# RAPID DETERMINATION OF TEMPERATURE-DEPENDENT PARAMETERS FOR THE CRYSTAL VISCOPLASTICITY MODEL

A Thesis
Presented to
The Academic Faculty

By

Daniel J. Smith

In Partial Fulfillment
Of the Requirements for the Degree
Master of Science in Mechanical Engineering

Georgia Institute of Technology

May 2011

# RAPID DETERMINATION OF TEMPERATURE-DEPENDENT PARAMETERS FOR THE CRYSTAL VISCOPLASTICITY MODEL

Approved by:

Dr. Richard W. Neu, Advisor
George W. Woodruff School of Mechanical Engineering
Georgia Institute of Technology

Dr. David L. McDowell
George W. Woodruff School of Mechanical Engineering
Georgia Institute of Technology

Dr. W. Steven Johnson
School of Materials Science and Engineering
Georgia Institute of Technology

Date Approved: March 30th 2011

# Acknowledgements

The author would like to express his gratitude to all those who have assisted in the completion of this work and to those who have made the work possible.

Firstly I would like to thank my advisor, Dr. Richard Neu. His guidance and insight were instrumental to the completion of this project. Without his kind assistance and gentle prodding I could not have succeeded. I would also like to thank Dr. David McDowell and Dr. W. Steve Johnson for serving as my committee members.

I would like to thank my fellow graduate students; Dr. Robert Amaro, Mike Kirka, Michael Hirsch, Patxi Fernandez-Zelaia, Dr. Bobby Watkins, and Matt Siopis. Their conversation relieved the stress of long days and their helpful insight, experience, and understanding was instrumental in the completion of this work. I would also like to thank Brad Fromm for his help in understanding and using ABAQUS and computational resources.

I would like to acknowledge the support of Siemens Energy and the personnel there including Saiganesh Iyer and Phillip Gravitt for supplying the raw material used in this work and for their feedback. I would also like to acknowledge the support of the NSF (I/UCRC) Center for Computational Materials Design, a joint venture with Penn State and Georgia Tech, and our mentors General Electric. I would like to thank some of the many personnel from General Electric, including Jim Laflen, John Pape, Adrian Loghin, and Liang Jiang for their feedback and insight. This work was also supported in part by the National Center for Supercomputing Applications.

I would like to extend a heartfelt thanks to wife, Nancy Smith-Berger, who showed me love and devotion throughout the project, but especially during its final stages. Without her support I could not have completed the work. I would also like to thank my parents, Dan and Kris Smith who have not only instilled in me the drive and desire to achieve a higher education, but who have supported me financially and emotionally throughout my education.

Last but not least I would like to thank my heavenly Father for His gracious blessings and wonderful love. Without Him I am nothing and can do nothing but "I can do all things through Christ who strengthens me" (Philippians 4:13).

# Table of Contents

# List of Tables

# List of Figures

# Summary

Thermomechanical fatigue life prediction is important in the design of Ni-base superalloy components in gas turbine engines and requires a stress-strain analysis for accurate results. Crystal viscoplasticity models are an ideal tool for this stress-strain analysis of Ni-base superalloys as they can capture not only the anomalous yielding behavior, but also the non-Schmid effect, the strain rate dependence, and the temperature dependence of typically large grained directionally-solidified and single crystal alloys. However, the model is difficult to calibrate even for isothermal conditions because of the interdependencies between parameters meant to capture different but similar phenomena at different length scales, many tied to a particular slip system. The need for the capacity to predict the material response over a large temperature range, which is critical for the simulation of hot section gas turbine components, causes the determination of parameters to be even more difficult since some parameters are highly temperature dependent. Rapid parameter determination techniques are therefore needed for temperature-dependent parameterizations so that the effort needed to calibrate the model is reduced to a reasonable level.

Specific parameter determination protocols are established for a crystal viscoplasticity model implemented in ABAQUS through a user material subroutine. Parameters are grouped to reduce interdependencies and a hierarchical path through the groups and the parameters within each group is established. This dual level hierarchy creates a logical path for parameter determination which further reduces the interdependencies between parameters, allowing for rapid parameter determination.

Next, experiments and protocols are established to rapidly provide data for calibration of the temperature-dependencies of the viscoplasticity. The amount of data needed to calibrate the crystal viscoplasticity model over a wide temperature range is excessively large due to the number of parameters that it contains which causes the amount of time spent in the experimentation phase of parameter determination to be excessively large. To avoid this lengthy experimentation phase each experiment is designed to contain as much relevant data as possible. This is accomplished through the inclusion of multiple strain rates in each experiment with strain ranges sufficiently large to clearly capture the inelastic response.

The experimental and parameter determination protocols were exercised by calibrating the model to the directionally-solidified Ni-bas superalloy DS-CM247LC. The resulting calibration describes the material's behavior in multiple loading orientations and over a wide temperature range of 20 °C to 1050 °C. Several parametric studies illustrate the utility of the calibrated model.

# Chapter 1. Introduction

Ni-base superalloys are used extensively in gas turbine engines. Their anomalous yielding behavior allows them to sustain higher loads at higher temperatures than most other metal alloys and their relatively high fracture toughness makes them more feasible than ceramics and refractory metals. However, the design of these alloys is far from trivial. Since they typically contain upwards of ten alloying elements (Reed, 2006), the number of possible combinations is quite large. The design of these alloys attempts to maximize fatigue life, fracture toughness, oxidation resistance, and creep resistance. To fully characterize a material for comparison of these properties requires a large amount of testing and an accurate knowledge of the stress-strain response of the material. The stress-strain response of a Ni-base superalloy is especially important in the prediction of fracture and fatigue life (Yue et al., 1997), since traditional methods of resolved shear stress, normal stress, and equivalent stress fail to accurately predict crack growth and fatigue lives. Predictive models could be used to estimate material performance, but the complex stress-strain behavior of Ni-base superalloys causes traditional models fail to accurately represent their behavior across a wide range of conditions such as strain rate, temperature, and material structure and orientation. Additional difficulty in modeling the behavior of these alloys is created from the wide temperature ranges which gas turbine components experience. Since the temperature difference between startup and shutdown can be in excess of 900 °C (Reed, 2006) any model used to predict material behavior must be calibrated over a wide temperature range for it to become viable for thermomechanical fatigue (TMF) predictions. The advanced crystal viscoplasticity (CVP) model in Shenoy et al. (2005) and

Shenoy (2006), which has an intricate flow rule and multiple parameter evolution equations, is able to capture the material's dependence on these factors, making it a desirable tool for use in life prediction and stress-strain modeling. In addition, since the components in these gas turbine engines are typically single crystal (SC) or directionally solidified (DS) where the grain size is fairly large, inelastic deformation is largely due to dislocation motion through a crystal lattice, upon which CVP models are based. This CVP model is therefore an ideal tool for the simulation of stresses and strains resulting from temperature-dependent loadings as it includes temperature-dependence, is strain rate sensitive, and captures the underlying cause of material deformation and can account for the anomalous yielding in these alloys.

This CVP model however is challenging to calibrate even to isothermal data and requires copious amounts of time to achieve acceptable TMF predictions. The number of parameters contained in the CVP model is one reason that its calibration is so difficult. Additionally since the model is primarily phenomenological there is no clear relationship between individual parameters and specific material behaviors. This causes interdependencies which have the affect of further increasing the difficulty of calibration. These factors limit the applicability of the model and cause it to be ill-fitted for use in industrial applications. Therefore techniques for rapidly determining the material parameters for a wide temperature range are needed so that the model becomes an economical as well as efficient tool for predicting material behavior.

In the following work a systematic approach to parameter determination is laid out. Chapter 2 reviews the literature and background information needed for the completion and understanding of this work. Chapter 3 details the CVP model and its attributes, showing the effect of each parameter and how the model captures specific behaviors. Chapter 4 shows the tools needed for rapid parameter determination, including the grouping, parameter determination path, and parameter sensitivity to data types. Also expressly shown in Chapter 4 is the method for rapid isothermal parameter determination as well as the method for converting isothermal parameter values into temperature dependent parameters. Chapter 5 contains the experimental data requirements and the design of experiments along with the list of experiments conducted in the completion of this work. Chapter 6 explains the experimental setup and shows the data acquired from the experiments. In Chapter 7 the results of the isothermal parameterizations and the predictions of TMF data are shown. Chapter 8 contains a parametric study of the calibrated CVP model where predictions of different loadings and loading types are compared. Finally Chapter 9 contains the conclusions of this work and recommendations for future research. The appendices are included for additional information on specific aspects of the CVP model which are not integral to its functioning and as a resource for additional parameter determination tools.

# Chapter 2. Literature Review

This chapter focuses on preparing the reader for the information contained in the following chapters. Since knowledge of crystal plasticity (CP) and crystal viscoplasticity (CVP) is key to understanding this work, this chapter focuses on these topics. First a brief history of CP and CVP models is given. Then the general formulation of CVP is discussed and examples of some types of models are shown and explained. Implementation of CVP models in finite element analyses is discussed next with the different benefits and costs of each one. Finally different approaches in the literature to parameter determination are examined.

## 2.1 Crystal Viscoplasticity Model Development

Crystal plasticity and viscoplasticity are rooted in the 1938 paper by Taylor in which he proposed that plastic deformation occurs by dislocation motion through the crystal lattice (Taylor, 1938). The theory was not implementable at the time since the computational power did not exist to apply the theory (Asaro, 1983): it was not until 1943 that the first finite element (FE) simulations were performed (Courant, 1943). Even so the first crystal plasticity simulations were performed in 1982 by Pierce et al. (1982) who greatly simplified his model by only using two symmetric slip systems. In fact it was not until Becker (1991) that simulations based upon the 12 octahedral slip systems of a face centered cubic (FCC) crystal were performed. Since then the form of CVP models has increasingly become more complex with increased computing power available for implementation. The following is a brief review of the major changes in CVP models, with a focus on the developments related to the model of Shenoy et al. (2005), which is used in this work.

The early formulations of CP and CVP models relied on the $J_2$ stress invariant as the primary cause of plastic deformation, which corresponds to a Von Mises criterion. While this works well for static analyses of polycrystalline metals, it is inconsistent with the formulation of CVP since dislocation motion has been shown to be caused by the resolved shear stress (Frost and Ashby, 1982). Therefore the resolved shear stress on a slip system the $J_2$ stress invariant as the overstress, which is the stress that exceeds any yield stress or back stress.

Another change in CVP models was brought about by the understanding that creep and plasticity were both caused by the same phenomena. Early models treated the plastic and creep strains separately, however, with the understanding that the same stress causes these different effects, these strains were combined in the 1970s to form what is termed “unified” viscoplastic formulations (Chaboche and Rousselier, 1983; Chan et al., 1985; Walker and Jordan, 1985). The formulation of both creep and plasticity in a single term causes the treatment of these strains to be more consistent with the deformation of metals.

Early CVP models focused on power law equations for implementing the plastic strains. These equations are well suited for capturing the creep behavior of metals since this behavior follows a linear trend when plotted with log-log axes. However Ni-base superalloys exhibit strain rate insensitivity at higher strain rates and lower temperatures, so these power law formulations fail to accurately describe the behavior of this class of materials under these conditions. The pairing of an exponential with a power law, as in the Shenoy et al. (2005) model which is able to capture both the rate-sensitive and rate-insensitive behaviors, was first published by Nouailhas (1989) who used it as a unified $J_2$ plasticity model. The model was calibrated to an austenitic stainless steel with good results in both cyclic hysteresis and creep, even though the hardening rules were simple compared to current formulations.

The ability to recreate temperature-dependent loadings with CVP models is important for fatigue life prediction of Ni-base superalloys. However the early evolution equations for hardening and state variables were not formulated consistently for the prediction of temperature-dependent loadings since the equations of most CVP models are based in thermodynamics and the arbitrary addition of temperature as a variable was inconsistent with the formulation of the equations. Therefore a major milestone was reached when McDowell (1992) extended the model of Moosbrugger and McDowell (1990), which also has a paired power law and exponential, to allow for temperature-dependent loadings by the addition of temperature rate terms in the evolution equations.

## 2.2 Formulation of Crystal Viscoplasticity Models

In general most crystal plasticity and viscoplasticity models follow the same initial formulation: they are based on dislocation motion through a crystal structure (Asaro, 1983) and they are fundamentally dependent on continuum mechanics. The essence of this formulation is to assume that deformation is achieved through stretching and rotation of the crystal lattice. An isothermal deformation is therefore separable into two distinct deformation gradients, $\mathbf{F}^{p}$ and $\mathbf{F}^{*}$, as shown in Figure 2.1 where $\mathbf{F}^{*}$ stretches the lattice and $\mathbf{F}^{\theta}$ performs lattice rotation. However for temperature-dependent simulations $\mathbf{F}^{*}$ is separable into elastic and thermal deformations, $\mathbf{F}^{e}$ and $\mathbf{F}^{\theta}$ respectively (Srikanth and Zabaras, 1999) as is shown in Figure 2.2. The total deformation gradient of the lattice, $\mathbf{F}$, is obtained through multiplication of the separate deformation gradients,

$$\mathbf{F} = \mathbf{F}^{e} \cdot \mathbf{F}^{p} \cdot \mathbf{F}^{\theta} \tag{2.1}$$

where the order of deformation is right to left.

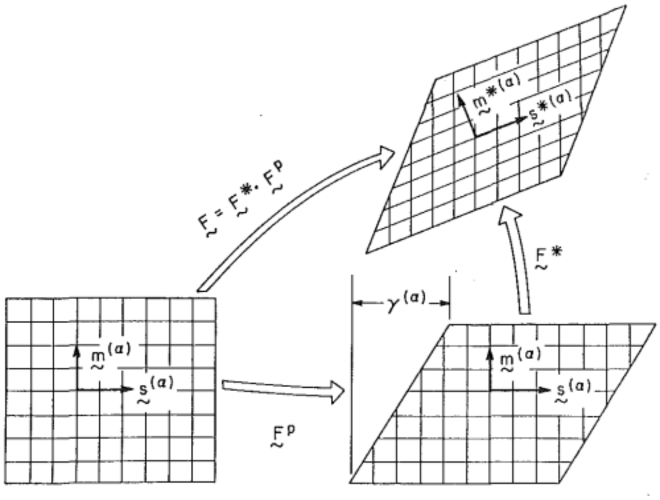

Figure 2.1: Kinematics of crystal deformation through dislocation slip (Asaro, 1983)

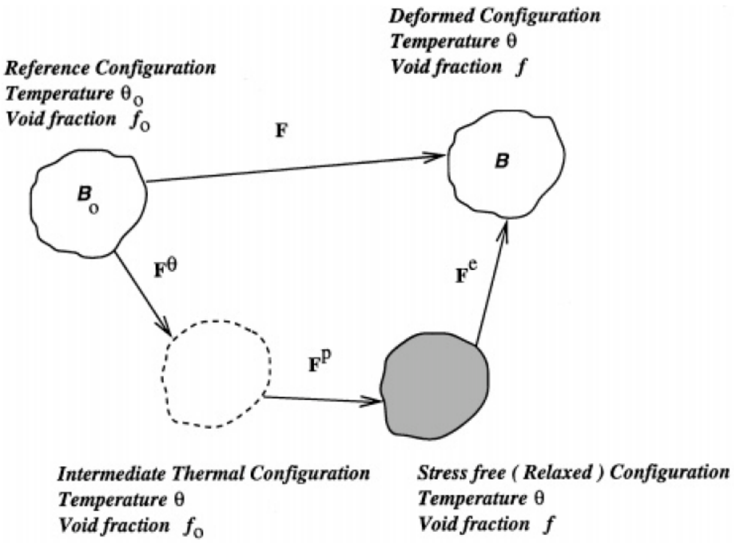

Figure 2.2: Addition of thermal deformation to the constitutive relations (Srikanth and Zabaras, 1999)

In the normal formulation of model updates the total strain is specified. The thermal strain is then calculated and subtracted from the total strain to get the mechanical strain. The plastic strain is then determined based upon the state of stress in the material and the elastic strain is finally determined by subtracting the plastic strain from the mechanical strain.

$$\boldsymbol{\varepsilon}^{e} = \boldsymbol{\varepsilon}^{\mathrm{Tot}} - \boldsymbol{\varepsilon}^{\theta} - \boldsymbol{\varepsilon}^{\mathrm{p}} \tag{2.2}$$

$\boldsymbol{\varepsilon}^{\mathrm{e}}$ is the elastic strain, $\boldsymbol{\varepsilon}^{\mathrm{Tot}}$ is the total strain, $\boldsymbol{\varepsilon}^{\theta}$ is the thermal strain, and $\boldsymbol{\varepsilon}^{\mathrm{p}}$ is the plastic strain.

The deformation gradients are determined in the same order as the strains. The total deformation gradient, $\mathbf{F}^{\mathrm{Tot}}$, is found by,

$$\boldsymbol{\varepsilon}^{\mathrm{Tot}} = \mathbf{N} \cdot \boldsymbol{\epsilon} \cdot \mathbf{N} = \frac{1}{2}\mathbf{N} \cdot \left(\mathbf{F}^{\mathrm{Tot}^{\mathrm{T}}} \cdot \mathbf{F}^{\mathrm{Tot}} - \mathbf{I}\right) \cdot \mathbf{N} \tag{2.3}$$

$$\mathbf{F}^{\mathrm{Tot}^{\mathrm{T}}} \cdot \mathbf{F}^{\mathrm{Tot}} = 2(\mathbf{N} \cdot \boldsymbol{\varepsilon}^{\mathrm{Tot}} \cdot \mathbf{N}) + \mathbf{I} \tag{2.4}$$

where $\boldsymbol{\epsilon}$ is the Green's strain and $\mathbf{F}^{\mathrm{Tot}^{\mathrm{T}}}$ is the transpose of $\mathbf{F}^{\mathrm{Tot}}$. $\mathbf{N}$ is a direction vector. The thermal deformation gradient is determined through the coefficient of thermal expansion (CTE), $\beta$, where a finite step between temperatures is used (Srikanth and Zabaras, 1999).

$$\mathbf{F}_{\mathrm{i+1}}^{\theta} = \mathrm{e}^{\beta\Delta\mathrm{T}}\mathbf{F}_{\mathrm{i}}^{\theta} \tag{2.5}$$

Here the subscripts "i" and "i+1" represent the old and new $\mathbf{F}^{\theta}$ respectively. This update procedure is necessary for the implementation of the thermal strains since the coefficient is itself a function of temperature. The plastic deformation gradient is calculated by summing the inelastic strains from each slip system.

$$\dot{\mathbf{F}}^{\mathrm{p}} \cdot \mathbf{F}^{\mathrm{p}^{-1}} = \mathbf{L}^{\mathrm{p}} = \mathbf{D}^{\mathrm{p}} + \mathbf{W}^{\mathrm{p}} = \sum_{\alpha=1}^{\mathrm{N}} \dot{\gamma}^{\alpha}(\mathbf{s}_{0}^{\alpha} \otimes \mathbf{m}_{0}^{\alpha}) \tag{2.6}$$

Here $\mathbf{L}^{\mathrm{p}}$ is the velocity gradient which can be decomposed into the rate of plastic stretch, $\mathbf{D}^{\mathrm{p}}$, and the rate plastic of spin, $\mathbf{W}^{\mathrm{p}}$. The vectors $\mathbf{s}_{0}^{\alpha}$ and $\mathbf{m}_{0}^{\alpha}$ are unit vectors in the slip direction and slip plane normal direction, respectively, and N is the total number of slip systems with α being a slip system.

As mentioned previously one of the major characteristics of CVP models is the use of the Schmid stress (Schmid and Boas, 1950), or critical resolved shear stress (CRSS) as the activation parameter for slip systems. Schmid's law states that a slip system is potentially active when the resolved shear stress on the slip plane in the slip direction (the Schmid stress) reaches a critical value, the CRSS. The shear stress on a slip system in the slip direction, $\boldsymbol{\tau}^{\alpha}$, is related to the remote stress, $\boldsymbol{\sigma}$, by,

$$\boldsymbol{\tau}^{\boldsymbol{\alpha}} = \mathrm{m}_{\nu}^{\alpha} \cdot \boldsymbol{\sigma} \tag{2.7}$$

where $\alpha$ the slip system, $\nu$ is the slip direction, and $\mathrm{m}_{\nu}^{\alpha}$ is the Schmid factor, using the convention of Kocks (1970). However, when loaded uniaxially in a particular direction the Schmid stress on a particular slip system is not trivial to define. The Schmid factors for the twelve primary octahedral and six cubic slip systems considered in the Shenoy et al. (2005) CVP model are therefore shown in 2.1 for uniaxial loadings in the [1 0 0], [0 1 1], and [1 1 1] directions. The Schmid factors for the cubic slip systems can be seen to be zero for uniaxial loading in one of the principal crystal directions.

$$\begin{array}{cccl}
[1\;0\;0] & [0\;1\;1] & [1\;1\;1] & \text{Loading Direction} \\
\begin{pmatrix}0\\0.408248\\-0.408248\\0\\-0.408248\\-0.408248\\-0.408248\\0\\0.408248\\0\\0.408248\\0.408248\end{pmatrix} &
\begin{pmatrix}0\\0.408248\\-0.408248\\0\\-0.408248\\-0.408248\\-0.408248\\0\\0.408248\\0\\0.408248\\0.408248\end{pmatrix} &
\begin{pmatrix}0\\0\\0\\0\\0.272166\\0.272166\\0\\0.272166\\0.272166\\0.272166\\0.272166\\0\end{pmatrix} & \text{Primary octahedral slip system Schmid factors} \\
\begin{pmatrix}0\\0\\0\\0\\0\\0\end{pmatrix} &
\begin{pmatrix}0\\0\\0.353553\\-0.353553\\0.353553\\0.353553\end{pmatrix} &
\begin{pmatrix}0.471405\\0\\0.471405\\0\\0.471405\\0\end{pmatrix} & \text{Cube slip system Schmid factors}
\end{array}$$

Figure 2.3: Schmid factors for [1 0 0], [0 1 1], and [1 1 1] loading directions on primary octahedral and cubic slip planes

Using these Schmid factors to calculate the shear stress on a slip system the rate of inelastic shear strain can then be determined. There are a myriad of formulations for the calculation of $\dot{\gamma}$. These equations are termed “flow rules” since the plastic flow is determined through them. The most commonly used type of flow rule is the power law equation, an example of which is (Asaro, 1983),

$$\dot{\gamma}^{(\alpha)} = \dot{a}^{(\alpha)} \left(\frac{\tau^{(\alpha)}}{g^{(\alpha)}}\right) \left|\frac{\tau^{(\alpha)}}{g^{(\alpha)}}\right|^{(1/m)-1} \tag{2.8}$$

where $\alpha$ is a slip system, $\tau^{(\alpha)}$ is the overstress on the slip system, $g^{(\alpha)}$ is the drag stress which describes isotropic strain hardening and is allowed to evolve with $\dot{\gamma}^{(\alpha)}$, $\dot{a}^{(\alpha)}$ is the reference strain rate, and *m* is the flow exponent. Some other examples of power law flow rules can be found in the literature (McGinty and McDowell, 1999; Almroth et al., 2002; Almroth et al., 2004). Dual power law functions (Shenoy et al., 2008),

$$\dot{\gamma}^{\alpha} = \left[ \dot{\gamma}_0 \left\langle \frac{\left|\tau^{\alpha} - \chi^{\alpha}\right| - \kappa^{\alpha}_{\lambda}}{D^{\alpha}} \right\rangle^{n_1} + \dot{\gamma}_1 \left\langle \frac{\left|\tau^{\alpha} - \chi^{\alpha}\right|}{D^{\alpha}} \right\rangle^{n_2} \right] \mathrm{sgn}\left(\tau^{\alpha} - \chi^{\alpha}\right) \tag{2.9}$$

are used to capture both the rate dependent and rate insensitive regions of material deformation. There are two flow exponents, $n_1$ and $n_2$ which control the rate insensitive and rate dependent regions respectively. There are also two reference inelastic shear strain rates, $\dot{\gamma}_0$ and $\dot{\gamma}_1$ to control the activation of the separate regions. The rate insensitive term has a threshold stress, $\kappa^{\alpha}$, while the rate dependent term does not so that the stress may be recovered until the back stress, $\chi^{\alpha}$, is reached. The drag stress, $D^{\alpha}$, captures the flow resistance in the material that can be overcome by energy fluctuations. Another example of an additive power law flow rule can be found in Chaboche (1989). Power laws combined with an exponential are used (Shenoy et al., 2005),

$$\dot{\gamma}^{\alpha} = \dot{\gamma}_0 \Theta(\mathrm{T}) \left\langle \frac{\tau^{\alpha}_{v}}{D^{\alpha}} \right\rangle^{n} \exp\left( B_0 \left\langle \frac{\tau^{\alpha}_{v}}{D^{\alpha}} \right\rangle^{n} \right) \mathrm{sgn}\left(\tau^{\alpha} - \chi^{\alpha}\right) \tag{2.10}$$

These also are able to capture the rate sensitive and insensitive regions. However, a main difference is that the rate insensitivity can be much higher than the dual power law equations. Also this equation tend to be stiffer, e.g. more difficult to solve when implemented. Additional examples of flow rules with exponentials can be found in the literature (Nouailhas, 1989; Ramaswamy et al., 1990; Sheh and Stouffer, 1990; Stouffer et al., 1990; McDowell, 1992; Bhattachar and Stouffer, 1993; Rowley and Thornton, 1996). Hyperbolic sine functions are also used (Miller, 1976),

$$\dot{\gamma} = B\left[\sinh\left(\frac{\sigma_{\mathrm{v}}}{K}\right)^{1.5}\right]^{n} \tag{2.11}$$

where $B$ is the reference inelastic shearing rate, $K$ is the drag stress, and $\sigma_{\mathrm{v}}$ is the viscous overstress. These contain both the rate sensitive and rate insensitive regions in the single term which simplifies the form of the flow rule, but they do not give the versatility of either the dual power law or the power law with the exponential.

The power law relationship is commonly used in the flow rule of CP and CVP models since it accurately captures the creep behavior of metals, although at higher strain rates the inelastic shear strain rate no longer follows the power law relationship. This can be neglected, however if the strain rates are assumed to be low enough to lie in the power law region of the material. An example of a more complicated power law flow rule can be found in Walker and Jordan (1985),

$$\begin{aligned}\dot{\gamma} = K_{\mathrm{r}}^{-p}\Bigg\{&(\pi^{\mathrm{r}}_{\mathrm{mn}} - \omega^{\mathrm{r}}_{\mathrm{mn}})|\pi^{\mathrm{r}}_{\mathrm{mn}} - \omega^{\mathrm{r}}_{\mathrm{mn}}|^{p-1} \\ &+ \sum_{\mathrm{i}=m}^{z} \alpha_{ii}(\pi^{\mathrm{r}}_{\mathrm{ii}} - \omega^{\mathrm{r}}_{\mathrm{ii}})|\pi^{\mathrm{r}}_{\mathrm{ii}} - \omega^{\mathrm{r}}_{\mathrm{ii}}|^{p-1} \\ &+ 2\alpha_{\mathrm{mz}}(\pi^{\mathrm{r}}_{\mathrm{mz}} - \omega^{\mathrm{r}}_{mz})|\pi^{r}_{\mathrm{mz}} - \omega^{r}_{\mathrm{mz}}|^{p-1} \\ &+ 2\alpha_{\mathrm{nz}}(\pi^{\mathrm{r}}_{\mathrm{nz}} - \omega^{\mathrm{r}}_{\mathrm{nz}})|\pi^{\mathrm{r}}_{\mathrm{nz}} - \omega^{\mathrm{r}}_{\mathrm{nz}}|^{p-1}\Bigg\}\end{aligned} \tag{2.12}$$

where non-Schmid factors are additionally accounted for through $\alpha_{\mathrm{ii}}$, $\alpha_{\mathrm{mz}}$, and $\alpha_{\mathrm{nz}}$,. The $K_{\mathrm{r}}$ is the drag stress, $\omega$ is the back stress, $p$ is the flow exponent, r is the slip direction of the resolved shear stress, $\pi^{\mathrm{r}}_{\mathrm{mn}}$, and the subscripts $m$, $n$, and $z$ are the locations in the stress tensor. In their formulation, as with others (Asaro, 1983; Walker and Jordan, 1985; McGinty and McDowell, 1999) the drag stress and back stress are allowed to evolve with inelastic deformation.

Most of the above equations are phenomenological in nature. However, there is another method of formulating CVP models; basing the state variables on microstructural phenomena such as dislocation density, dislocation initiation and cancellation, and grain boundary considerations (Arsenlis and Parks, 1999; Arsenlis and Parks, 2002; Balasubramanian and Anand, 2002; Evers et al., 2002; Arsenlis et al., 2004; Evers et al., 2004; Ma et al., 2006b; Ma et al., 2006a; Shenoy et al., 2008). Phenomenological models are more widely used. These seek to recreate certain aspects of material behavior by considering the kinetics and kinematics of deformation, implicitly accounting for microstructure attributes. When applying phenomenological models to some areas, such as small scale deformations or interface mechanisms, the constitutive equations are often insufficient (Roters et al., 2010). The physically based constitutive equations which explicitly consider microstructure phenomena tend to be more complex and thus more difficult to implement, but as mentioned above are able to transcend some of the problems associated with phenomenological models.

## 2.3 Implementation of Crystal Viscoplasticity Models

With their complex flow rules and even more convoluted evolution equations the implementation of a CVP model is no trivial matter. Yet this is crucial to the efficient operation of the model. There are three distinct methods for solving the constitutive equations; explicit, semi-implicit, and implicit. Within each of these methods there are multiple starting points for solving an increment in time and strain.

In explicit algorithms the stress required to reach a particular strain is calculated and the inelastic deformation resulting from this stress is found. This solution is then assumed to be accurate and the analysis progresses to the next time step. Explicit is the easiest to formulate since it does not require checking a solution, but rather, as stated above, assumes that the solution found on the first iteration is accurate. Small time steps are used to ensure that the solution of the iteration is not far from the true solution. This method is able to evaluate a time step very quickly since it does not require iteration, but it requires very small time steps and does not ensure an accurate solution.

Implicit is more difficult to implement than explicit, although it results in the most accurate solution. The implicit method uses a predictor-corrector scheme where a prediction of the stress required to obtain a particular strain is generated. The method then solves for the inelastic deformation using this prediction. The inelastic deformation is then used to correct the stress and a new stress prediction is created with which the inelastic deformation is again calculated. This is repeated until the difference between the calculated stress and predicted stress is within a level of tolerance. This method is more robust than the explicit method since it, in theory, can take very large steps in time and strain and still converge to an accurate solution. Its accuracy comes at a price, however since it is more difficult to implement and takes longer to implement a single time increment. Comparing explicit and implicit methods by the time needed for similar accuracies, the implicit method will usually perform better.

Semi-implicit is halfway between explicit and implicit where an initial guess is made, but only one iteration is used to attempt convergence. As with the explicit method this does not ensure an accurate solution. It does, however give a better result than the explicit method without sacrificing as much of the speed that makes it attractive as implicit algorithm does. Difficulty arises however in determining the best way to update the initial guess since the method only gives one opportunity for improvement.

There are in general five different starting points for the implicit method, which uses a predictor-corrector scheme. These are represented in Figure 2.4 which also shows the order of updating the prediction. The symbol **S** in this case represents the second Piola-Kirchoff stress which can be converted to a shear stress on a slip system and used to calculate the inelastic deformation. The Piola-Kirchoff stress can be found from the Cauchy stress, **σ**, by,

$$\mathbf{S}=\mathrm{J}\cdot\mathbf{F}^{-1}\cdot\boldsymbol{\sigma}\cdot\mathbf{F}^{-\mathrm{T}} \tag{2.13}$$

where J is the Jacobian, $\mathbf{F}^{-1}$ is the inverse of **F**, and $\mathbf{F}^{-\mathrm{T}}$ is the transpose of $\mathbf{F}^{-1}$. The most common starting points are $\mathbf{F}_\mathrm{e}$, $\mathbf{F}_\mathrm{p}$, **S**, or $\dot{\gamma}$, and should result in identical solutions. However in choosing a starting point one must consider that the Jacobian matrix will need to be inverted when using the Newton-Raphson method, and that the equations may be more or less difficult to evaluate. The size of the Jacobian is equal to the number of independent variables of the item used as the prediction. Thus for **S** there are six due to symmetry, for $\mathbf{F}_\mathrm{p}$ there are eight since the volume is conserved, for $\mathbf{F}_\mathrm{e}$ there are nine, and for $\dot{\gamma}$ there are twelve or more for FCC crystalline metals, depending on the number of slip systems. However using $\dot{\gamma}$ produces much better stability since there are small variations in stress associated with variations in $\dot{\gamma}$ as it gets larger. The inverse is true for the other three, which results in less stability.

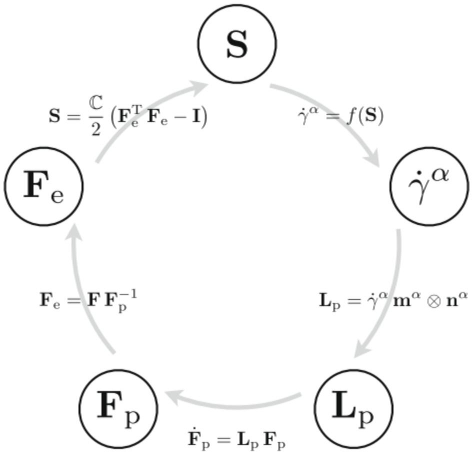

Figure 2.4: Order of updates in implementation of CVP models (Roters et al., 2010)

## 2.4 Parameter Determination

Determining material parameters for the various CVP models is not a trivial task. Added to this is the lack of information on how each model functions or what each parameter's role is. Even though each model is calibrated to represent experimental data, the authors rarely give more than a brief explanation of the calibration procedures (Nouailhas, 1989; Sheh and Stouffer, 1990; McDowell, 1992; Huber and Tsakmakis, 2001; Almroth et al., 2002; Yaguchi et al., 2002a; Yaguchi et al., 2002b; Mucke and Bernhardi, 2003; Almroth et al., 2004; Tong, 2004; Shenoy et al., 2006; Shenoy, 2006; Wang et al., 2006; Christ and Bauer, 2011). This section presents a limited review of the methods that have been published, such as neural networks, genetic algorithms, and optimization schemes.

Sheh and Stouffer (1990) determined the material parameters for a CVP model with an exponential flow rule,

$$\dot{\gamma}_{\mathrm{OCT}}^{\alpha\beta} = D_1 \exp\left[-A_1\left(\frac{\mathrm{Z}_1^{\alpha\beta}}{\left|\tau^{\alpha\beta}-\Omega_1^{\alpha\beta}\right|}\right)^{n_{11}}\right]\frac{\tau^{\alpha\beta}-\Omega_1^{\alpha\beta}}{\left|\tau^{\alpha\beta}-\Omega_1^{\alpha\beta}\right|} \tag{2.14}$$

where $\mathrm{Z}_1^{\alpha\beta}$ is the drag stress, $\Omega_1^{\alpha\beta}$ is the back stress, $\tau^{\alpha\beta}$ is the resolved shear stress, $\dot{\gamma}_{\mathrm{OCT}}^{\alpha\beta}$ is the local slip rate, $n_{11}$ is the strain-rate sensitive exponent, and $D_1$ and $A_1$ are scale factors. The back stress evolution,

$$\dot{\Omega}_1^{\alpha\beta} = F_1\left|\dot{\gamma}_{\mathrm{OCT}}^{\alpha\beta}\right|^{n_{12}}\left[\mathrm{sign}\left(\dot{\gamma}_{\mathrm{OCT}}^{\alpha\beta}\right)-\frac{\Omega_1^{\alpha\beta}}{\Omega_{\mathrm{SAT}}{}^{1}}\right]+G_1\dot{\tau}^{\alpha\beta} \tag{2.15}$$

has both elastic and inelastic portions. $n_{12}$, $F_1$, $G_1$, and $\Omega_{\mathrm{SAT1}}$ are fitting parameters. The drag stress evolution equation,

$$\mathrm{Z}_1^{\alpha\beta} = H_1^{\alpha\beta} + V_1\tau_1^{\alpha\beta} + V_2\left|\tau_2^{\alpha\beta}\right| + V_3\tau_3^{\alpha\beta} \tag{2.16}$$

contains has mostly non-evolving terms, except for $H_1^{\alpha\beta}$ which is the measure of work hardening. $V_1$, $V_2$, and $V_3$ are fitting parameters which modify the shear stresses $\tau_1^{\alpha\beta}$, $\tau_2^{\alpha\beta}$ , and $\tau_3^{\alpha\beta}$. The approach to determining the parameters was to run simulations and compare the results. Parameters were determined using different sets of data in the process shown in Figure 2.5. Specifically the strain-rate sensitivity exponent, $n_{11}$, orientation dependence factors, $V_1$, $V_2$, and $V_3$, saturated state variable values, $Q_{SAT}^1$ and $H_{11}$, were determined using saturated data. Strain hardening and inelastic recovery data were then used to evaluate the back stress constants $G_1$, $n_{12}$, and $F_1$. Finally since the material stabilized quickly the hardening equation was not utilized.

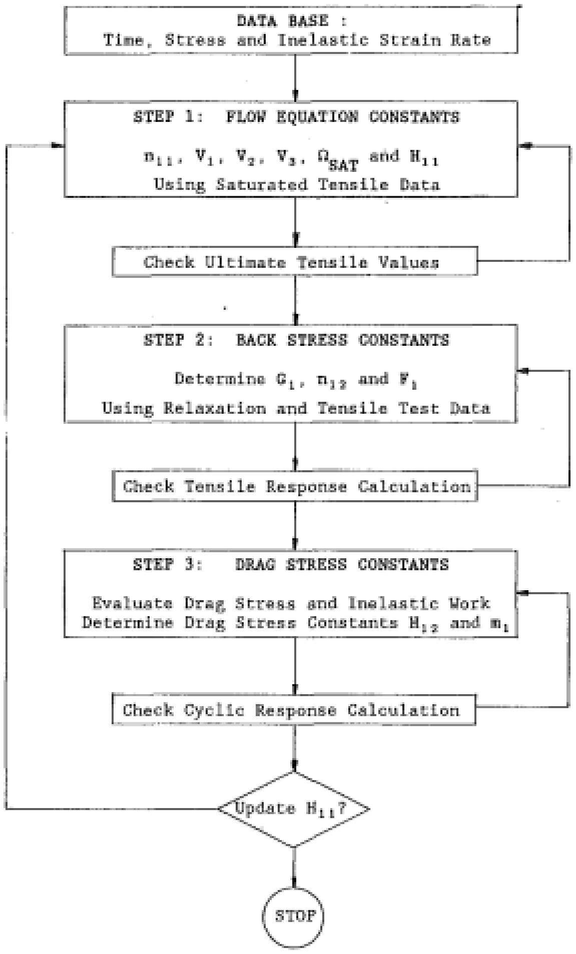

Figure 2.5: Parameter determination loops for an exponential flow rule (Sheh and Stouffer, 1990)

Huber and Tsakmakis (2001) use a neural network to identify parameters for a viscoplasticity model. To capture the material behavior of a ferritic steel a series of twenty experiments of three types, tension, cyclic, and creep, were performed. A neural network was then trained to determine the model parameters from simulations by adjusting the neural network until the outputs matched the simulations sufficiently well. The network was then used to determine model parameters from simple experimental histories. The calibrated model was able to model the experimental behavior with a high degree of accuracy.

Others too have used neural networks to determine model parameters for a range of materials (Sumpter and Noid, 1996; Yagawa and Okuda, 1996). Some of the benefits of neural networks include (Yagawa and Okuda, 1996):

- A nonlinear mapping of input data to output data in the network can be constructed through a learning process of some sample input versus output relations.
- The trained network can predict the output data satisfactorily even for unlearned input data, provided the training data is sufficiently extensive.
- The trained network produces parameters quickly while requiring minimal computing power.

However, the effort required to tune them is extensive and will need to be shortened before neural networks become an effective parameter determination tool.

One of the methods used to determine model parameters for simple CP models has been genetic algorithms (GAs) (Goldberg, 1989; Carroll, 1996), although no references were found which applied directly to NI-base superalloys (Xie et al., 2004; Venkataramani et al., 2006). GAs operate by evaluating possible parameter combinations based on their fitness, which is an error evaluated between the result of the parameter set and experimental data. First a random set of parameter combinations are selected. The best combinations are then selected for use in the next round and new possibilities are created by (1) reproduction, (2) crossover, and (3) mutation. This process continues until the best combination is better than the acceptable level. Because of the many different combinations considered throughout the course of the algorithm it is an effective method for determining parameters for simple models. However, because the method requires many parameter-based predictions it is ill-fitted for use with CVP models since they in general are not fast in generating the predictions, and in general contain more parameters than CP models which increases the number of combinations needed for convergence. This leads to long convergence times on CVP models for this method while the result can be more quickly achieved through other methods.

Tong (2004) calibrates a Chaboche type model (Chaboche and Rousselier, 1983) to cyclic and creep data for a NI-base superalloy. To determine the parameters he first generates an estimate, and then uses an iterative optimization scheme to find a final parameter set. This is illustrated in Figure 2.6. The main problem with this method is that the number of iterations required to reach a final parameter set, and thus the time required to complete the algorithm, is highly dependent on the accuracy of the initial parameters. Therefore an accurate method of creating the initial parameter set is still required. Tong does not fully define such a method, but does state that parameters are separated and initialized based upon data that they are most sensitive to.

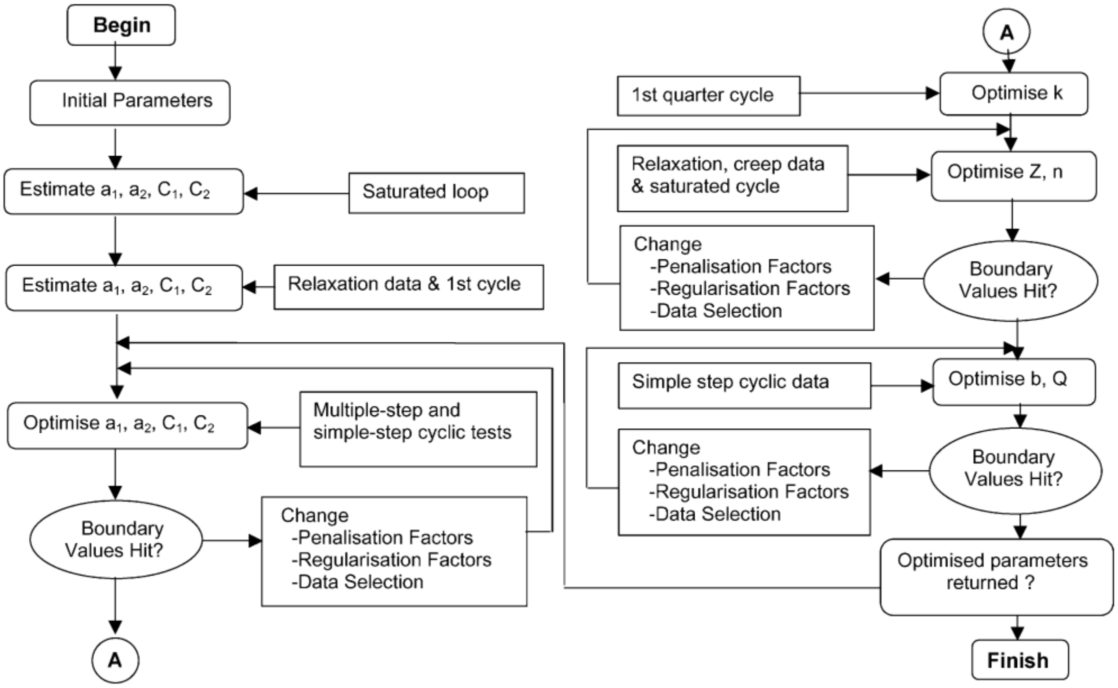

Figure 2.6: Parameter determination algorithm from Tong (2004)

Song (2010) uses an iterative approach combined with a parameter clustering to optimize the parameters for a macroscale viscoplastic model similar to the one used in this work. Figure 2.7 shows the process flow diagram that was used. The first part of his algorithm is a parameter clustering which can be seen in the figure as the parameter sets. These allow him to separate parameters into groups which are related to specific behaviors. By selecting individual clusters for optimization each cluster can be fitted to match experimental data. In addition to his clustering of parameters Song splits his optimizations into three distinct levels: 1) part of an experiment such as a creep hold where a specific parameter is determined, 2) a single experiment where multiple parameters are simultaneously considered, and 3) multiple experiments where all clusters are established. Note that level three can include multiple temperatures and strain rates.

However a limited temperature range was used and the method loops back on itself to the extent that the number of times a parameter is modified is excessive.

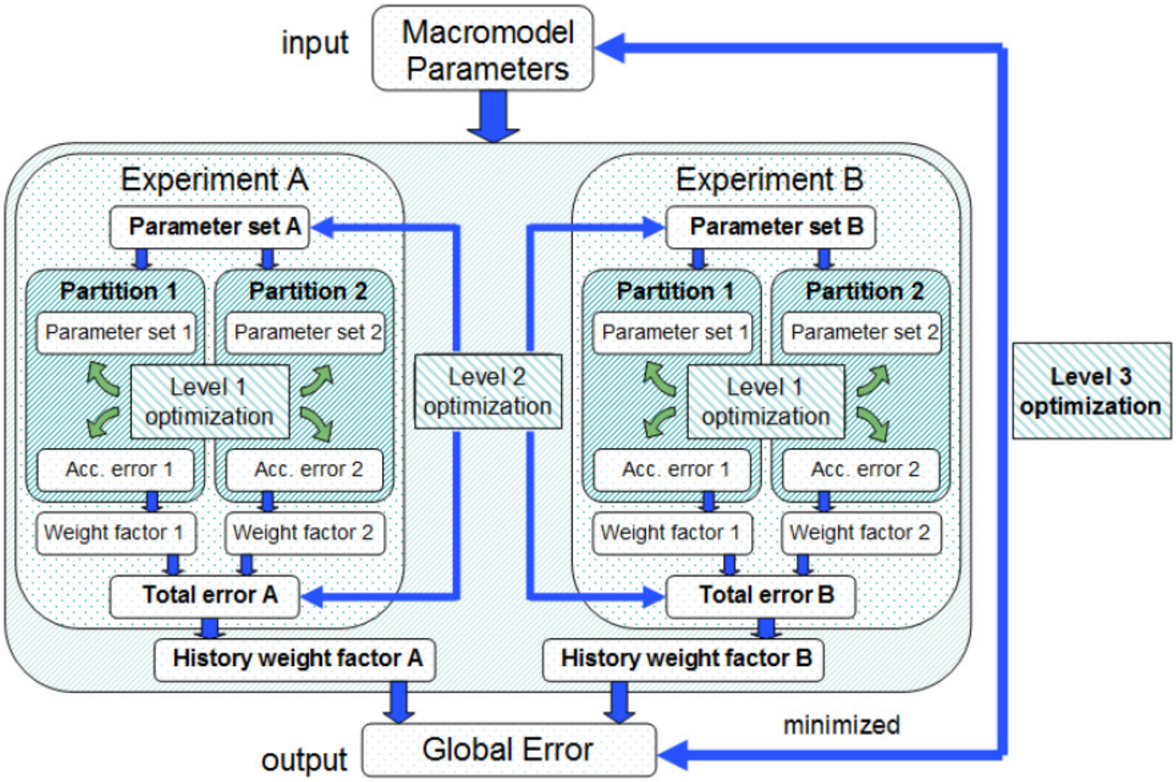

Figure 2.7: Hierarchical optimization scheme from Song (2010)

# Chapter 3. Crystal Viscoplasticity Model Description and Implementation

The crystal viscoplasticity model used in this research was developed by Shenoy (Shenoy et al., 2005; Shenoy, 2006). The following is a more in-depth explanation of the flow rule and evolution equations, along with examples of the functionality of each portion of the model. Also included in this chapter is a description of the implementation of the CVP model in ABAQUS and a list of parameters needed for running simulations.

## 3.1 Crystal Viscoplasticity Model Description

In the development of the model it was calibrated to GTD-111 (Shenoy et al., 2005; Shenoy, 2006), a directionally solidified Ni-bas superalloy. The flow rule,

$$\dot{\gamma}^{\alpha} = \dot{\gamma}_0 \Theta(\mathrm{T}) \left\langle \frac{\tau_{\mathrm{v}}^{\alpha}}{\mathrm{D}^{\alpha}} \right\rangle^{n} \exp\left\{ B_0 \left\langle \frac{\tau_{\mathrm{v}}^{\alpha}}{\mathrm{D}^{\alpha}} \right\rangle^{n+1} \right\} \mathrm{sgn}\left(\tau^{\alpha} - \chi^{\alpha}\right) \tag{3.1}$$

is a power law multiplied by an exponential. As discussed in the previous chapter the power law term captures the creep regime while the exponential captures the rate insensitive regime. The flow rule is plotted in Figure 3.1 using arbitrary parameter values. The Macaulay brackets, $\langle x \rangle$, act to keep the flow rule turned off when the $\tau_{\mathrm{v}}$ is negative. The drag stress, $\mathrm{D}^{\alpha}$, is a measure of the flow potential of the material as it effectively accounts for the component of flow resistance than can be overcome by thermal fluctuation (Shenoy, 2006). $\dot{\gamma}_0$ is the reference inelastic shear strain rate and $\tau_{\mathrm{v}}^{\alpha}$. The rate insensitive region is set by $B_0$ and "$n$+1" collectively. However, since the flow exponent, $n$, also governs the power law creep region, $B_0$ effectively is the only parameter free to control this region. The temperature dependent diffusivity function, Θ(T), is controlled by a single parameter; the dislocation activation energy, $Q_0$. This function controls the difference between the inelastic shear strain rates for identical $\tau_v$ values at different temperatures, which can be easily seen in the difference between the flow rule lines in Figure 3.1.

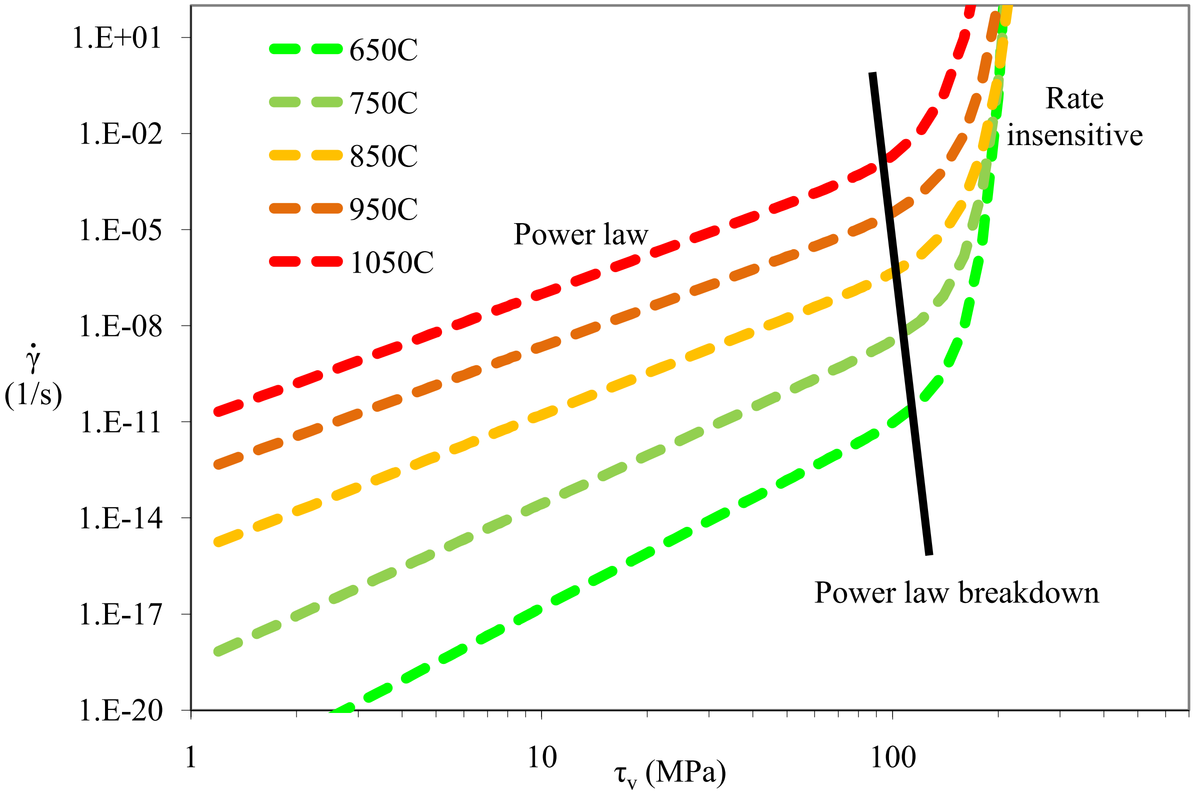

Figure 3.1: Flow rule for arbitrary parameter values

The drag stress, $D^\alpha$, does not evolve, but rather scales,

$$D^\alpha = D_0 \frac{\mu}{\mu_0} \tag{3.2}$$

by the shear modulus, $\mu$, where $\mu_0$ is the shear modulus at 0K. The viscous overstress, $\tau_v$, in Eq. (3.1) is found by,

$$\tau_v^\alpha = |\tau^\alpha - \chi^\alpha| - \kappa^\alpha \frac{\mu}{\mu_0} \tag{3.3}$$

where $\chi^\alpha$ is the back stress and $\kappa^\alpha$ is the threshold stress. The back stress evolution equation,

$$\dot{\chi}^\alpha = h_\chi|\dot{\gamma}^\alpha| - h_{\chi d}|\dot{\gamma}^\alpha|\chi^\alpha + \left(\frac{1}{R_\chi}\frac{\partial R_\chi}{\partial \mathrm{T}} + \frac{1}{h_\chi}\frac{\partial h_{\chi d}}{\partial \mathrm{T}}\right)\chi^\alpha \dot{\mathrm{T}} - h_{\chi s}\Theta_{\chi s}(\mathrm{T})|\chi^\alpha|^{r_{\chi s}}\chi^\alpha \tag{3.4}$$

where,

$$R_\chi = \frac{h_\chi}{h_{\chi d}} \tag{3.5}$$

models the evolution of the dislocation structure within the material and has a temperature rate term to allow for consistency in temperature-dependent loadings. The first term, with the rate of evolution parameter, $h_\chi$, represents hardening due to dislocations piling up on obstacles while the second captures the dynamic recovery which is the reduction in dislocation density due to annihilation of dislocations of opposite sign. The third term, with the temperature rate, accounts for the evolution of back stress due to temperature changes and is required if the model is to be temperature dependent (McDowell, 1992). The final term models the dynamic thermal recovery of the back stress. The threshold stress is composed of rate-independent and rate-dependent parts,

$$\kappa^\alpha = \kappa_c^\alpha + \kappa_e^\alpha \tag{3.6}$$

The rate-independent portion of the threshold stress is,

$$\kappa_c^\alpha = \kappa_0(\mathrm{T}) + h_{pe}\tau_{pe}^\alpha + h_{se}\tau_{se}^\alpha + h_{cb}|\tau_{cb}^\alpha| \tag{3.7}$$

where the non-Schmid factors, $h_{pe}$, $h_{se}$, and $h_{cb}$, are contained, along with the temperature dependence, $\kappa_0$. The rate-dependent portion of the threshold stress,

$$\kappa_{\mathrm{e}}^{\alpha} = h_0 \sum_{\beta=1}^{\mathrm{N_{slip}}} q^{\alpha\beta} \left|\dot{\gamma}^{\beta}\right| - h_{\kappa s}\kappa^{\alpha} \sum_{\beta=1}^{\mathrm{N_{slip}}} \left|\dot{\gamma}^{\beta}\right| - h_s \Theta_{\kappa s}(\mathrm{T}) \langle \kappa^{\alpha} - \kappa_{\mathrm{th}} \rangle^{r_s} \tag{3.8}$$

captures the cyclic hardening of a material and is therefore related to the transient response between initial cycling and steady-state hysteresis. However, because the behavior of interest in this research is steady state behavior, which is important for fatigue life prediction, the rate-dependent equation is set to zero and the threshold stress is initially assumed to be constant. Finally the Arrhenius equation,

$$\Theta(\mathrm{T}) = \begin{cases} \exp\left(-\dfrac{Q_0}{\mathrm{RT}}\right) \ldots\ldots\ldots\ldots\ldots\ldots\ldots\ldots\ldots \mathrm{T} \geq \dfrac{\mathrm{T_m}}{2} \\ \exp\left(-\dfrac{2Q_0}{\mathrm{RT_m}}\left[\ln\left(\dfrac{\mathrm{T_m}}{2\mathrm{T}}\right) + 1\right]\right) \ldots\ldots \mathrm{T} \leq \dfrac{\mathrm{T_m}}{2} \end{cases} \tag{3.9}$$

can be found in Eq. (3.1) , Eq. (3.4), and Eq. (3.8) where the activation energy, $Q_0$ can be different in each case. However, this has been found unnecessary and a single Arrhenius equation is implemented in the model. These equations are summarized in Table 3.1.

Table 3.1: Summary of equations for the CVP model

$$\dot{\gamma}^{\alpha} = \dot{\gamma}_0 \Theta(\mathrm{T}) \left\langle \frac{\tau_{\mathrm{v}}^{\alpha}}{\mathrm{D}^{\alpha}} \right\rangle^{n} \exp\left\{ B_0 \left\langle \frac{\tau_{\mathrm{v}}^{\alpha}}{\mathrm{D}^{\alpha}} \right\rangle^{n+1} \right\} \mathrm{sgn}\left(\tau^{\alpha} - \chi^{\alpha}\right)$$

Where $\tau_{\mathrm{v}}^{\alpha} = |\tau^{\alpha} - \chi^{\alpha}| - \kappa^{\alpha} \frac{\mu}{\mu_0}$ and $\mathrm{D}^{\alpha} = D_0 \frac{\mu}{\mu_0}$

$$\Theta(\mathrm{T}) = \begin{cases} \exp\left(-\dfrac{Q_0}{\mathrm{RT}}\right) \dots\dots\dots\dots\dots\dots\dots\dots \mathrm{T} \geq \dfrac{\mathrm{T_m}}{2} \\ \exp\left(-\dfrac{2Q_0}{\mathrm{RT_m}}\left[\ln\left(\dfrac{\mathrm{T_m}}{2\mathrm{T}}\right) + 1\right]\right) \dots\dots \mathrm{T} \leq \dfrac{\mathrm{T_m}}{2} \end{cases}$$

Evolution Equations:

Back Stress:

$$\dot{\chi}^{\alpha} = h_{\chi}|\dot{\gamma}^{\alpha}| - h_{\chi\mathrm{d}}|\dot{\gamma}^{\alpha}|\chi^{\alpha} + \left(\frac{1}{R_{\chi}}\frac{\partial R_{\chi}}{\partial \mathrm{T}} + \frac{1}{h_{\chi}}\frac{\partial h_{\chi\mathrm{d}}}{\partial \mathrm{T}}\right)\chi^{\alpha}\dot{\mathrm{T}} - h_{\chi\mathrm{s}}\Theta_{\chi\mathrm{s}}(\mathrm{T})|\chi^{\alpha}|^{r_{\chi\mathrm{s}}}\chi^{\alpha}$$

where $R_{\chi} = \frac{h_{\chi}}{h_{\chi d}}$

Threshold Stress:

$$\kappa^{\alpha} = \kappa_{\mathrm{c}}^{\alpha} + \kappa_{\mathrm{e}}^{\alpha}$$

$$\kappa_{\mathrm{c}}^{\alpha} = \kappa_0(\mathrm{T}) + h_{\mathrm{pe}}\tau_{\mathrm{pe}}^{\alpha} + h_{\mathrm{se}}\tau_{\mathrm{se}}^{\alpha} + h_{\mathrm{cb}}|\tau_{\mathrm{cb}}^{\alpha}|$$

$$\kappa_{\mathrm{e}}^{\alpha} = h_0 \sum_{\beta=1}^{\mathrm{N_{slip}}} q^{\alpha\beta}\left|\dot{\gamma}^{\beta}\right| - h_{\kappa s}\kappa^{\alpha} \sum_{\beta=1}^{\mathrm{N_{slip}}} \left|\dot{\gamma}^{\beta}\right| - h_s \Theta_{\kappa\mathrm{s}}(\mathrm{T})\langle \kappa^{\alpha} - \kappa_{\mathrm{th}} \rangle^{r_s}$$

The superscript α in each of the equations represents a slip system. The CVP model uses eighteen slip systems (Shenoy et al., 2002): twelve octahedral $\{111\}\langle 110\rangle$, and six cubic $\{100\}\langle 110\rangle$ slip systems where some of each are depicted in Figure 3.2. This is based upon the cubic crystal structure of Ni-base superalloys. Since the octahedral slip systems are more closely packed than the cubic slip systems most of the dislocation motion occurs on theses slip systems and they are active over the entire temperature range. Dislocation motion along the cubic slip systems has been observed at high homologous temperatures although there is speculation about the exact nature of this mechanism. Bettge and Osterle (1999) have shown that the slip on these planes is actually caused by zigzag motion of dislocations on octahedral planes in a cubic slip channel as shown in Figure 3.3. In the model's implementation, however, it is assumes that slip is occurring on the cubic slip systems when activated, and therefore has separate parameters for these slip systems. The activation of any slip system occurs when the critical resolved shear stress exceeds the threshold stress. When a slip system becomes active the flow rule is utilized to determine the rate of inelastic strain needed to satisfy dynamic equilibrium.

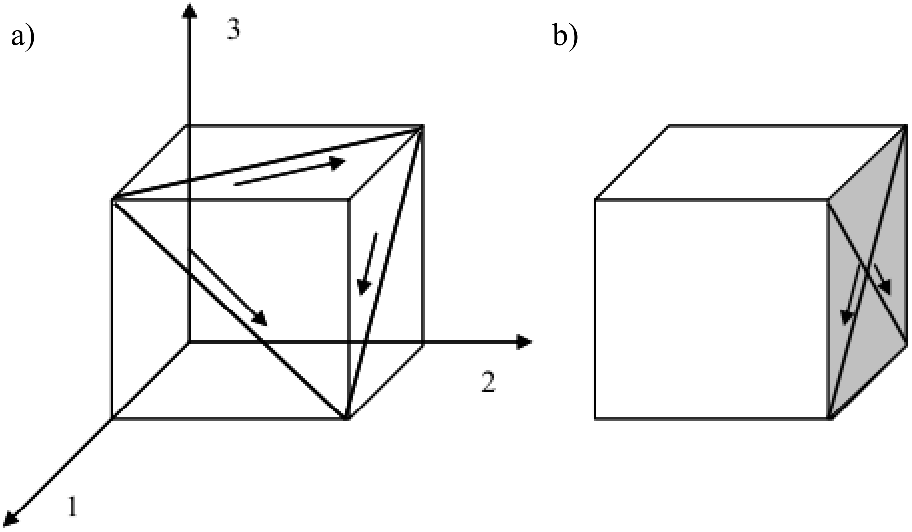

Figure 3.2: (a) Octahedral slip systems and (b) Cubic slip systems. Note that only one plane for each type is shown (Shenoy, 2006)

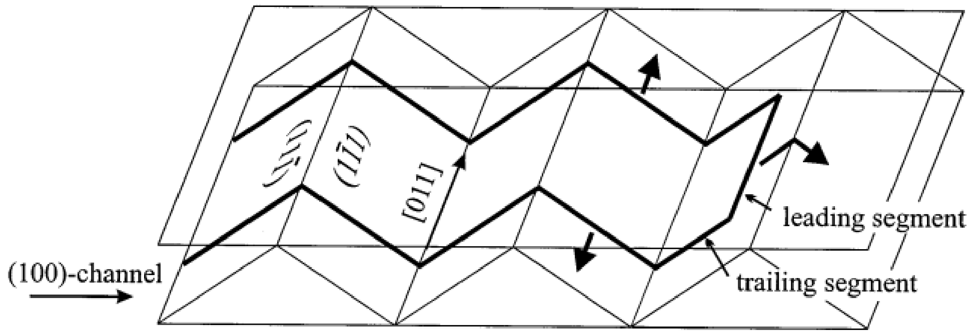

Figure 3.3: Zigzag motion of dislocation slip in cubic channels (Bettge and Osterle, 1999)

As stated above, the non-Schmid effects are accounted for through the threshold stress. Schmid's law states that a slip system is potentially active when the resolved shear stress on the slip plane in the slip direction (the Schmid stress) reaches a critical value, the CRSS. However in Ni-base superalloys other shear components also affect the mobility of dislocations at high homologous temperatures (Qin and Bassani, 1992b). If the yield surface is assumed to be symmetric in tension and compression then the critical shear stress depends on a single extra shear stress, $\tau_{cb}$. If there is a tension-compression asymmetry then there are two additional terms, $\tau_{pe}$ and $\tau_{se}$. $\tau_{pe}$ is the shear stress on a primary octahedral slip plane, $\tau_{se}$ is the shear stress on a secondary octahedral slip plane, and $\tau_{cb}$ is the shear stress on the {100} cross-slip plane (Qin and Bassani, 1992a). Figure 3.4 shows the orientation of each shear stress (Qin and Bassani, 1992b). The size of the yield surface is affected by $h_{cb}$ while $h_{pe}$ and $h_{se}$ shift the position of the yield surface. This can be clearly seen since the absolute value is only taken for $\tau_{cb}$ in Eq. (3.7). The effect of the non-Schmid factors is shown in Figure 3.5 where $h_{pe}$ has been set to a small value.

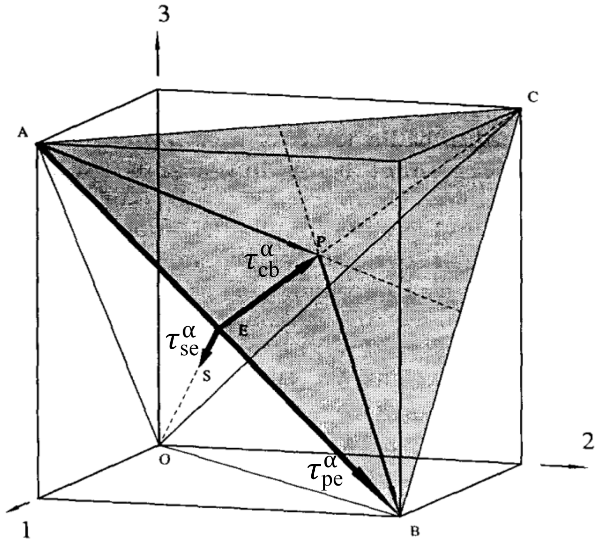

Figure 3.4: Orientation of non-Schmid shear stresses (Qin and Bassani, 1992b)

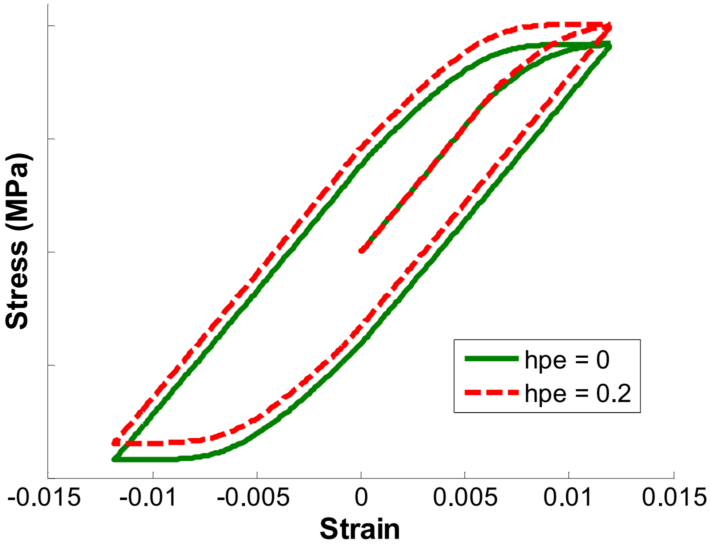

Figure 3.5: Effect of $h_{\mathrm{pe}}$ on a cyclic hysteresis loop

## 3.2 Crystal Viscoplasticity Model Implementation

The model is implemented in ABAQUS v6.9 as a User MATerial subroutine (UMAT). The UMAT from the work of McGinty (2001) was modified by Shenoy (2006) for the implementation of the CVP model used in this work. However, the UMAT that Shenoy employed was not written for efficient modification of parameter values. Thus the UMAT was modified to allow rapid modification of parameters to aid in rapid calibration. Additionally, the UMAT contained errors in implementation that were corrected during this project. All of these changes and others can be found listed in Appendix A. Since the UMAT has been updated some of the parameter values for GTD-111 (Shenoy et al., 2006; Shenoy, 2006) will no longer yield correct results with the current UMAT. Specifically any threshold stress evolution parameters, non-Schmid factors, or threshold stress temperature dependence will no longer produce with the new UMAT a model response which corresponds to any data. Because of this disparity subsequent use of the term UMAT will only refer to the modified version used in this work except where expressly stated.

The UMAT is fully implicit and uses $\dot{\gamma}$ as the starting point shown in Figure 2.4. The initial inelastic shear strain rate is assumed to be zero and the state of stress is estimated by an elastic increment. To do this the strain it is given must first be converted into a deformation gradient through Eq. (2.4). To simulate an isothermal loading history the state of total strain at a point in time is given and the UMAT linearly interpolates the strain and time from its original deformation state to the final state. Predicting thermal deformations requires the inclusion of the thermal strain. The thermal deformation gradient is therefore found through Eq. (2.5). In both isothermal and temperature-dependent cases the amount of mechanical deformation that is plastic is determined using a fully implicit algorithm with a combined Newton-Raphson and linear search algorithm for rapid convergence to a solution (McGinty, 2001). The elastic portion of the mechanical deformation gradient is finally determined from the other deformation gradients,

$$\mathbf{F}^{\mathrm{e}} = \mathbf{F}^{\mathrm{Tot}} \cdot \mathbf{F}^{\theta^{\mathrm{T}}} \cdot \mathbf{F}^{\mathrm{p}^{\mathrm{T}}} \tag{3.10}$$

Three Euler angles, $\varphi_1$, $\Phi$, and $\varphi_2$, are used in the UMAT to describe the orientation of the crystal structure with respect to the loading. The Roe convention, as defined by McGinty (2001), is used where the first rotation is about the global Z-axis, the second rotation is about the new local Y'-axis, and the final rotation is about the new local Z'' axis as shown in Figure 3.6. Loading can be specified along any of the original axes, however with this angle definition it is convenient to apply loads in the original y-direction, Y. A rotation can then orient the material coordinate system such that loading is applied in an arbitrary direction with respect to the material coordinates. Since the model uses cubic symmetry the direction of solidification can be set in any of the three material coordinate axes, X, Y, and Z, with caveat that the angles are defined appropriately. Since determination of Euler angles for a specific loading direction is not trivial Appendix B has been included to assist in finding these angles.

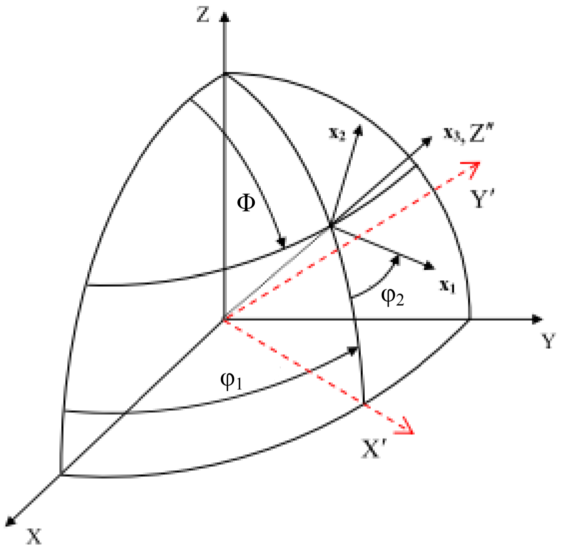

Figure 3.6: Euler angle convention (McGinty, 2001)

For analyses containing multiple grains, which is required for non-longitudinal loading in DS alloys, the UMAT uses the Taylor approximation to describe the interaction between grains. This method is shown in Figure 3.7 (Shenoy, 2006) where the arrows represent grain orientations. Rather than representing individual grains in a geometric model, multi grain simulations are performed by considering a unit cube with one orientation at a time. The same total deformation is then applied to each grain, which allows the simplification of the intergranular constraints because there are no strain discontinuities between grains. Because the grain orientations are unique the stress for each grain is dissimilar from any other. The global stress is found by taking the average of the stresses from each grain.

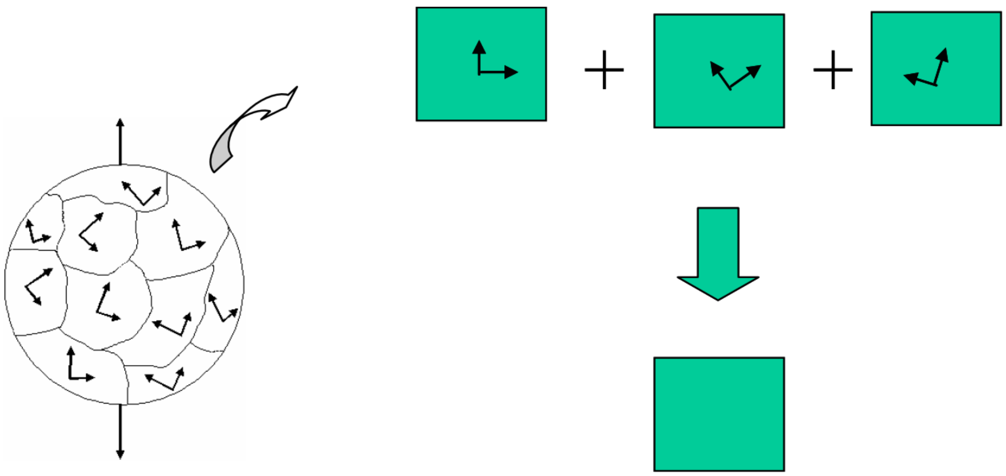

Figure 3.7: Taylor approximation for grain interactions (Shenoy, 2006)

## 3.3 Model Parameters

The model parameters for GTD-111 (Shenoy et al., 2005) are listed in Table 3.2. They have been arranged by equation with the parameters in the flow rule shown together, back stress parameters shown next, threshold stress parameters listed next, and elastic constants and Euler angles listed last. As mentioned previously the modifications to the UMAT may cause these parameter values to yield incorrect results. Specifically, modifications to the UMAT have antiquated the threshold stress parameters. All other parameter values are still valid however. The largest group by far in the table is the threshold stress, but as explained above, most of these parameters are assumed to be identically zero. All of these model parameters are inserted into an ABAQUS input file and run as a simulation. Appendix C gives a detailed description of the input file and each of the required fields. Appendix C also contains for reference a list of model parameters and code variables with the form of their temperature-dependence specified.

Table 3.2: Model parameters and GTD-111 values

| Parameter | Parameter name | GTD-111 value |
|---|---|---|
| $\dot{\gamma}_0$ | Reference inelastic shear strain rate | 1.15e9 ($s^{-1}$) |
| $D_0$ | Drag stress | 102 (MPa) |
| $n$ | Flow exponent | f(T) |
| $B_0$ | Rate independent drag stress modification | 0.05 |
| $\mu$ | Shear modulus | $= C_{44}$ |
| $\mu_0$ | Shear modulus at 0K | 166000 (MPa) |
| $Q_0$ | Dislocation activation energy | 309000 (KJ/mol) |
| $T_m$ | Melting temperature | 1699 K |
| $\chi^\alpha$ | Back stress | - |
| $h_\chi$ | Hardening coefficient | 4th order polynomial |
| $h_{\chi d}$ | Dynamic recovery coefficient | f($h_\chi$, $R_\chi$) |
| $R_\chi$ | Steady state back stress for high $\dot{\gamma}$ | 4th order polynomial |
| $h_{\chi s}$ | Static thermal recovery coefficient | Exponential |
| $r_{\chi s}$ | Static thermal recovery exponent | Quadratic polynomial |
| $\kappa^\alpha$ | Threshold stress | - |
| $\kappa_0^\alpha(T)$ | Threshold stress temperature dependence | Two 4th order polynomials |
| $h_{pe}$ | Primary slip system non-Schmid factor | Quadratic polynomial |
| $h_{se}$ | Secondary slip system non-Schmid factor | Quadratic polynomial |
| $h_{cb}$ | Cubic slip system non-Schmid factor | Quadratic polynomial |
| $h_0$ | Rate of evolution of threshold stress coeff. | 0 |
| $q^{\alpha\alpha}$ | Sensitivity of $\kappa^\alpha$ to $\dot{\gamma}^\alpha$ | 1 |
| $q^{\alpha\beta}$ | Sensitivity of $\kappa^\alpha$ to $\dot{\gamma}^\beta$ | 1.4 |
| $h_{\kappa s}$ | Threshold stress dynamic recovery term | 0 |
| $h_s$ | Static thermal recovery coefficient | 0 |
| $\kappa_{th}$ | Threshold stress recovery threshold | 0 |
| $r_s$ | Static thermal recovery exponent | 0 |
| $C_{11}$ | Stiffness constants | Quadratic polynomial |
| $C_{12}$ | | Quadratic polynomial |
| $C_{44}$ | | Quadratic polynomial |
| $\varphi_1$ | First Euler angle | Function of orientation |
| $\Phi$ | Second Euler angle | Function of orientation |
| $\varphi_1$ | Third Euler angle | Function of orientation |

Additional input parameters are required for the analysis of multiple grains. Since Euler angles for each grain are required, the number of Euler angles input to the model would exceed ninety for simulations containing more than thirty grains. Rather than input these angles directly they are specified in a text file in units of degrees. The location of the text file is then specified inside the UMAT. Appendix B shows more detail on how this is accomplished.

# Chapter 4. Protocols for Rapid Parameter Determination

Calibrating the model across a temperature range is challenging without an in-depth knowledge of the model and its behavior because the parameters must behave smoothly with respect to temperature to prevent anomalous kinks in the response and to improve convergence. Thus if temperature dependent material parameters are desired it is necessary to develop methods and protocols which act as guidelines for parameter determination. The process depends on the specific functional relationships of one CVP model as well as the class of material being calibrated. These protocols are established for the Shenoy et al. (2005) model, described in Chapter 3, and Ni-base superalloys. The flow of this chapter is shown in Figure 4.1 where a grouping of parameters is first presented which reduces the perceived interdependencies between parameters. Next a dual level hierarchical ranking of groups and parameters is presented which defines a systematic path for parameter determination. This is followed by defining a specific type of data for the calibration of each parameter. The calibration of the model to an isothermal temperature is then explicitly demonstrated. Finally the determination of temperature-dependent parameters from isothermal values is illustrated. First, however, a brief overview of the process will be given.

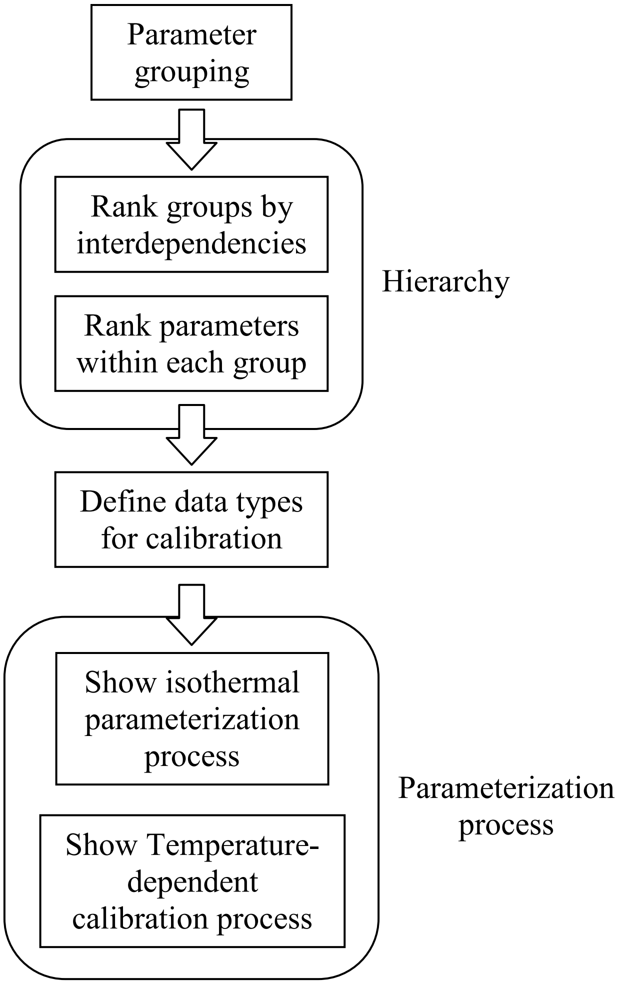

Figure 4.1: Strategy for parameterization

The process for isothermal parameter determination is shown in further detail in Figure 4.2. The threshold stress is calibrated first, along with $R_\chi$ and $h_\chi$, to match the yield and saturation stresses. The flow exponent is determined next using creep or stress relaxation data, and the threshold stress and steady state back stress are mathematically adjusted to account for the change in *n*. The drag stress is the next parameter to be determined, and the strain rate dependence is used in this case along with the hardening behavior. Again $\kappa$ and $R_\chi$ are mathematically adjusted to retain the calibration to the yield and saturation stresses. Finally $\dot{\gamma}_0$ is determined using the strain rate dependence. As will be shown this procedure reduces the interdependencies experienced between parameters and allows the rapid determination of parameters for isothermal temperatures.

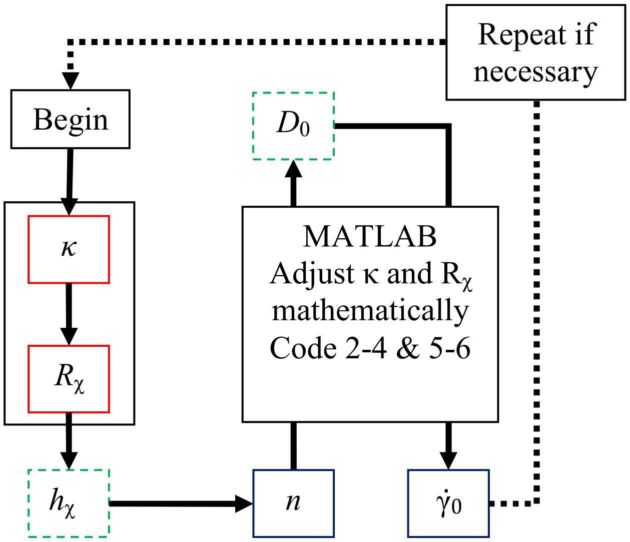

$B_0$ and $Q_0$ cannot be determined
using a single temperature

Figure 4.2: Flow diagram for isothermal parameter determination

The methodology for developing temperature-dependent parameters from the isothermal parameters is shown in Figure 4.3. As shown, the isothermal parameters are first converted to polynomials. These parameter values, especially those for $\kappa_0$ and $R_\chi$, typically do not follow smooth polynomial behavior and the dashed-dotted line represents adjustments in these parameters to create polynomials which better reflect their behavior. The dislocation activation energy, $Q_0$, is then determined, and $\dot{\gamma}_0$ is mathematically adjusted to maintain the calibration at the highest temperature. The limit of the quasi-rate independent region is then calibrated through $B_0$. Finally the isothermal experiments are predicted with the new temperature dependent parameters and checked for consistency with experimental data. If the isothermal calibrations are satisfactory with this new parameter set then the calibration is complete. Otherwise the isothermal parameterizations are reinitialized and the process is repeated.

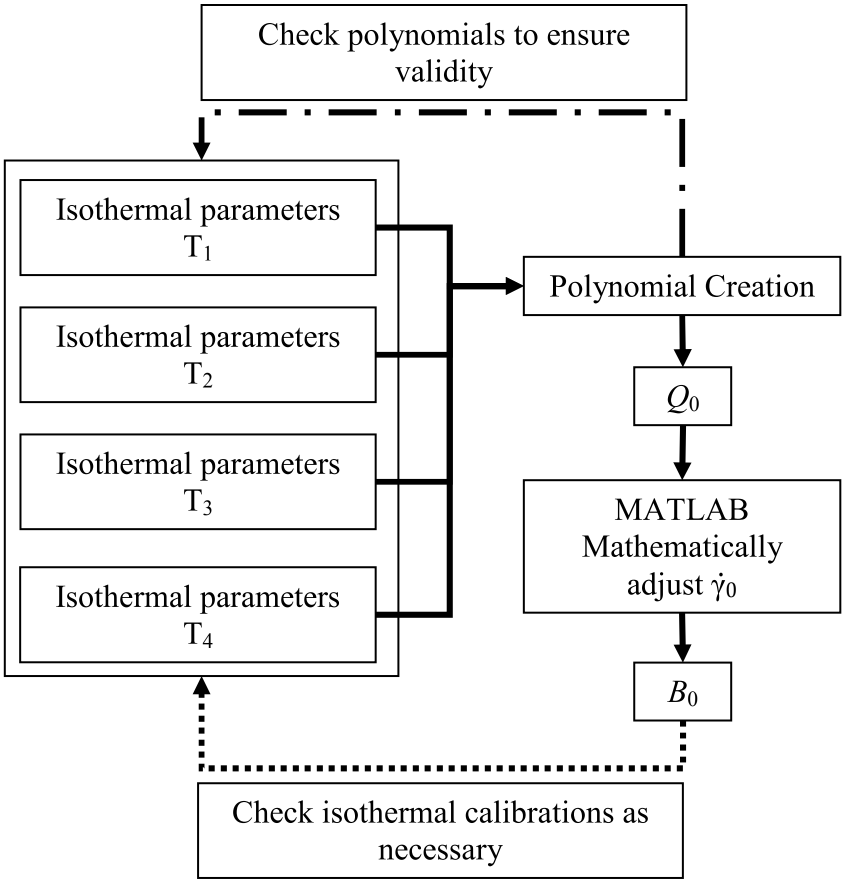

Figure 4.3: Process flow diagram for temperature-dependent parameter determination

## 4.1 Parameter Grouping

The grouping of parameters by relation and dependence is the first step towards model calibration. This grouping allows the separation of parameters for parameterization and reduces the interdependencies observed during model calibration. Therefore the following groups are formed so that the interaction between parameters in separate groups is minimized.

*Group 1: Elastic Constants and Coefficient of Thermal Expansion;* $C_{11}$, $C_{12}$, $C_{44}$, *and* $\beta$

The elastic constants are the most important group of parameters. Every other group depends on this group, with only small changes in stiffness leading to significant changes in the amount of cyclic inelastic strain. The thermomechanical fatigue response also relies heavily on these parameters since the material response of Ni-base superalloys tends to be mostly elastic even when life is considered in the low cycle fatigue regime. This dependency is twofold. First any evaluation of the error between a model prediction and an experiment will contain additional error from the mismatch in moduli if the stiffness constants are incorrect. Secondly, the shape of the hysteresis loop for temperature-dependent, as well as isothermal, simulations is highly sensitive to the stiffness constants because of the accumulated affect of any error. This is demonstrated in Figure 4.4 where the only difference is the stiffness constants. Thus it is of the utmost importance that this group not only be parameterized with precision but also that the methods of doing so be well understood.

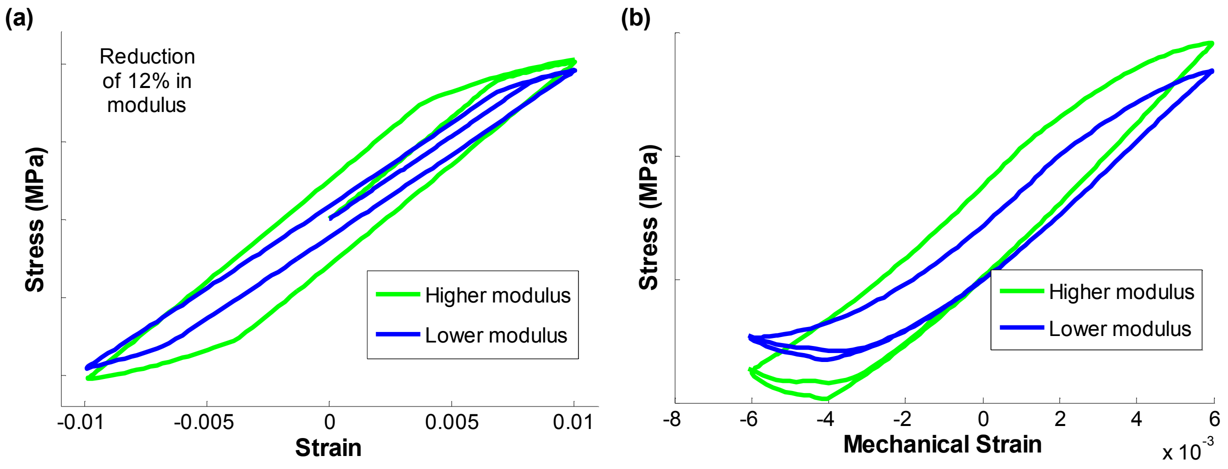

Figure 4.4: Effect of modulus on cyclic hysteresis loops for (a) an isothermal prediction and (b) an out of phase TMF prediction from 100 °C to 950 °C

The first set of parameters in this group is the stiffness constants, $C_{11}$, $C_{12}$, and $C_{44}$. Since each parameter is assumed to be best fit by a second order polynomial there are nine total parameters associated with these three variables.

$$\mathrm{C}_{11} = C11\_1 * \mathrm{T}^2 + C11\_2 * \mathrm{T} + C11\_3 \tag{4.1}$$

$$\mathrm{C}_{12} = C12\_1 * \mathrm{T}^2 + C12\_2 * \mathrm{T} + C12\_3 \tag{4.2}$$

$$\mathrm{C}_{44} = C44\_1 * \mathrm{T}^2 + C44\_2 * \mathrm{T} + C44\_3 \tag{4.3}$$

The temperature, T, must be in units of Kelvin since the UAMT assumes that this is what is given. This is true for all other temperature-dependent inputs as well. The procedure for determining these values is different for single crystals and DS specimens and will be discussed in a further section.

The coefficient of thermal expansion (CTE) is the next parameter in this group. It is placed here since it has a considerable influence on the proper simulation of temperature-dependent loadings, but is affected by none of the other parameters. The CTE is allotted four coefficients for a third order polynomial,

$$\beta = ec1 * \mathrm{T}^3 + ec2 * \mathrm{T}^2 + ec3 * \mathrm{T} + ec4 \tag{4.4}$$

because its behavior is slightly ill fit by a quadratic polynomial. Again, the temperature must be in Kelvin.

Table 4.1 shows the input parameters contained in this group. Note that the shear modulus is entered twice: once for $C_{44}$ and once for $\mu$. In theory the drag stress should scale with the shear modulus (Shenoy, 2006), however the implementation in the UMAT allows the drag stress to scale to a separate polynomial. This was not found to be necessary during the calibration to DS-CM247LC. Note also that the shear modulus at 0K, $\mu_0$, is set equal to *C44_3*. Since there is in general no data available for the shear modulus at temperatures even near 0K, the value of this parameter cannot be set experimentally. Thus to initialize this parameter the polynomial for the shear modulus can be extrapolated to room temperature. In general extrapolation of a polynomial outside of the calibration data by one third of the total calibrated range is not a good practice since the behavior of polynomials is notoriously unpredictable outside of the calibrated range. However since the polynomial for this parameter is in general very smooth the extrapolation of its polynomial should result in an acceptable approximation of the shear modulus at 0K. This may not be valid in all cases and the behavior of the polynomial for the shear modulus should therefore be checked for smoothness prior to implementing this relationship. The UMAT allows for a quadratic fit to each parameter since the elastic constants tend to behave smoothly.

Table 4.1: Group 1 parameters and inputs

| Parameter | UMAT variables | Suggested Value |
|---|---|---|
| $C_{11}$ | *C11_1* | NA |
| | *C11_2* | |
| | *C11_3* | |
| $C_{12}$ | *C12_1* | |
| | *C12_2* | |
| | *C12_3* | |
| $C_{44}$ | *C44_1* | |
| | *C44_2* | |
| | *C44_3* | |
| $\mu$ | *pmeuc1* | C44_1 |
| | *pmeuc2* | C44_2 |
| | *pmeuc3* | C44_3 |
| $\mu_0$ | *pmeu_zero* | C44_3 |
| $\mathrm{T}_\mathrm{m}$ | *Tmelt* | NA |
| $\beta$ | *ec1* | NA |
| | *ec2* | |
| | *ec3* | |
| | *ec4* | |

### *Group 2: Yield Stress;* $\kappa_0$*, and* $\mathrm{R}_\chi$

The yield stress is an important parameter to calibrate accurately because it controls the stress at which the rest of the plasticity parameters become active. Therefore the calibration of every other group, with the exception of those in Group 1, depends heavily on this group. The yield stress group consists of two main parameters, $\kappa_0^\alpha(\mathrm{T})$, and $R_\chi$. These control the point where the material stress-strain response transitions from a purely elastic behavior to one which includes plastic deformation through dislocation motion. Additional parameters are the non-Schmid factors $h_{\mathrm{pe}}$, $h_{\mathrm{se}}$, and $h_{\mathrm{cb}}$, which capture asymmetry of the yield surface and can be used to model the orientation dependence of the yield surface.

The temperature dependence of the threshold stress, $\kappa_0^\alpha(\mathrm{T})$, is one of the more difficult parameters to fit a polynomial through. Because of the anomalous yielding behavior which Ni-base superalloys exhibit there is an increase in this parameter at temperatures near 750 °C and a sharp decrease in its value afterwards (Reed, 2006). This sharp transition from a gradually increasing parameter to a rapidly decreasing trend causes it to be ill-fitted for representation by a single polynomial. Therefore this parameter is allotted two polynomials: one to capture the temperature dependent behavior between room temperature and around 750 °C and another to capture the rapidly decreasing behavior above at high temperatures.

$$\kappa_0^\alpha(\mathrm{T})_{\mathrm{low}} = \mathit{g0\_l1} * \mathrm{T}^4 + \mathit{g0\_l2} * \mathrm{T}^3 + \mathit{g0\_l3} * \mathrm{T}^2 + \mathit{g0\_l4} * \mathrm{T} + \mathit{g0\_l5} \tag{4.5}$$

$$\kappa_0^\alpha(\mathrm{T})_{\mathrm{high}} = \mathit{hg0\_1} * \mathrm{T}^4 + \mathit{hg0\_2} * \mathrm{T}^3 + \mathit{hg0\_3} * \mathrm{T}^2 + \mathit{hg0\_4} * \mathrm{T} + \mathit{hg0\_5} \tag{4.6}$$

The subscripts “low” and “high” designate the low and high temperature polynomials, respectively, and the temperature, T, is in Kelvin. The transition temperature between these two polynomials is controlled through an input parameter, $T_{\mathrm{trans}}$. These two polynomials should not only have identical values at this transition temperature but also similar slopes. Therefore, when creating these two polynomials, it is important to choose their behavior in such a way as to encourage such a transition. Data from the longitudinal direction should be used to calibrate this parameter since the activity of cubic slip systems can cause the yield stress to vary with orientation.

The non-Schmid factors, $h_{\mathrm{pe}}$, $h_{\mathrm{se}}$, and $h_{\mathrm{cb}}$ for the threshold stress capture the dependence of dislocation motion on non-Schmid shear stresses. Specifically the glissile to sessile core transformation is affected by shear stresses on primary cross slip planes, $\tau_{\mathrm{pe}}$, secondary cross slip planes, $\tau_{\mathrm{se}}$, and the cubic plane, $\tau_{\mathrm{cb}}$ (Qin and Bassani, 1992b). Since their effect is the shift or expansion/contraction of the yield surface based upon orientation, which is in general small compared to the temperature dependence of the threshold stress, they are less important than $\kappa_0^\alpha(\mathrm{T})$. If they are excluded from the initial parameterizations then the threshold stress may be slightly incorrect in different orientations, but the responses should not significantly differ from experimental data in the longitudinal direction. Also if they are excluded the anisotropy of the saturation stress will not be captured in any orientation, but again this effect is in general small. To calibrate these parameters fully, experimental data from the longitudinal direction, where octahedral slip systems are exclusively active, and the transverse or other off-axis orientation direction, where cubic slip has been activated, is required.

$R_\chi$ is the magnitude of the steady state value of the back stress. This can be clearly seen by examining the back stress evolution equation in Eq. (3.4). Since for isothermal analyses the temperature rate, $\dot{\mathrm{T}}$, is zero and since at high strain rates the static thermal recovery, $\Omega_\chi^\alpha$, is negligibly small these can both be neglected. Inserting $R_\chi$ in for $\chi^\alpha$ results in,

$$\dot{\chi}^\alpha = h_\chi|\dot{\gamma}^\alpha|\mathrm{sgn}(\tau^\alpha - \chi^\alpha) - h_{\chi\mathrm{d}}\left[R_\chi\right]|\dot{\gamma}^\alpha| \tag{4.7}$$

$$\dot{\chi}^\alpha = h_\chi|\dot{\gamma}^\alpha|\mathrm{sgn}(\tau^\alpha - \chi^\alpha) - h_{\chi\mathrm{d}}\left[\frac{h_\chi}{h_{\chi\mathrm{d}}}\mathrm{sgn}(\tau^\alpha - \chi^\alpha)\right]|\dot{\gamma}^\alpha| \tag{4.8}$$

$$\dot{\chi}^\alpha = h_\chi|\dot{\gamma}^\alpha|\mathrm{sgn}(\tau^\alpha - \chi^\alpha) - h_\chi\mathrm{sgn}(\tau^\alpha - \chi^\alpha)|\dot{\gamma}^\alpha| = 0 \tag{4.9}$$

where the rate of evolution of the back stress, $\dot{\chi}^\alpha$, is easily seen to go to zero. Thus when the magnitude of the back stress is equal to $R_\chi$ the back stress has reached saturation and thus $R_\chi$ is the saturation value of the back stress at high strain rates. This parameter is easily determined then by matching the saturation stress of experimental data at high strain rates.

Table 4.2 shows the input parameters for the yield group. Each of the non-Schmid factors is given a quadratic polynomial,

$$h_{\mathrm{pe}} = h\_pe1 * \mathrm{T}^2 + h\_pe2 * \mathrm{T} + h\_pe3 \tag{4.10}$$

$$h_{\mathrm{se}} = h\_se1 * \mathrm{T}^2 + h\_se2 * \mathrm{T} + h\_se3 \tag{4.11}$$

$$h_{\mathrm{cb}} = h\_cb1 * \mathrm{T}^2 + h\_cb2 * \mathrm{T} + h\_cb3 \tag{4.12}$$

where again the temperature is in Kelvin. The polynomial for $R_\chi$,

$$R_\chi = Rx\_1 * \mathrm{T}^4 + Rx\_2 * \mathrm{T}^3 + Rx\_3 * \mathrm{T}^2 + Rx\_4 * \mathrm{T} + Rx\_5 \tag{4.13}$$

also must be in units of Kelvin, and generally has been found to increase to around 850 °C and then gradually decrease for NI-base superalloys.

Table 4.2: Group 2 parameters and inputs

| **Parameter** | **UMAT variables** | **Range of Values** |
|---|---|---|
| $R_\chi$ | *Rx_1* | 0-200 MPa |
| | *Rx_2* | |
| | *Rx_3* | |
| | *Rx_4* | |
| | *Rx_5* | |
| $\kappa_0^\alpha(\mathrm{T})_{\mathrm{low}}$ | *g0_l1* | 0-200 MPa |
| | *g0_l2* | |
| | *g0_l3* | |
| | *g0_l4* | |
| | *g0_l5* | |
| $\kappa_0^\alpha(\mathrm{T})_{\mathrm{high}}$ | *hg0_1* | 0-200 MPa |
| | *hg0_2* | |
| | *hg0_3* | |
| | *hg0_4* | |
| | *hg0_5* | |
| $h_{\mathrm{pe}}$ | *h_pe1* | 0-0.3 |
| | *h_pe2* | |
| | *h_pe3* | |
| $h_{\mathrm{se}}$ | *h_se1* | 0-0.3 |
| | *h_se2* | |
| | *h_se3* | |

Table 4.2 (continued)

| **Parameter** | **UMAT variables** | **Range of Values** |
|---|---|---|
| $h_{\text{cb}}$ | *h_cb1* | 0-0.3 |
| | *h_cb2* | |
| | *h_cb3* | |
| $R_{\chi}^{\text{cub}}$ | *R_x_oct* | 100-200 MPa |
| $T_{\text{trans}}$ | *T_trans* | 1023K |

*Group 3: Hardening;* $h_\chi$*, and* $D_0$

The hardening group contains the most sensitive parameters, $h_\chi$ and $h_{\chi d}$ (Shenoy, 2006). However, in this parameterization $h_{\chi d}$ is controlled indirectly through $R_\chi$,

$$R_\chi = \frac{h_\chi}{h_{\chi\text{d}}} \tag{4.14}$$

which has already been placed in Group 2. An additional parameter in this group is the drag stress, $D_0$, which affects hardening by normalizing the shear stress on each slip system.

The rate of back stress evolution, $h_\chi$, controls the rate at which the back stress, and therefore the stress, reaches its saturation value. A high value for this parameter can seem to extend the elastic region of the simulation, while a very small value can cause a sharp transition immediately following the yield point with slow, almost linear, hardening afterward as is shown in Figure 4.5. This parameter should be calibrated by matching the rate of evolution of the back stress at high strain rates.

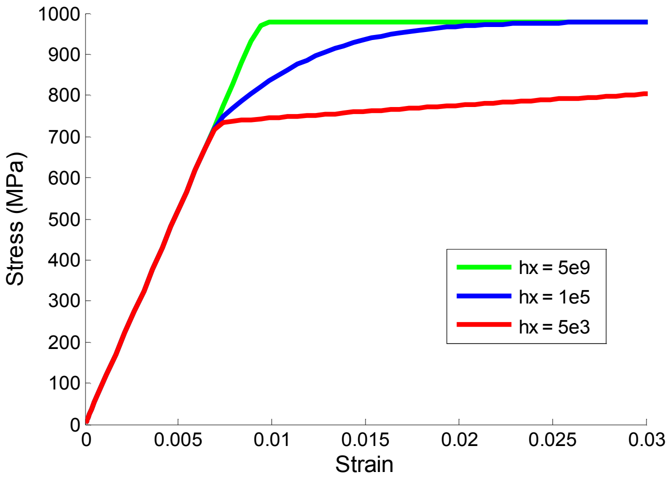

Figure 4.5: Effect of $h_\chi$ on back stress evolution

The drag stress, $D_0$, is included in this group because it determines the sensitivity of the model to changes in the viscous overstress. It captures the component of flow resistance which is possible to overcome with the addition of thermal energy (Shenoy, 2006). A large value of the drag stress will cause a change in the viscous overstress to result in a smaller change in the inelastic shear strain rate, $\dot{\gamma}$, than a low drag stress. Confusion may be generated by the placement of this parameter in the hardening group since in most recent CVP models it is used as a yield parameter. The use of the drag stress in this manner can be justified through examination Figure 4.6 where the yield stress is elevated when the drag stress is increased. However, examination of the literature shows that it is also utilized as a hardening parameter (Asaro, 1983) as well as a viscous parameter (Nouailhas, 1989). The effect on hardening can also be seen in Figure 4.6, where as the drag stress increases the amount of hardening after yield is increased. Its effect as a viscous parameter is demonstrated in Figure 4.7 where the lines are isothermal values of the flow rule. Therefore the drag stress has been grouped as a hardening parameter since this is the data type by which it was found to be most easily determined.

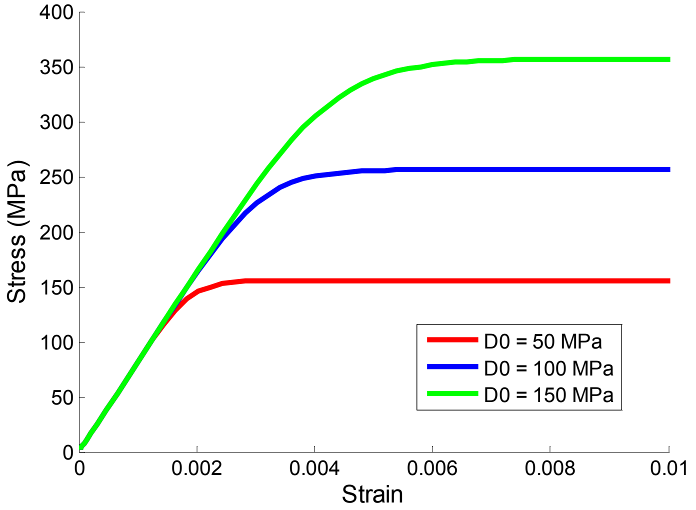

Figure 4.6: Effect of $D_0$ on a model prediction without back stress

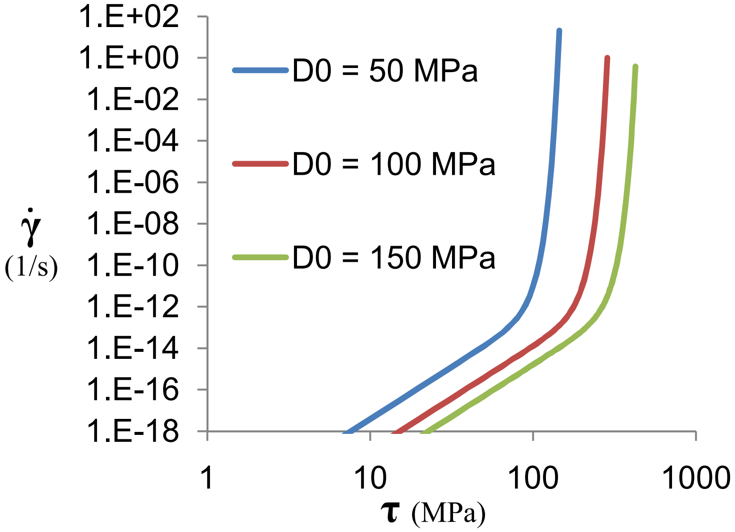

Figure 4.7: Effect of $D_0$ on the flow rule

The hardening parameters are shown in Table 4.3 with their associated input variables. $h_\chi$ is allowed five inputs corresponding to a 4th order polynomial,

$$h_\chi = h\_x1 * \mathrm{T}^4 + h\_x2 * \mathrm{T}^3 + h\_x3 * \mathrm{T}^2 + h\_x4 * \mathrm{T} + h\_x5 \tag{4.15}$$

The drag stress however has a single variable since its temperature dependence is controlled through the shear modulus as shown in Eq. (3.2).

Table 4.3: Group 3 parameters and inputs

| Parameter | UMAT variables | Range of values |
|---|---|---|
| $h_\chi$ | *h_x1* | $1\text{x}10^4$ – $5\text{x}10^5$ MPa |
| | *h_x2* | |
| | *h_x3* | |
| | *h_x4* | |
| | *h_x5* | |
| $h_\chi^{\text{cub}}$ | *hx_oct* | $1\text{x}10^4$ - $1\text{x}10^5$ MPa |
| $D_0$ | *d_zero* | 80 - 120 MPa |
| $D_0^{\text{cub}}$ | *d_zero_oct* | 40 - 80 MPa |

*Group 4: Flow Rule;* n, $\dot{\gamma}_0$, $Q_0$, *and* $B_0$

The flow rule group consists of parameters that can be found in Eq. (3.1). These parameters govern the strain rate dependence of the CVP model and are crucial for both capturing the strain rate dependence of experimental data and for generating accurate predictions of strain rates outside of the calibrated range.

The first parameter in this group is the flow exponent, *n*. As can be clearly seen in Figure 4.8, the value of *n* greatly affects the stress-strain relationship. Consider a test specimen experiencing plastic deformation of $\dot{\gamma} = 1 \times 10^{-4}$ 1/s, and assume that the temperature is sufficiently high to place this strain rate in the creep regime.

$$1 * 10^{-4} = \dot{\gamma}_0 \Theta \left(\frac{\tau_v^\alpha}{D^\alpha}\right)^n \tag{4.16}$$

If all other flow rule parameters are constant the viscous overstress, $\tau_v^\alpha$, must be large for Eq. (4.16) to be satisfied for small values of *n*. Similarly, $\tau_v^\alpha$ must be smaller for large values of *n* to achieve the same inelastic shear strain rate. Thus the model will predict a lower stress for a higher flow exponent if all other parameters remain constant.

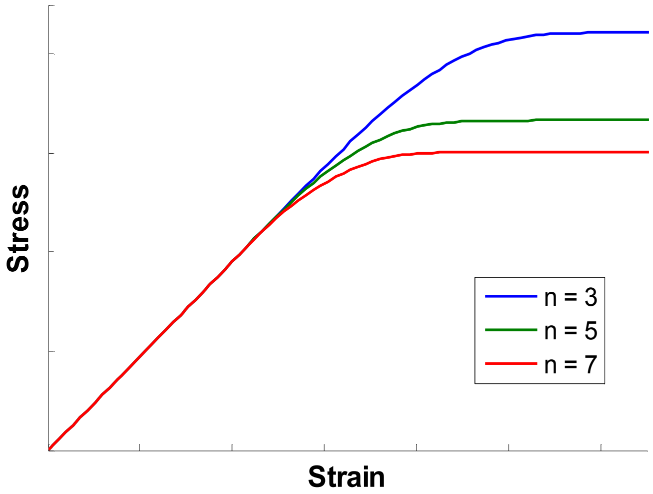

Figure 4.8: Effect of *n*, keeping all else constant

As the temperature increases the strain rate dependence should increase which corresponds to a decrease in the flow exponent. Finding values for *n* that fit a smooth function is somewhat less difficult than for the back stress and threshold stress parameters because the model is less sensitive to this parameter and so the tolerance is larger. The behavior of *n* with respect to temperature should conform to the following trends: It should be fairly flat in the rate insensitive region between room temperature and 650 °C. At the other extreme, as the material approaches its melting temperature it will tend towards behaving as a Newtonian fluid ($n = 1$). In addition to these constraints, the model assumes that this parameter is constant outside the range of a range set within the UMAT. The temperature-dependence of this parameter is therefore implemented through a 3rd order polynomial.

$$n = \mathit{flow\_exp1} * \mathrm{T}^3 + \mathit{flow\_exp2} * \mathrm{T}^2 + \mathit{flow\_exp3} * \mathrm{T} + \mathit{flow\_exp4} \tag{4.17}$$

where the temperature is in Kelvin. The polynomial should have a slope of zero at both of these temperatures so that the transition from the temperature dependent behavior to the constant value is smooth. Figure 4.9 shows an acceptable polynomial for the flow exponent, *n*.

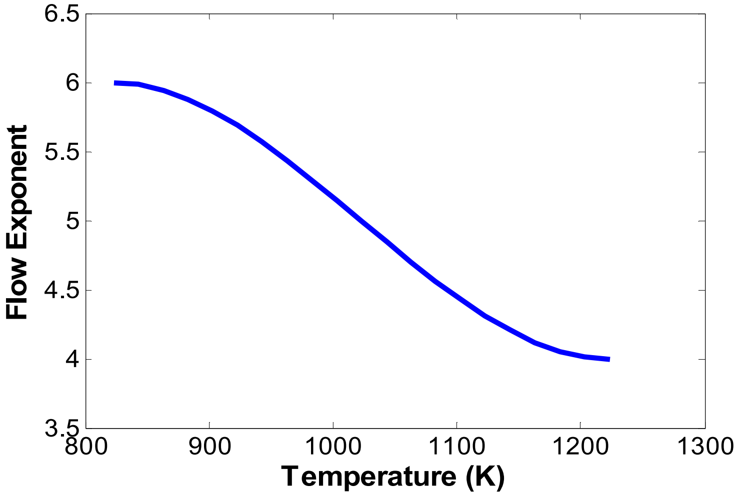

Figure 4.9: Proper polynomial for *n*

The next parameter in this group is $B_0$ which is a unitless quantity in the flow rule exponential. This parameter has its most pronounced effect on the fastest strain rates since it modifies the exponential term of the flow rule. Its effect on the flow rule is to shift the rate insensitive region to the left and right, as shown in Figure 4.10, while leaving the steady state creep region undisturbed. It can be thought of as a modification to the drag stress for the exponential term. Since the parameter is not in itself temperature dependent it should be set using the lowest temperature and fastest strain rate where the response is known to be rate insensitive.

Note that the value of this parameter should never be greater than unity. Also note that as the parameter is decreased it becomes less sensitive.

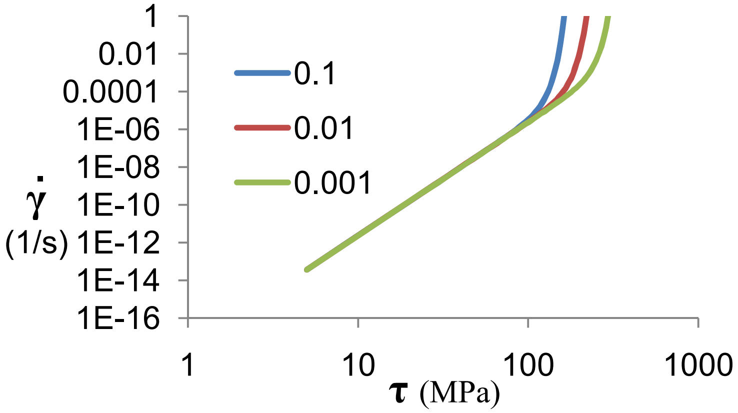

Figure 4.10: Effect of $B_0$ on flow rule

The final two parameters in this group are the reference inelastic shear strain rate, $\dot{\gamma}_0$, and the dislocation activation energy, $Q_0$. The effect of these two parameters is very distinct from that of any other. $\dot{\gamma}_0$ has the effect of shifting the entire flow rule up or down on the plot shown in Figure 4.11 by increasing or decreasing its value respectively. $Q_0$ also has a similar affect on this plot, but in addition it has the effect of increasing or decreasing the separation of the isothermal lines in Figure 3.1. The dislocation activation energy should be initially set to the experimental dislocation activation energy where available. Usually this is a starting point, however, and its value should be adjusted to give correct observed temperature dependence of the strain rate.

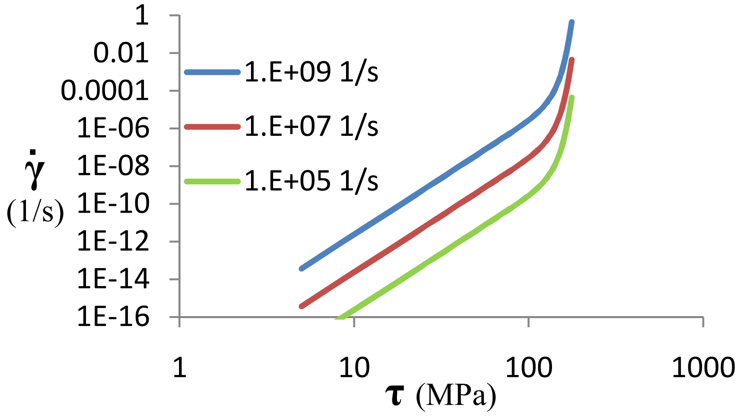

Figure 4.11: effect of $\dot{\gamma}_0$

The parameters listed in this group are shown in Table 4.4. They are listed in order sensitivity in the model. The flow exponent, *n*, causes large changes in other parameters based upon changes in its value which is why it is listed first. $\dot{\gamma}_0$ and $Q_0$ are next since they are important for capturing the strain rate dependence for all stresses. Finally $B_0$ is listed last since it only affects the rate insensitive region of the flow rule.

Table 4.4: Group 4 parameters and inputs

| **Parameter** | **UMAT variables** | **Range of values** |
|---|---|---|
| *n* | *flow_exp1* | 3-10 |
| | *flow_exp2* | |
| | *flow_exp3* | |
| | *flow_exp4* | |
| $\dot{\gamma}_0$ | *gamma_dot_zero* | $10^5$ - $10^{10}$ 1/s |
| $Q_0$ | *q_energy* | $2.5\text{x}10^5$ – $5.0\text{x}10^5$ MPa |
| $B_0$ | *b_zero* | 0.001 - 1 |
| $B_0^{cub}$ | *B_zero_oct* | 0.001 - 1 |

### *Group 5: Creep;* n, $h_{\chi s}$, *and* $r_{\chi s}$

The creep group is the final group. Since creep behavior is only significant at very slow strain rates (≈1.0x$10^{-5}$/s), it can be neglected at the higher strain rates while the other material parameters are determined. Once the model is behaving correctly at the faster strain rates, its creep behavior should be adjusted.

Parameters that most affect creep behavior are the flow exponent, $n$, and the back stress static thermal recovery variables, $h_{\chi s}$ and $r_{\chi s}$. The back stress terms are the most sensitive variables, but care must be taken to not only model the stress relaxation behavior, but also the very slow cycling behavior. This is because the back stress can be modified through $h_{\chi s}$ and $r_{\chi s}$ to model the relaxation behavior, but this is not valid if the stress-strain response is not correct afterwards. Figure 4.12 illustrates a correctly calibrated model with a region of stress relaxation denoted as Region 1. Note that if only the back stress is used to calibrate the model to the creep behavior in Region 1, it may diverge from the desired response in Region 2 shown on the figure since the static thermal recovery of the back stress could cause its saturation level to be significantly lower than that needed for calibration of the saturation stress.

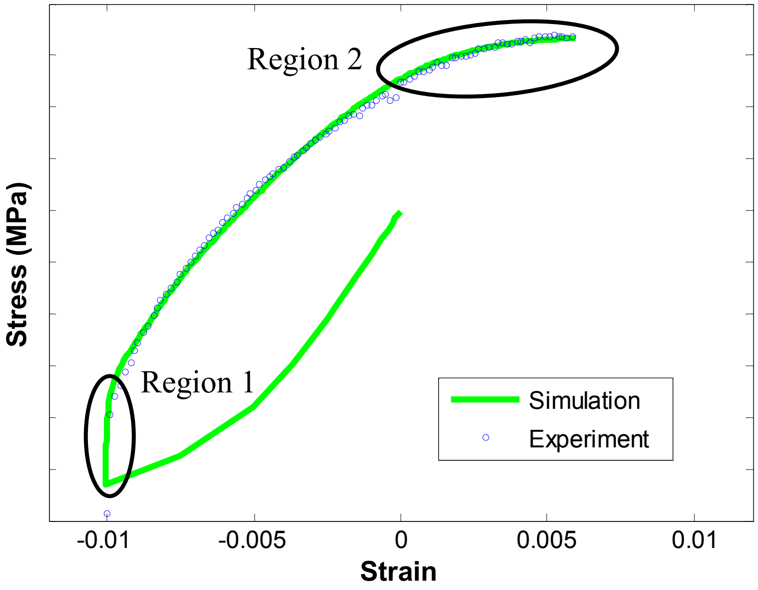

Figure 4.12: Creep behavior of DS-CM247LC

The creep group parameters are listed in Table 4.5. Each of the back stress static thermal recovery parameters is given three inputs. However the static thermal recovery coefficient, $h_{\chi s}$, is modeled as an exponential

$$h_{\chi s} = h\_xs1 + h\_xs2 * e^{h\_xs3 * \mathrm{T}} \tag{4.18}$$

while $r_{\chi s}$ is fit with a quadratic polynomial,

$$r_{\chi s} = r\_xs1 * \mathrm{T}^2 + r\_xs2 * \mathrm{T} + r\_xs3 \tag{4.19}$$

Table 4.5: Group 5 parameters and inputs

| **Parameter** | **UMAT variables** | **Range of values** |
|---|---|---|
| $n$ | *flow_exp1* | 3-10 |
| | *flow_exp2* | |
| | *flow_exp3* | |
| | *flow_exp4* | |
| $h_{\chi\mathrm{s}}$ | *h_xs1* | NA |
| | *h_xs2* | |
| | *h_xs3* | |
| $r_{\chi\mathrm{s}}$ | *r_xs1* | 1-4 |
| | *r_xs2* | |
| | *r_xs3* | |
| $h_{\chi\mathrm{s}}$ | *h_xs_oct* | NA |
| $r_{\chi\mathrm{s}}^{\mathrm{cub}}$ | *r_xs_oct* | 1-4 |

## 4.2 Hierarchical Ranking of Groups and Parameters

After having grouped parameters by function and dependencies it is necessary to define an order of parameterization. This is done by examining the CVP model's sensitivity to changes in parameter values and the number of interdependencies which exist in each parameter.

Taking the first criterion, each group is ranked by the percent change in each parameter required to cause a significant change a model prediction, where a significant change is defined as the difference in stress for cyclic calculations relative to the same percent change in the threshold stress. Since the model is very sensitive to the yield stress and hardening groups these are ranked first according to this criterion. The elastic constants and CTE are ranked next. Finally the flow rule is next to last and the creep group is least sensitive.

Taking the second criterion, each parameter group is ranked by the number of parameters outside of its group upon which it depends. Figure 4.13 shows the interdependencies which exist between groups where an arrow pointing towards a group indicates that the parameters at the end of the arrow depend on parameters at the beginning of the arrow. Dashed arrows indicate a weaker dependence than solid arrows. The elastic constants do not depend on any other group, but every other group depends on this group. Therefore the elastic constants are ranked first by this criterion. The yield stress and hardening groups both have the same number of dependencies, but the strength of these dependencies differs so that the yield group is ranked before the hardening group.  The groups with the most dependencies are the flow rule and creep groups, however the creep group affects fewer groups and so is ranked lower.

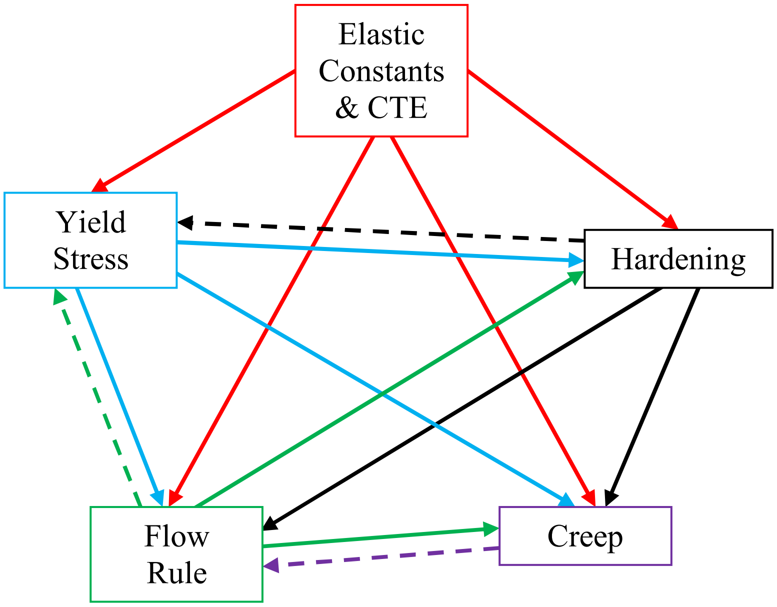

Figure 4.13: Interdependencies between parameter groups

The combined ranking from these two criterion results in weighting the elastic constants and CTE first, yield and then hardening groups next, flow rule group next, and finally the creep group.

Evaluating the parameters in each group is the next step towards creating the dual level hierarchy. Considering the elastic constants and CTE, the CTE can be neglected for isothermal analyses and therefore is ranked below the elastic constants. In the yield group the threshold stress is calibrated first so that the saturation back stress value, $R_\chi$, can be correctly calibrated. In the hardening group the rate of evolution of the back stress, $h_{\chi s}$, is calibrated first. However the consideration of the drag stress, $D_0$, presents a quandary since it depends strongly on the flow exponent, $n$. Therefore the order of groups is violated slightly by determining the value of $n$ before determining $D_0$. The next parameter to be considered is $\dot{\gamma}_0$ since it depends most heavily on the drag stress. Finally the creep parameters are determined; first $r_{\chi s}$ and then $h_{\chi s}$. This is shown in Figure 4.14 where the thicker arrow emphasizes the jump between groups mentioned previously.

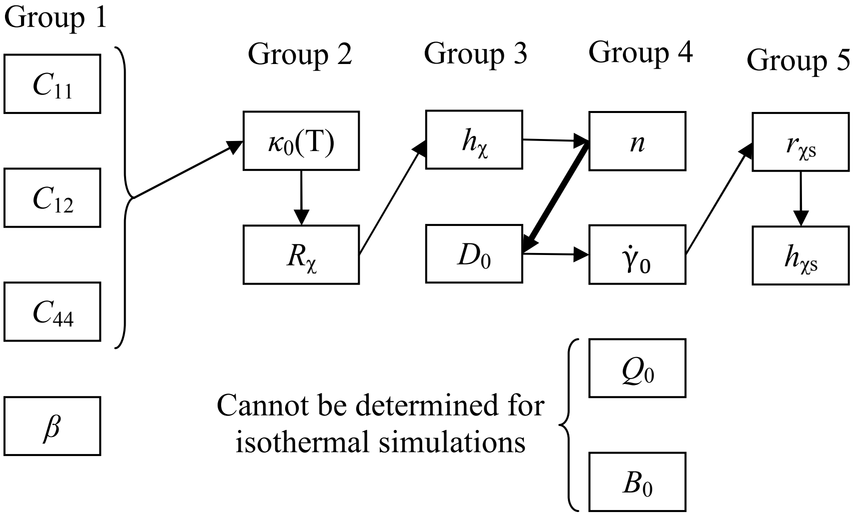

Figure 4.14: Hierarchical path for rapid parameter determination

However this hierarchical grouping method, as shown in Figure 4.14, would neglect the interdependencies between parameters by not adjusting them based upon calibration parameters upon which they depend. Therefore a set of scripts and functions has been written which corrects specific parameters based upon changes in other parameters. The flow diagram for this implementation is shown in Figure 4.15 where the dashed lines indicate the use of codes to modify $\kappa_0$ and $R_\chi$. These codes were implemented in MATLAB and can be found in Appendix D.

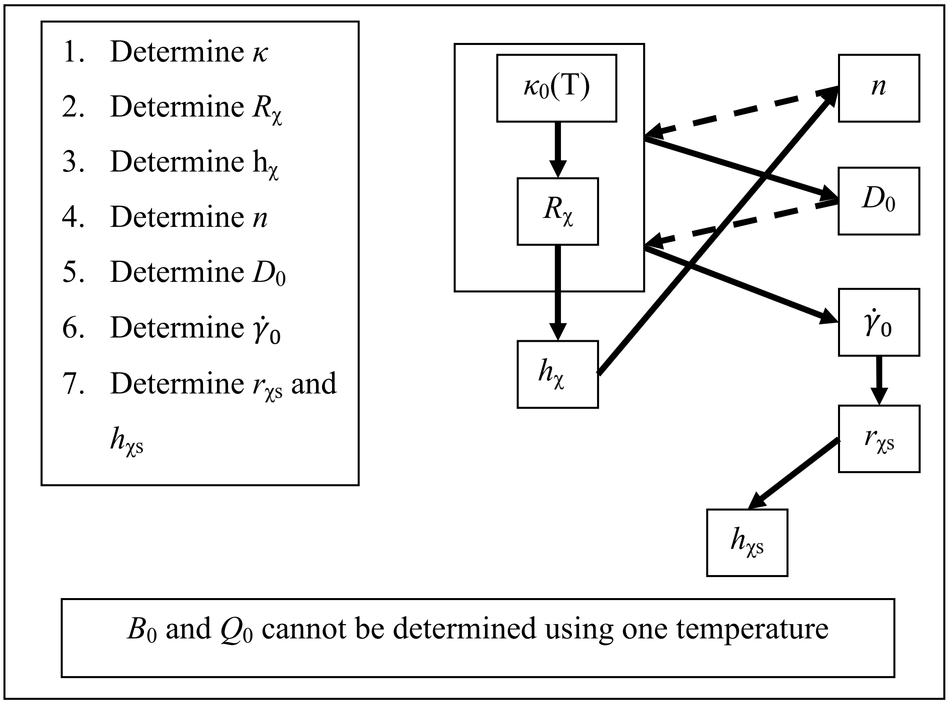

Figure 4.15: Process flow for an isothermal parameterization

## 4.3 Definition of Data Types for Parameter Determination

In the calibration of parameters of the CVP model it is necessary to define sections of data to which each parameter is most sensitive. These can then be used in the calibration of separate parameters so that multiple parameters are not determined using identical data which would cause interdependencies to be accentuated. Firstly, the elastic portions of an experiment are used to determine the modulus of elasticity. Moduli in multiple directions are needed to find the stiffness constants. The shear modulus can be found either from additional off-axis testing or torsion experiments. Calibration of the threshold stress requires the initialization of plastic deformation. Therefore the yield stress of an experiment is determined using a tight offset and this value is used to calibrate the threshold stress. The saturation back stress, $R_\chi$, needs experimental data with high strain rates where the saturation stress is clearly showing. The rate of back stress evolution requires knowledge of the hardening behavior of the material and so requires the section of data between yield and saturation. The flow exponent requires creep holds or stress relaxation data. For creep holds a sufficiently high strain rate must be used prior to the hold so that there is a significant amount of creep. Stress relaxation data is easily collected by switching from a fast strain rate to a slow strain rate or a strain hold. Calibration of the drag stress requires knowledge of the size of the inelastic flow potential. The calibration of $B_0$ requires data with a strain rate sufficiently high to access the rate insensitive region of the flow rule. The calibration of $\dot{\gamma}_0$ is accomplished by correctly calibrating the saturation stresses for a range of strain rates. Similarly the dislocation activation energy, $Q_0$, is calibrated to the saturation stresses of several strain rates, but in this case multiple temperatures are required. The creep parameters, $h_{\chi s}$ and $r_{\chi s}$, are calibrated to creep or stress relaxation data, but are done so by matching the change in magnitude of the back stress between the beginning of the creep hold and its end. This is done by first measuring the displacement of the yield surface for cyclic hysteresis loops without strain or stress holds. Then the displacement of the yield surface is found after a hold. The difference between the two is due to static thermal recovery of the back stress and can be used to calibrate $h_{\chi s}$ and $r_{\chi s}$. However multiple creep hold times are needed for this implementation, which is infeasible given other testing constraints which will be discussed later in this work. Therefore these terms are calibrated using the saturation stress of very slow strain rates.

To summarize the above data requirements:

- Modulus of elasticity in two directions, and shear modulus or Poisson's ratio
- Appreciable yielding
- Saturated hardening
- Creep or stress relaxation
- Minimum of three strain rates, each an order of magnitude different

## 4.4 Isothermal Parameter Determination

Since it is difficult to isolate parameters in a TMF experiment, isothermal experiments are used to determine internal state variable evolution and to calibrate the temperature-dependence of the CVP model. These parameter values are then combined with the result being temperature-dependent parameter behavior. Isothermal parameter determination is therefore crucial to finding temperature-dependent parameters. The order of parameter determination is defined in section §4.2 and the data from which each parameter is determined is identified in §4.3. Therefore this section shows in detail the methodology used for determining isothermal parameters. Note that since the simulations are all isothermal during the initial parameter determination, it is unnecessary to input all of the coefficients of the temperature-dependent polynomials. By adjusting only the last coefficient of the polynomial and setting the rest to zero the number of input parameters is reduced to around twenty. Once parameter values have been determined for all temperatures, polynomials can be created and used in subsequent parameter calibration.

### *Group 1: Elastic Constants and Coefficient of Thermal Expansion;* $C_{11}$, $C_{12}$, $C_{44}$, *and* $\beta$

As mentioned previously there are separate methods for finding the elastic stiffness constants for SC and DS alloys. For single crystal specimens the stiffness values can be obtained from the elastic modulus, *E*, Poisson's ratio, *v*, and the shear modulus, *G*. The stiffness tensor, **C** is the inverse of the compliance tensor, **S**, which is shown in Figure 4.16 (Mucke and Bernhardi, 2003) for cubic symmetry. Therefore the stiffness constants can be easily found by inserting *E*, *v*, and *G* into **S** and inverting the tensor. Alternatively the same process can be employed through

$$C_{11} = \frac{E * (1 - \nu)}{(1 + \nu) * (1 - 2\nu)} \tag{4.20}$$

$$C_{12} = \frac{E * \nu}{(1 + \nu) * (1 - 2\nu)} \tag{4.21}$$

$$C_{44} = G \tag{4.22}$$

which are the equations that result from inverting **S**.

$$\begin{bmatrix} 1/E & -v/E & -v/E & 0 & 0 & 0 \\ -v/E & 1/E & -v/E & 0 & 0 & 0 \\ -v/E & -v/E & 1/E & 0 & 0 & 0 \\ 0 & 0 & 0 & 1/G & 0 & 0 \\ 0 & 0 & 0 & 0 & 1/G & 0 \\ 0 & 0 & 0 & 0 & 0 & 1/G \end{bmatrix}$$

Figure 4.16: Equations for material compliance tensor, *S*, for cubic symmetry (Mucke and Bernhardi, 2003)

For DS alloys, which are transversely isotropic, the procedure above cannot be used to obtain the stiffness constants because Poisson's ratio measured between the transverse and longitudinal directions is not equivalent to the one measured between principal lattice directions. The equations for the elastic and shear moduli are (Kuhn and Sockel, 1989),

$$\frac{1}{E_{\theta,\rho}} = S_{11} - 2(S_{11} - S_{12} - 0.5 * S_{44}) * J \tag{4.23}$$

$$\frac{1}{G_{\theta,\rho}} = S_{11} + 4(S_{11} - S_{12} - 0.5 * S_{44}) * J \tag{4.24}$$

where,

$$J = \sin^2(\theta)\cos^2(\theta) + \frac{\sin^4(\theta)}{8}[1 - \cos(4\rho)] \tag{4.25}$$

and the angles θ and ρ are defined as in Figure 4.17. The elastic modulus in the longitudinal direction, $E_L$, and the shear modulus measured in the longitudinal direction, $G_L$, can easily be found by inserting $\theta = 0$ and $\rho = 0$ into Eq. (4.25) and then evaluating Eq. (4.23) and (4.24), respectively. This results in,

$$\frac{1}{E_L} = S_{11} \tag{4.26}$$

$$\frac{1}{G_L} = S_{44} \tag{4.27}$$

Evaluating the elastic modulus in the transverse direction requires setting $\theta = 90°$ and integrating over ρ from 0-90°,

$$E_T = \int_{0}^{45°} \frac{d\rho}{S_{11} - 2(S_{11} - S_{12} - 0.5 * S_{44}) * J} \tag{4.28}$$

However, this leads to the formula,

$$E_T = \left(E_L E_{(011)}\right)^{1/2} \tag{4.29}$$

where $E_{(011)}$ is the modulus in the [0 1 1] direction. Inserting Eq. (4.23), with $\theta = 45$ and $\rho = 0$, into Eq. (4.29) results in,

$$\mathrm{E_T} = \left(\frac{8\mathrm{G_L E_L}}{6\mathrm{G_L} + \mathrm{E_L} + 2\mathrm{G_L E_L S_{12}}}\right)^{1/2} \tag{4.30}$$

Solving for the only remaining stiffness constant, $S_{12}$,

$$\mathrm{S_{12}} = \frac{2\mathrm{E_L}}{\mathrm{E_T}^2} - \frac{1}{2\mathrm{G_L}} - \frac{1}{\mathrm{E_L}} \tag{4.31}$$

Thus, the stiffness constants, $C_{11}$, $C_{12}$ and $C_{44}$, can be found to functions of only the elastic and shear moduli in the longitudinal direction and the elastic moduli in the transverse direction,

$$\begin{aligned} C_{11} &= \frac{\mathrm{S_{11}} + \mathrm{S_{12}}}{\mathrm{S_{11}}^2 + \mathrm{S_{11}S_{12}} - 2\mathrm{S_{12}}^2} \\ &= \frac{\mathrm{G_L E_L}^2 \mathrm{E_T}^2\left(\mathrm{E_T}^2 + 4\mathrm{G_L E_L}\right)}{\left(4\mathrm{G_L E_L}^2 - \mathrm{E_T}^2(\mathrm{G_L} + \mathrm{E_L})\right)\left(4\mathrm{G_L E_L}^2 - \mathrm{E_T}^2(4\mathrm{G_L} + \mathrm{E_L})\right)} \end{aligned} \tag{4.32}$$

$$\begin{aligned} C_{12} &= \frac{-\mathrm{S_{12}}}{\mathrm{S_{11}}^2 + \mathrm{S_{11}S_{12}} - 2\mathrm{S_{12}}^2} \\ &= \frac{\mathrm{G_L E_L E_T}^2\left(4\mathrm{G_L E_L}^2 - \mathrm{E_T}^2(2\mathrm{G_L} + \mathrm{E_L})\right)}{\left(4\mathrm{G_L E_L}^2 - \mathrm{E_T}^2(\mathrm{G_L} + \mathrm{E_L})\right)\left(4\mathrm{G_L E_L}^2 - \mathrm{E_T}^2(4\mathrm{G_L} + \mathrm{E_L})\right)} \end{aligned} \tag{4.33}$$

$$C_{44} = G \tag{4.34}$$

In the case of DS-CM247LC, $E_L$, $E_T$, and $G_L$ were supplied by Siemens and data obtained from the experiments performed were used to validate these values.

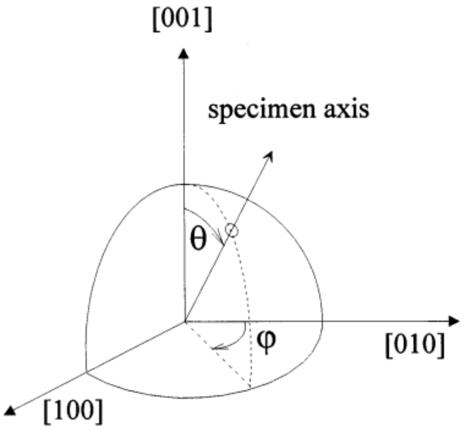

Figure 4.17: Definition of angles for elastic constant determination (Fahrmann et al., 1999)

The Coefficient of Thermal Expansion (CTE), $\beta$, is not needed for isothermal analyses so the procedure for determining this parameter is listed in the next section.

*Group 2: Yield Stress;* $\kappa_0$*, and* $R_\chi$

The parameters contained in this group are $R_\chi$, and $\kappa_0$. Since this group is the most sensitive to other parameters the values determined during the initial parameterization will be modified numerically based upon changes in other parameters. The calibration process is as follows.

The first parameter to be determined in this group should be the threshold stress, $\kappa_0$. Any experimental data set with cyclic plasticity can be used here, although slower strain rates are preferred since the hardening rate is much slower which causes the yield stress to be more clearly defined. The goal is to adjust the point where the model predicts initial yielding until it matches some yield criteria. A very tight yet resolvable offset of 0.02% is used for yield stress determination. Figure 4.18 shows the calibration of $\kappa_0$. The threshold stress can be estimated mathematically using the yield stress, however given the speed at which the model can be run it is usually more efficient to calibrate the threshold stress visually starting from a value of zero and working upwards. This is not true for simulations which require lengthy runtimes, however.

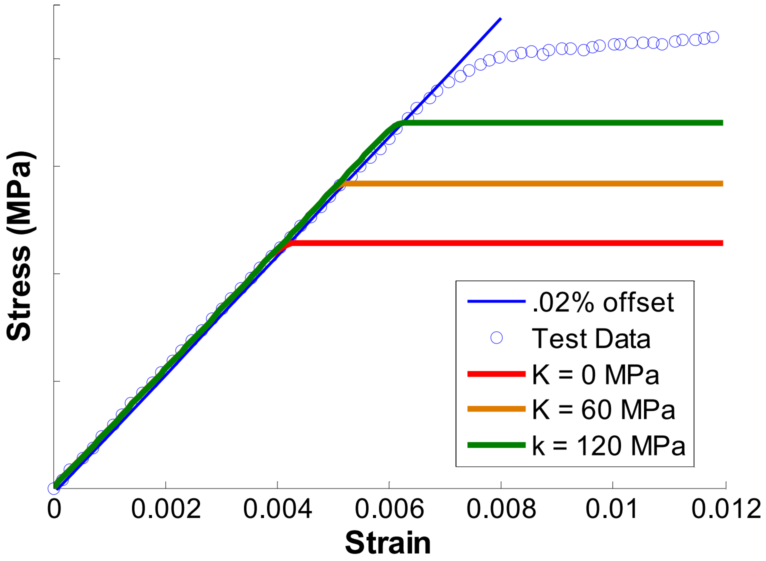

Figure 4.18: Calibration of $\kappa_0$ to normalized data

The steady state value of the back stress, $R_\chi$, is the next parameter in this group to be determined. This is found by setting $h_\chi$ to a very large number ($1.0\text{x}10^{10}$ MPa) and adjusting the value of $R_\chi$ until the saturation stress is matched. By setting $h_\chi$ to a large number the back stress evolves very quickly to its steady state. The evolution can be so fast in fact that the response appears elastic up until the saturation stress. The calibration is illustrated in Figure 4.19. To calibrate this parameter the fastest strain rate should be used since this data will not be biased by the inclusion of static thermal recovery of the back stress. The evolution equation for the back stress can, in the case of fast strain rates, be simplified to the first two terms as in Eq. (4.7) which simplifies the determination of $R_\chi$. If the data does not contain sufficient plastic deformation to achieve the saturation stress then the value of $R_\chi$ can still be determined, however it is more difficult. The easiest solution in this case is to extrapolate the data and make an educated guess as to what the saturation stress is and then calibrate to this extrapolation. Alternatively $R_\chi$ and $h_\chi$ can be simultaneously determined, but this is undesirable since it leads to a solution which is not unique.

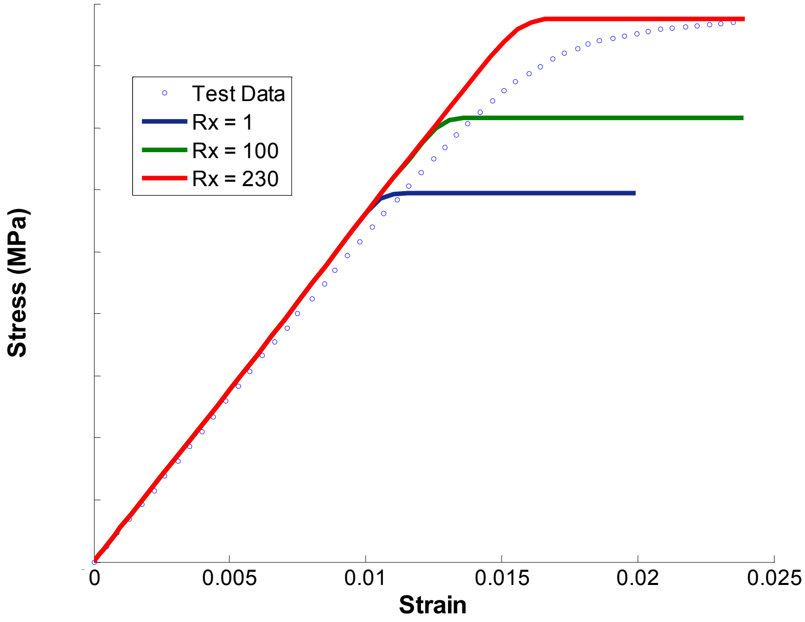

Figure 4.19: Calibration of $R_\chi$ to normalized data

As the magnitude of the steady state back stress, $R_\chi$ controls the maximum displacement of the yield surface. This means that the Bauschinger effect is controlled by this parameter. After calibration to the saturation stress this parameter should be checked to assure that yielding occurs in the correct location upon strain reversal. The locations indicated in the hysteresis loop shown in Figure 4.20 demonstrate the areas where this parameter has its most pronounced effect. The region of the hysteresis loop denoted by an ellipse targets where $R_\chi$ should be calibrated. The back stress also controls the Bauschinger effect, however, so the dashed circle contains the region where yielding should occur upon reversal.

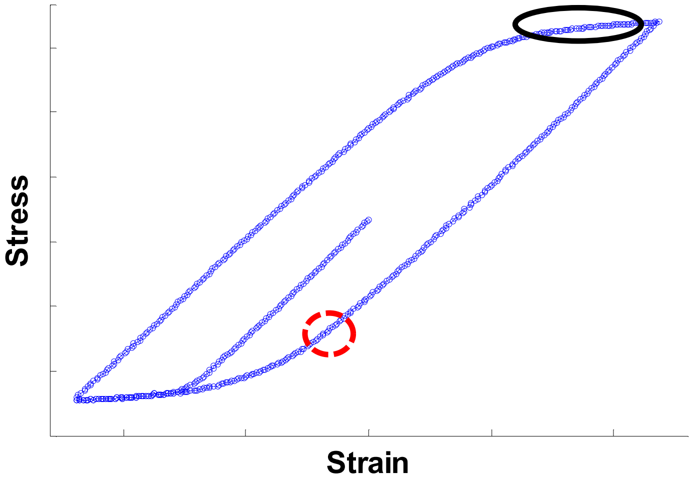

Figure 4.20: Calibration check of $R_\chi$

*Group 3: Hardening;* $h_\chi$, *and* $D_0$

The first parameter to be calibrated in this group is $h_\chi$. This parameter can be determined by slowly reducing its value from the value used during the calibration of $R_\chi$ until the hardening behavior is approximately correct. It is important to note that for the initial calibration this parameter should be determined with reasonable accuracy since its value was found to not change significantly with other parameters. Again, however, this parameter will be revisited as a final step in the calibration of the model.

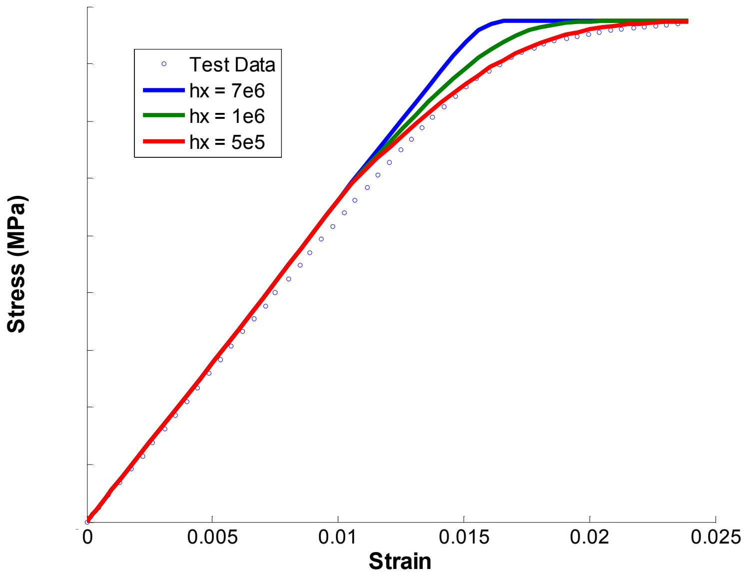

Figure 4.21: Calibration of $h_\chi$ to normalized data

The other parameter in this group, $D_0$, depends heavily on the flow exponent. Therefore it is determined after *n*. The drag stress should be determined such that the threshold stress at the highest tested temperature is positive. Looking at the flow rule in Eq. (3.1) it is noted that the drag stress is used to normalize the shear stress on a slip system. A large drag stress will allow a larger stress prior to appreciable yielding and a lower drag stress will cause the change in shear stress to be small for the same change in $\dot{\gamma}$. Using this behavior, the change in stress from yield to saturation and the hardening in between should be used to calibrate the drag stress. This should have already been calibrated using $R_\chi$, but the hardening behavior will be impossible to correctly calibrate if the drag stress is too high. Therefore the drag stress should be set to a value where the hardening is over predicted and then slowly decreased until the hardening behavior is adequately described and the saturation stress is accurate. This process requires numerical modification of $R_\chi$ and $\kappa_0$(T), and the scripts to accomplish this are shown in Appendix D.

*Group 4: Flow Rule;* n, $\dot{\gamma}_0$, $Q_0$, *and* $B_0$

The first parameter to be determined in this group is the flow exponent, *n*. It can be estimated using the saturation stress of several strain rates in experimental data if the inelastic shear strain rates lie in the power law regime of Figure 3.1. By plotting the saturation shear stress, $\tau_{sat}$, found through,

$$\tau_{\mathrm{sat}} = 0.4082483 * \sigma_{\mathrm{sat}} \tag{4.35}$$

for longitudinal experiments, versus the inelastic saturation shear strain rate, $\dot{\gamma}_{\mathrm{sat}}$, on a log-log plot it is possible to determine an approximate value for *n* as is shown in Figure 4.22 where the exponent in the trend line is the approximate value for *n*. The coefficient is the Schmid factor for [0 0 1]. However it is more accurate to determine the value of this parameter from creep data since at most temperatures there are not sufficient data points to construct *n* from the saturation stresses because the inelastic strain rates in the power law creep regime are too low. In this case the inelastic deformation can be plotted against the shear stress relaxation. It should follow a power law curve and a fit to this curve produces a value for the exponent. This method should be used with care, however, since the experimental data will contain the dynamic thermal recovery of the back stress which could bias the flow exponent.

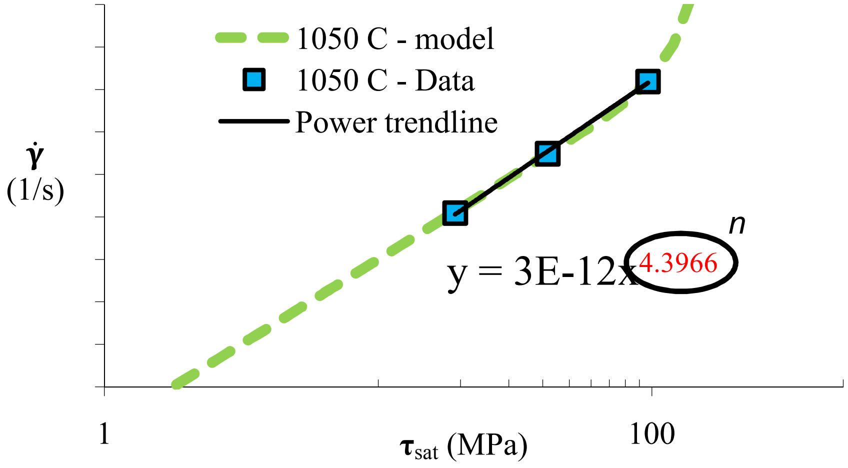

Figure 4.22: Calibration of *n* from saturation stresses at high temperatures

The next step is to determine the correct value for the combination of $\dot{\gamma}_0$and $Q_0$. Since this function is inherently temperature dependent the procedure used here is to determine a value of $\dot{\gamma}_0$which gives an appropriate value to the equation and correct later for the temperature dependence. To determine $\dot{\gamma}_0$ it is necessary to plot the flow rule on a log-log plot. The value of $\dot{\gamma}_0$ can shift the entire flow rule up and down on this plot as can be seen in Figure 4.11. The correct value of $\dot{\gamma}_0$ has been found when the flow rule, in the power law region, matches the data sufficiently well. Determining $Q_0$ requires multiple temperatures and the process for achieving this is described in the next section.

The final parameter to be determined in this group is $B_0$. This parameter should be set such that the rate insensitive region of the flow rule matches the behavior of the data as well as possible. It may be observed that at high temperatures the data may not enter the rate insensitive region fully. The value of $B_0$ should therefore be determined at low temperatures where the rate dependence is limited.

*Group 5: Creep;* n, $h_{\chi s}$*, and* $r_{\chi s}$

The parameters in this group are determined using creep and very slow strain rate data. Where available the values of $h_{\chi s}$ and $r_{\chi s}$ are determined using creep and stress relaxation from dwells in hysteresis loops. Since the back stress is recovered during periods of this nature it is possible to determine $h_{\chi s}$ and $r_{\chi s}$. Ideally these parameters should be determined using strain recovery at zero load after rapid loading (Nathal and Ebert, 1985). Since no strain recovery data was available, however, these parameters were determined using the saturation stress for slow strain rates.

*Group 6: Non Schmid factors;* $h_{pe}$*,* $h_{se}$*, and* $h_{cb}$

Since all other parameters from each group have been determined the only remaining parameters are the non-Schmid factors, $h_{pe}$, $h_{se}$, and $h_{cb}$. The calibration of these parameters requires data from material directions other than [0 0 1] or longitudinal. This can be clearly seen since the determination of $h_{pe}$ and $h_{se}$ cannot be simultaneously performed on data in the longitudinal direction since the magnitude of the shear stress on the active octahedral systems is equivalent. Additionally the shear stress on the cubic slip systems is approximately zero causing $h_{cb}$ to have no effect in this orientation. Therefore $h_{cb}$ should be calibrated using transverse data so that the size of the yield surface is correct. $h_{pe}$ and $h_{se}$ should be determined simultaneously using longitudinal and transverse data such that the shift in the hysteresis loop in both directions is correct.

The cubic non-Schmid shear stress, $\tau_{cb}$, is negligibly small in longitudinal loadings and thus $h_{cb}$ can only be calibrated using off-axis data. To calibrate this parameter to DS-CM247LC transverse simulations were compared to experimental data. The parameter $h_{cb}$ affects the threshold stress equally whether the shear stress on the slip system in the slip direction is negative or positive due to the absolute value operation in Eq. (3.7). This causes a symmetric change in threshold stress. Therefore this parameter should be calibrated after $\kappa_0^\alpha(\mathrm{T})$ by taking the data from the transverse direction and matching the difference in tensile yield stress and compressive yield stress. Note that for a single crystal the [1 1 1] direction should be used to calibrate this parameter since the cubic Schmid factors are larger in this orientation than in the [0 1 1] direction. However data from the [0 1 1] direction can be used to calibrate this parameter since it would activate some cubic slip systems.

The parameters $h_{\mathrm{pe}}$ and $h_{\mathrm{se}}$ affect the non-symmetric behavior of the yield stress and therefore the saturation stress. This can be clearly seen by applying a positive or negative stress to the unit cube. The result is that the threshold stress will be offset from its previous value by an amount directly proportional to the shear stress generated by the normal stress as is shown in Figure 3.5. In other words a positive shear on the primary or secondary slip planes in the slip directions will result in an increase in the threshold stress while a negative shear stress will result in a reduction of the threshold stress for positive values of $h_{\mathrm{pe}}$ and $h_{\mathrm{se}}$. Because the relationship between these two shear stresses on these planes will depend upon crystal orientation with respect to loading the coefficients $h_{\mathrm{pe}}$ and $h_{\mathrm{se}}$ should be calibrated such that the offset of the yield or saturation stress is accurate for two different orientations. For the calibration of DS-CM247LC the longitudinal and transverse directions were used to calibrate these two parameters. If data does not exist for multiple directions then these parameters become redundant and one should be set to zero.

## 4.5 Temperature Dependent Parameter Determination

The procedure for determining temperature dependent parameters is to first obtain parameter values at points in temperature from isothermal analyses and then to construct polynomials which follow the parameter behavior with respect to temperature. This may seem like a simple extension of the above procedure but unfortunately it is not. Some of the variability that exists in the model during an isothermal calibration disappears when the temperature dependence is included. Additionally, as the temperature range increases the variability of the model parameters decreases causing calibrations for large temperature ranges to be considerably more difficult than isothermal calibrations. Attempts were made to reduce this variability during the isothermal calibrations but it cannot be eliminated. The challenge comes from needing to find parameter values which nicely fit the behavior of a polynomial where smoothness is crucial. Figure 4.23 shows two sets of parameter values for $\kappa_0$. The polynomial fit in Figure 4.23(a) does not represent how the threshold stress should change with temperature, while the fit in Figure 4.23 (b) does a good job of representing the temperature-dependent behavior of the threshold stress as the maximum is around 750 °C (1023K) and the slope of the polynomial is strongly negative above this temperature.

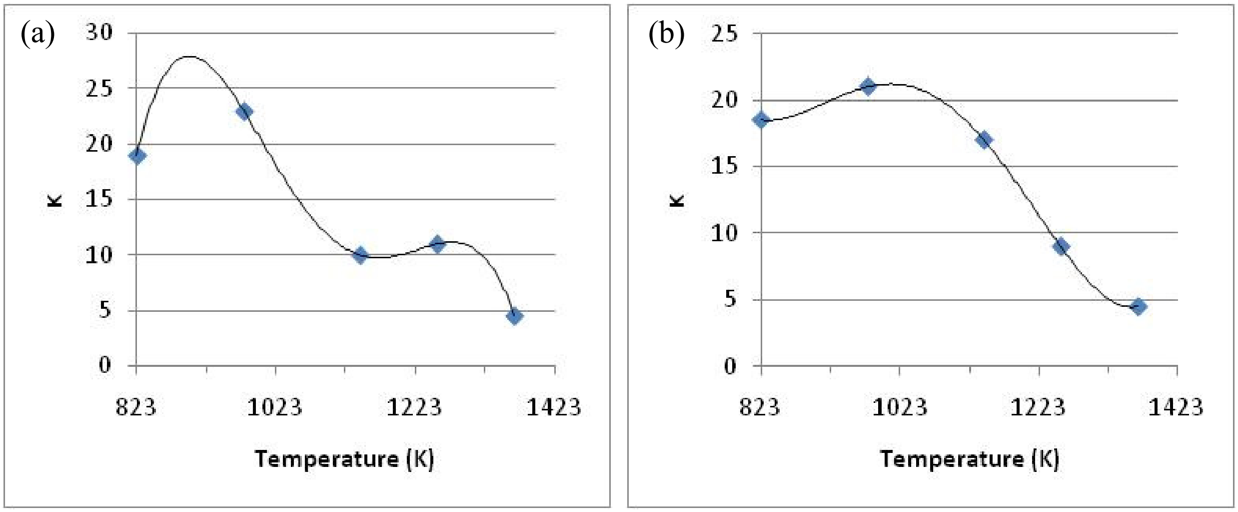

Figure 4.23: Illustration of (a) poor polynomial representation and (b) good polynomial representation to normalized data.

The first step in creating temperature dependent parameters is to calibrate the temperature dependence of the elastic properties. Implementing the temperature dependence of the stiffness constants, however, is fairly simple. One need only to plot the values obtained from isothermal experiments with respect to temperature and apply a 2$^{nd}$ order polynomial to the plot. The result should be very smooth polynomials like the ones shown in Figure 4.24.

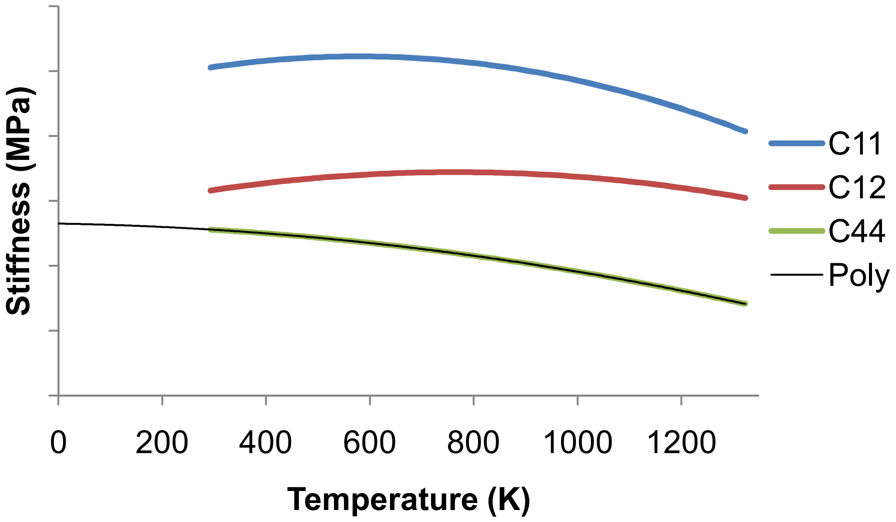

Figure 4.24: Behavior of $C_{11}$ with respect to temperature

The stiffness constants are not as easy to obtain as one might think. Several published values for the stiffness of Ni-base superalloys are shown in Figure 4.25 – Figure 4.27 (Alers et al., 1960; Ledbetter and Reed, 1973; Kuhn and Sockel, 1989; Ichitsubo et al., 2002; Shenoy et al., 2005; Ma et al., 2008). It is generally assumed that the stiffness values for these alloys should not vary significantly from that of pure Nickel (Reed, 2006), however, in reality the stiffness values shown cover a large range . Neither the Young's modulus, shown in Figure 4.28, nor the shear modulus however, show the same variation as do the stiffness constants. This suggests that the methods for determining the stiffness constants may not be as trivial as thought.

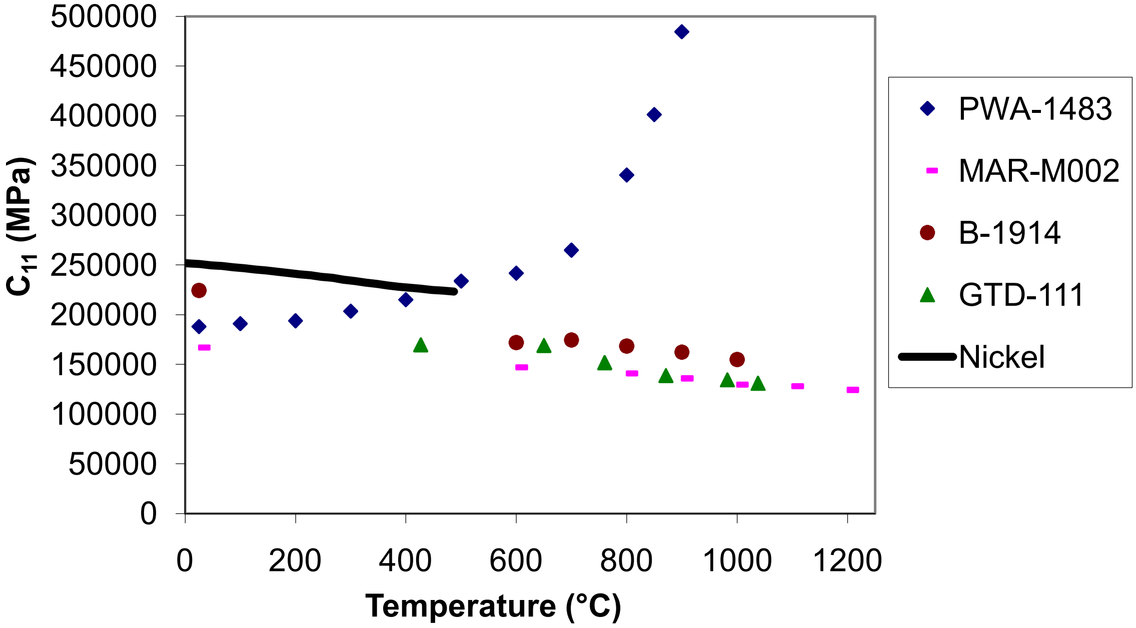

Figure 4.25: $C_{11}$ values from multiple sources

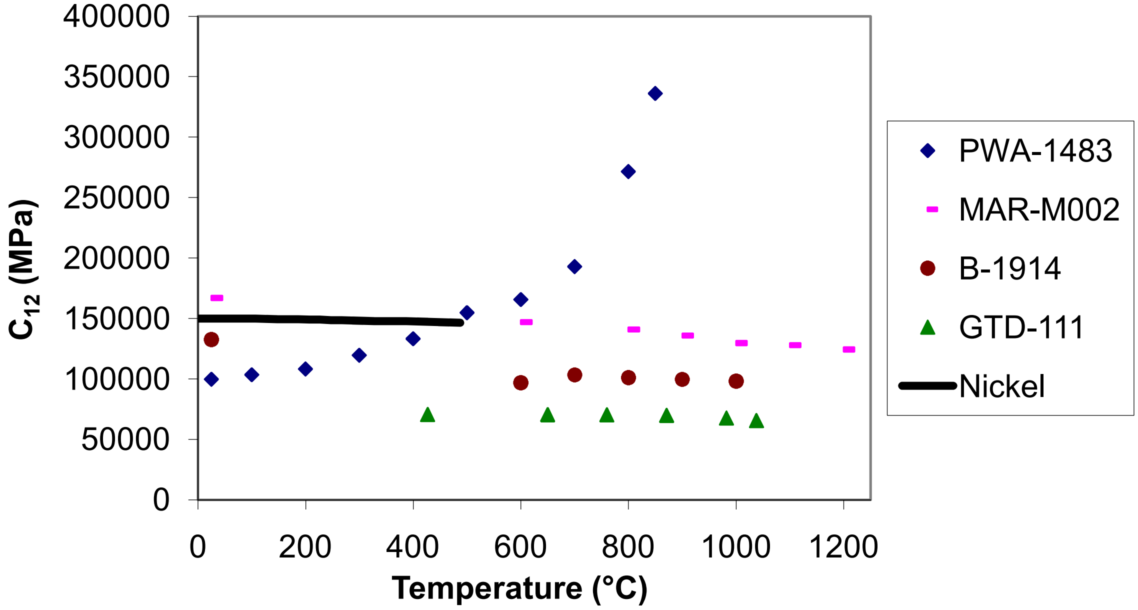

Figure 4.26: $C_{12}$ values from multiple sources

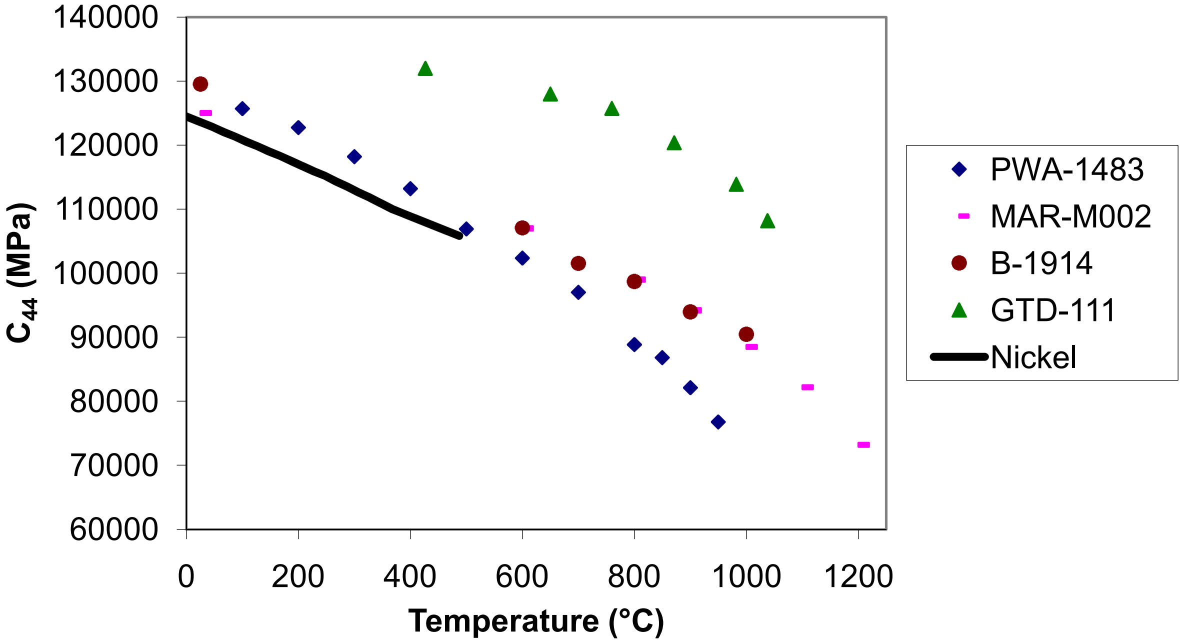

Figure 4.27: $C_{44}$ values from multiple sources

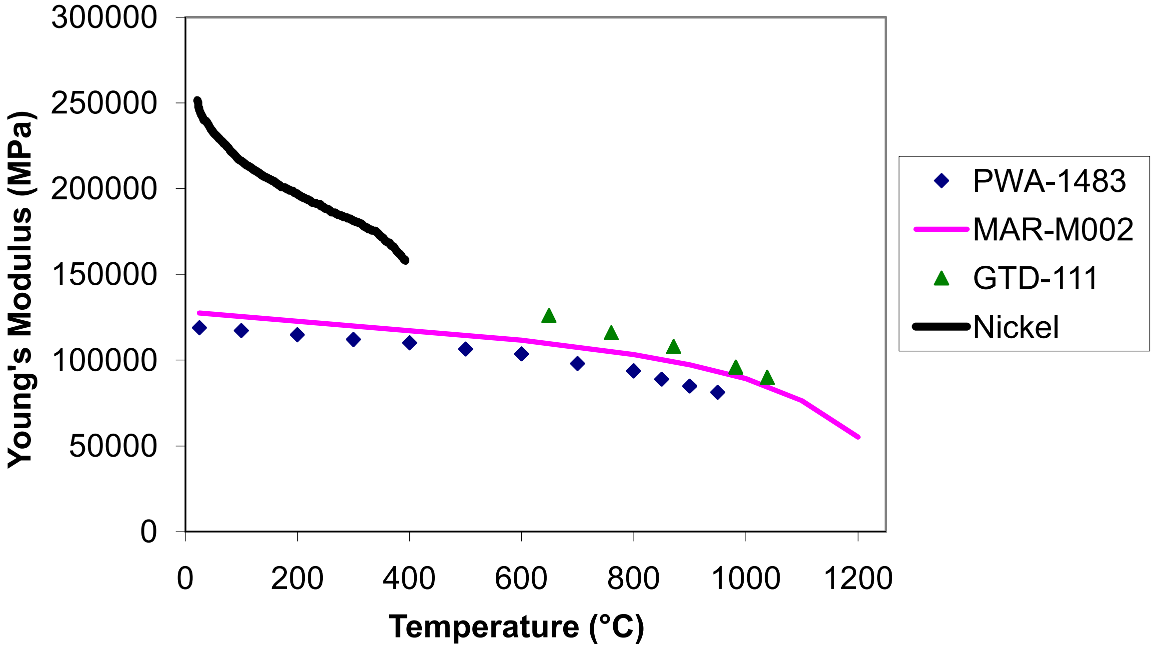

Figure 4.28: Young’s modulus in [0 0 1] direction for a range of DS and SC Ni-base superalloys and Nickel

The CTE is not difficult to obtain once an understanding of its derivation is secured. The implementation of thermal strain in the model follows that proposed by Srikanth and Zabaras (1999), which is slightly more complicated than the traditional approach. The data used to calibrate this parameter is the thermal strains from stabilized temperature cycling. It is tempting to use the thermal strain data from a high temperature isothermal experiment, however this in general is not a reliable measurement of the thermal strain since the temperature across the gage section is not uniform. Since the cyclic stabilization of the thermal strain is necessary prior to TMF experiments, however, it is intelligent to use this data where possible.

The equation by which the thermal deformation gradient is updated is shown in Eq. (3.10). For a finite number of steps the deformation gradient on the nth step can be calculated from the undeformed state as,

$$\begin{aligned}\mathbf{F}_{\mathrm{n}}^{\theta} &= \mathrm{e}^{\beta(\mathrm{T}_{\mathrm{n}})*\Delta\mathrm{T}}\mathrm{e}^{\beta(\mathrm{T}_{\mathrm{n}-1})*\Delta\mathrm{T}} * \ldots * \mathrm{e}^{\beta(\mathrm{T}_1)*\Delta\mathrm{T}_0}\mathbf{F}_0^{\theta} \\ &= \exp\left(\sum_{i=1}^{n} \beta\Delta\mathrm{T}\right)\mathbf{F}_0^{\theta}\end{aligned} \tag{4.36}$$

where $\mathbf{F}_{\mathrm{n}}^{\theta}$ is the thermal deformation gradient on the nth interval and $\mathbf{F}_0^{\theta}$ is the initial thermal deformation gradient for the step. If an infinite number of steps are used then the sum in the exponent can be approximated by an integral which results in,

$$\mathbf{F}_{\mathrm{n}}^{\theta} = \exp\left(\int_{\mathrm{T}_0}^{\mathrm{T}} \beta(x)\mathrm{dx}\right)\mathbf{F}_0^{\theta} \tag{4.37}$$

The thermal strain, $\boldsymbol{\varepsilon}^{\theta}$, can be calculated from the thermal deformation gradient, $\mathbf{F}_{\mathrm{n}}^{\theta}$, by,

$$\boldsymbol{\varepsilon}^{\theta} = \mathbf{N} \cdot \boldsymbol{\epsilon} \cdot \mathbf{N} = \frac{1}{2}\mathbf{N} \cdot \left(\mathbf{F}_{\mathrm{n}}^{\theta^{\mathrm{T}}} \cdot \mathbf{F}_{\mathrm{n}}^{\theta} - \mathbf{I}\right) \cdot \mathbf{N} \tag{4.38}$$

where **N** is a unit vector in the reference configuration, $\boldsymbol{\epsilon}$ is the thermal Green's strain, ${\mathbf{F}_{\mathrm{n}}^{\theta}}^{\mathrm{T}}$ is the transpose of $\mathbf{F}_{\mathrm{n}}^{\theta}$, and **I** is the identity matrix. Eq. (4.37) can be inserted into Eq. (4.38) which results in

$$\boldsymbol{\varepsilon}^{\theta} = \frac{1}{2}\mathbf{N}\cdot\left\{\left[\exp\left(\int_{\mathrm{T_0}}^{\mathrm{T}}\beta(\mathrm{x})\mathrm{dx}\right)\mathbf{F}_0^{\theta}\right]^{\mathrm{T}}\cdot\exp\left(\int_{\mathrm{T_0}}^{\mathrm{T}}\beta(\mathrm{x})\mathrm{dx}\right)\mathbf{F}_0^{\theta}-\mathbf{I}\right\}\cdot\mathbf{N} \tag{4.39}$$

$$= \frac{1}{2}\cdot\exp\left(2\int_{\mathrm{T_0}}^{\mathrm{T}}\beta(\mathrm{x})\mathrm{dx}\right)\mathbf{N}\cdot\left\{\left[\mathbf{F}_0^{\theta}\right]^{\mathrm{T}}\cdot\mathbf{F}_0^{\theta}-\mathbf{I}\right\}\cdot\mathbf{N} \tag{4.40}$$

$$= \frac{1}{2}\left(\exp\left(2\int_{\mathrm{T_0}}^{\mathrm{T}}\beta(\mathrm{x})\mathrm{dx}\right)-1\right) \tag{4.41}$$

Taking the natural log of both sides and rearranging gives,

$$\frac{\ln\left(2\varepsilon^{\theta}+1\right)}{2} = \int_{\mathrm{T_0}}^{\mathrm{T}}\beta(\mathrm{x})\mathrm{dx} \tag{4.42}$$

Taking the partial derivative of this with respect to temperature results in,

$$\beta(T) = \frac{\partial\ln(2\varepsilon_{\mathrm{th}}+1)}{2\cdot\partial\mathrm{T}} = \frac{\partial a}{\partial\mathrm{T}} \tag{4.43}$$

where *a* is the function $\ln(2\varepsilon_{\mathrm{th}}-1)/2$. By plotting *a* with respect to temperature, as is shown in Figure 4.29, a 4th order polynomial can be fit to the result. The CTE, *β*, is then the partial derivative of the polynomial with respect to temperature, which is shown in Figure 4.30. Table 4.6 shows the relationship between the CTE and the polynomial coefficients where $a_i$ is the coefficient of the ith term in the polynomial. The values for the CTE from Figure 4.29 are shown in Table 4.6 as additional illustration of the process for finding them.

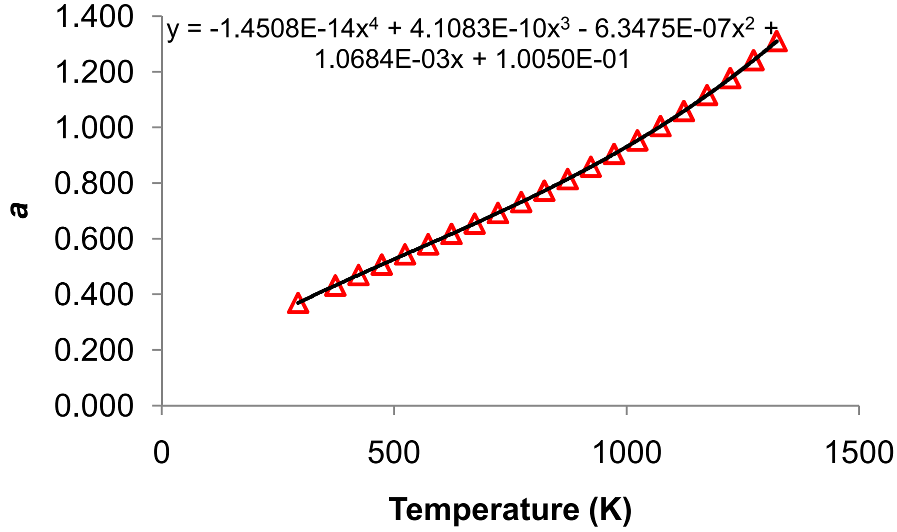

Figure 4.29: Plot of *a* vs. T

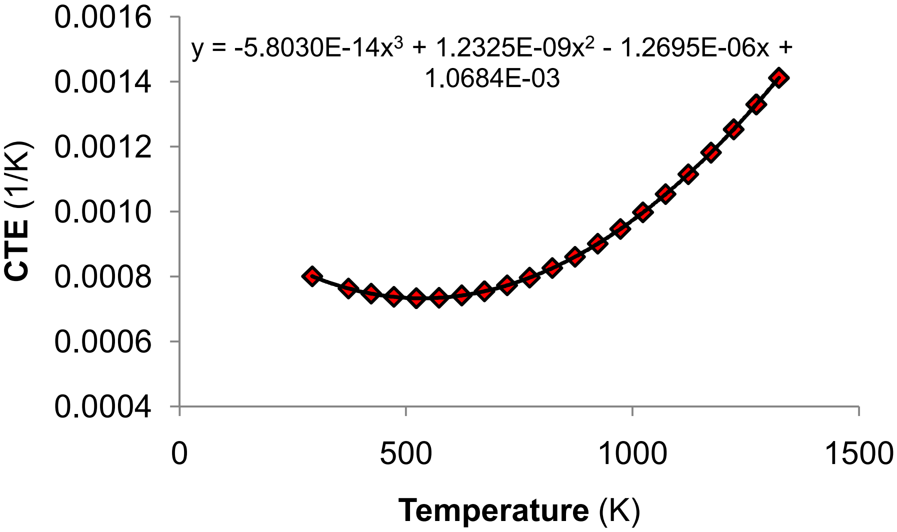

Figure 4.30: Polynomial for $\beta$

Table 4.6: Relationship between calculated and model parameters

| Model Parameter | Polynomial Coeffs. | Value from Figure 4.29 |
|---|---|---|
| ec1 = | $4*a_1$ | $-5.803\text{x}10^{-14}$ |
| ec2 = | $3*a_2$ | $1.233\text{x}10^{-9}$ |
| ec3 = | $2*a_3$ | $-1.270\text{x}10^{-6}$ |
| ec4 = | $1*a_4$ | $1.068\text{x}10^{-3}$ |

One of the most challenging temperature dependent parameters to calibrate is the threshold stress. Since the yield stress of Ni-base superalloys increases up to around 750 °C the threshold stress should follow the trend that it increases up to about this point. Afterwards, however, it quickly drops off. This behavior is difficult to match with a single polynomial which maintains smoothness across the entire temperature range and so it has been found necessary to describe this parameter with two separate temperature dependent polynomials. The temperature at which the model transitions from one polynomial to the other has been included as an input parameter as shown in Table 4.2. At the transition temperature both polynomials should have the same value and approximately the same slopes. In order to obtain smoothness a trade-off between $\kappa_0$ and $R_\chi$ must sometimes be employed where the yield stress is traded with the steady state value of the back stress such that the saturation stress remains the same.

$$R_\chi^{\mathrm{i}+1} = R_\chi^{\mathrm{i}} - \frac{\mu_0}{\mu}(\kappa_0^{\mathrm{i}} - \kappa_0^{\mathrm{i}+1}) \tag{4.44}$$

Here *i* represents the calibrated result, *i+1* represents the new parameters, $\mu$ is the shear modulus in MPa at the current temperature, and $\mu_0$ is the shear modulus at 0K. The result of these transformations is the plot on the right of Figure 4.23 which produces a smooth polynomial. Note the slope of the polynomial on the right as it approaches 550 °C is approximately zero. This is done since the plasticity parameters are assumed constant below 550 °C in this parameterization, which will be validated in a later chapter.

Previously $\dot{\gamma}_0$ was determined for each isothermal temperature. However obtaining a single value for this parameter as well as for $Q_0$ requires experimental data from multiple temperatures. To determine both $\dot{\gamma}_0$ and $Q_0$ they should be thought of as a single temperature dependent function.

$$\Phi(\mathrm{T}) = \dot{\gamma}_0\theta(\mathrm{T}) = \dot{\gamma}_0 \times \begin{cases} \exp\left(-\frac{Q_0}{\mathrm{RT}}\right) \ldots\ldots\ldots\ldots\ldots\ldots\ldots\ldots\ldots\ldots\ldots \mathrm{T} \geq \frac{\mathrm{T_m}}{2} \\ \exp\left(-\frac{2Q_0}{\mathrm{RT_m}}\left[\ln\left(\frac{\mathrm{T_m}}{2\mathrm{T}}\right)+1\right]\right) \ldots.\ldots\ldots \mathrm{T} \leq \frac{\mathrm{T_m}}{2} \end{cases} \tag{4.45}$$

As can be seen $Q_0$ controls the temperature dependence. To calibrate $Q_0$, the flow rule at the highest temperature should first be correctly calibrated using $\dot{\gamma}_0$ as is shown in Figure 4.31. The dashed lines are the flow rule, and the isolated symbols are the saturation stresses of experiments. It is observed that in this figure the dislocation activation energy is obviously much too small to capture the temperature dependence of the rate dependence. Therefore the value of $Q_0$ is increased until the isothermal lines at each temperature match the experimental data as shown in Figure 4.32. To accomplish this $\dot{\gamma}_0$ must be simultaneously modified by

$$\dot{\gamma}_0^{\mathrm{i}+1} = \dot{\gamma}_0^{\mathrm{i}}\exp\left(\frac{Q_0^{\mathrm{i}+1} - Q_0^{\mathrm{i}}}{\Phi}\right) \tag{4.46}$$

where “i+1” are the new parameter values and “i” is the value used in Figure 4.31. Φ is the temperature dependent function which changes at half the melting temperature as in Eq. (4.45). Note that the activation energy of NASAIR 100 (Nathal and Ebert, 1985) which is an alloy modified from MAR-M247 for single crystal applications, was used as an initial value in the calibration of DS-CM247LC.

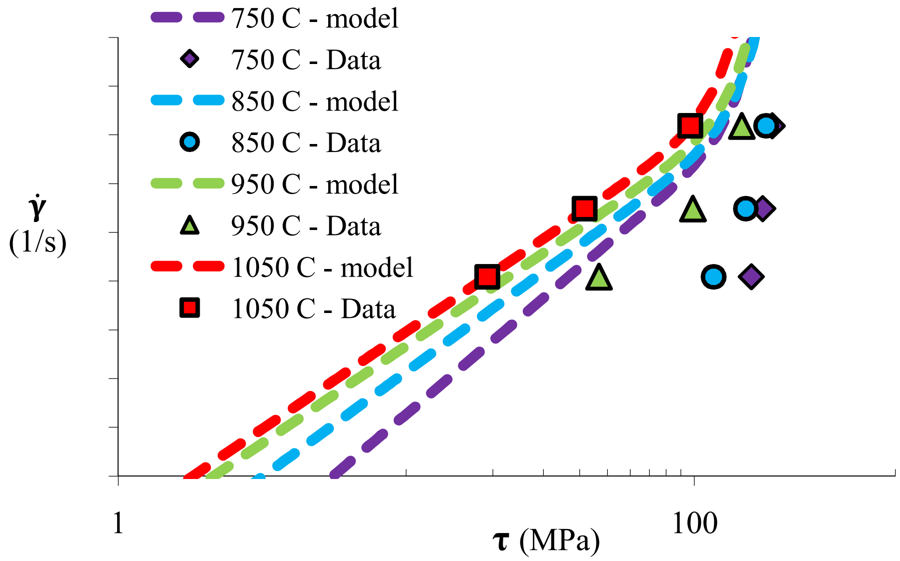

Figure 4.31: Model calibrated at highest temperature using $\dot{\gamma}_0$

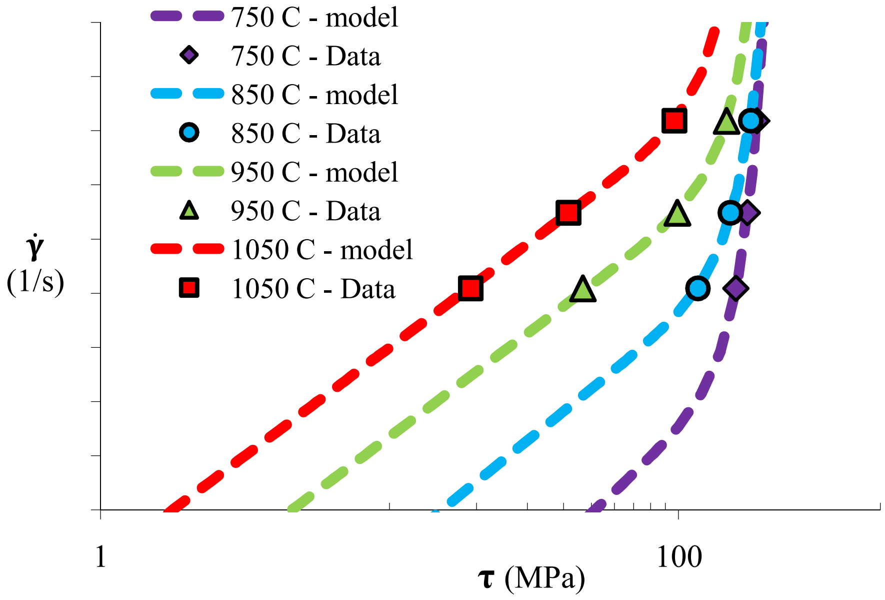

Figure 4.32: Model calibration after adjusting $Q_0$ and mathematically correcting $\dot{\gamma}_0$

As noted above, finding temperature dependent parameters can be difficult. It should be anticipated that the initial isothermal parameters will not create an adequate temperature dependent behavior. Therefore an iterative approach should be used where isothermal parameterizations are continuously performed in tandem with polynomial creation as shown in Figure 4.3.

## 4.6 Discussion of Parameter Optimization

In the course of determining parameters for the CVP model, one must realize that there exists no unique solution that completely captures a material's behavior. This is a consequence of the phenomenological nature of the model. Thus when a parameter set has been determined from the above procedures, one must ask if there could be a separate set of parameters which more accurately capture the material behavior. To answer this question an optimization algorithm could be used to find optimal parameters based upon an evaluation criteria similar to what Song (2010)  has done. This should not, however, be viewed as a shortcut to material parameters since the initial parameter set has a significant effect on the outcome of the optimization. Hence, one cannot skip the parameterization phase and go directly to solving an optimization problem. Any robust automated procedure must take small steps to hone in on a set of parameters.

In this work the author attempted to use ModelCenter® (Phoenix Integration v9.0) to find optimal parameters for DS-CM247LC. However, because the initial parameter values were not sufficiently accurate and because the error evaluation techniques were not adequately sophisticated, the time for convergence was on the order of days for a single parameter when the same accuracy could be achieved by hand in minutes. Due to time constraints the author was not able to focus on reducing the time of convergence. However, based upon this experience a set of requirements is outlined below.

The setup of an isothermal optimization should follow the procedure described in this chapter for isothermal parameterizations. A series of individual optimizations should be constructed within an optimization such that the parameter groups are determined individually as is shown in Figure 4.33. This method is similar to that shown in Song (2010) except that the levels of optimization have been sequenced rather than looped. There are two levels in the process. Level 1 is where the parameter groups are optimized, and level 2 is where the parameters are optimized.

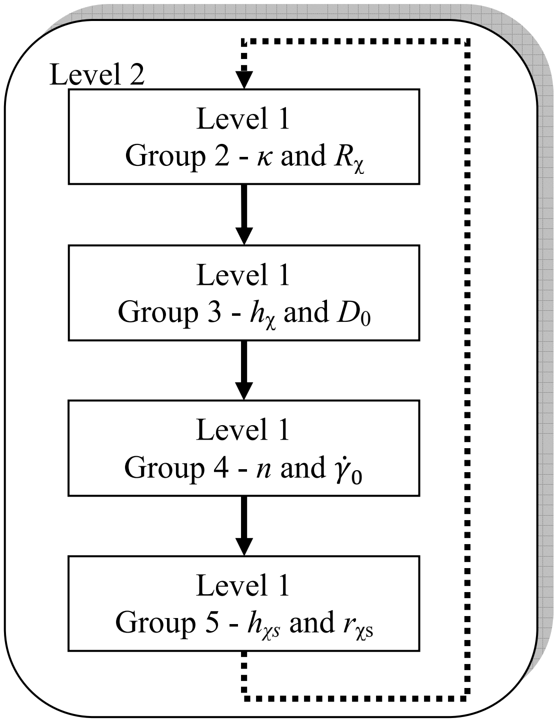

Figure 4.33: Isothermal optimization of parameters

To evaluate the error between the model predictions and experiments there must be a consistent way of determining the differences between the two. There are several possibilities for strain controlled experiments;

1) Take the difference between values of stress at discrete points in strain.

2) Take the difference between values of strain at discrete points in stress.

3) Take the difference between values of stress at discrete points in time.

4) Take the difference between values of strain at discrete points in time.

5) Take the difference between values of inelastic strain at discrete points in time.

Of those listed the two best are 1) and 3) since taking the difference between values of stress gives an appreciable error even for small deviations. The second option is acceptable for stress controlled experiments, however since the model is run by inputting a strain value, this criterion is difficult if not impossible to implement because the controlled strain must be adjusted to achieve convergence. The fourth option does not yield acceptable results for strain controlled experiments because it would result in the evaluation of the exactness of the experimental controller. The fifth option is an acceptable criterion for creep holds and strain holds if there is an accurate measurement of the inelastic strain. However this measurement is hard to achieve without significant noise cluttering the signal and making errors difficult to reduce. Regardless of which criterion is used, it will need to find identical x-values for comparing y-values. This can easily be accomplished through interpolation of the experimental data to find y-axis values for points of x-axis values which were used in the model prediction. This is shown graphically in Figure 4.34 where the experimental data has been interpolated to match the strain values for the model prediction.

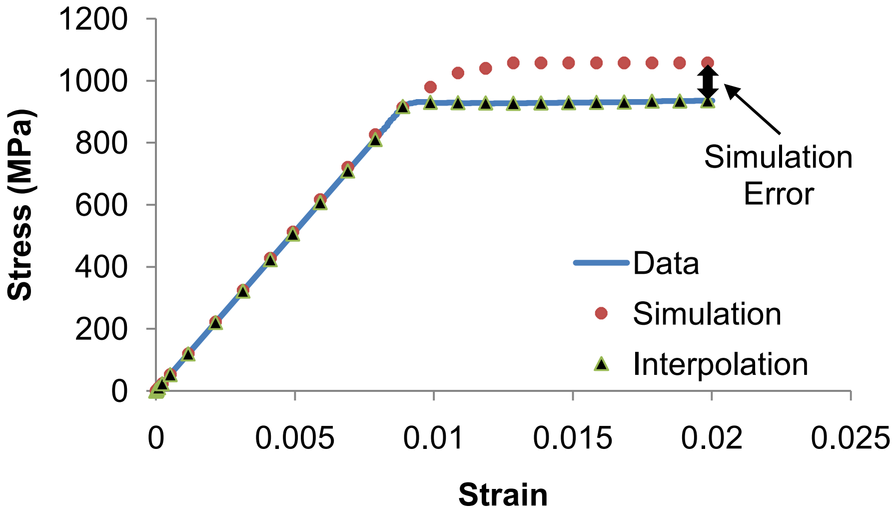

Figure 4.34: Interpolation of strain and stress for comparison with the CVP model

Two different error definitions have been chosen from the proposed five listed above. Definition 1) is chosen for most of the error evaluations because it allows the evaluation of the model parameters based upon the same criterion which fatigue lives are calculated: stress and strain. However this criterion cannot be used for stress relaxation where there exists a single value of strain, or small range of strain, with multiple values of stress. In these cases the third criterion, where the difference between values of stress at discrete points in time is taken, is used.

Once a criterion has been selected for error evaluation the error can be calculated between the experimental and model response through an objective function. One good choice for an objective function is,

$$Error = \frac{1}{N}\sum_{i=1}^{N} w(\varepsilon_\mathrm{i})\left(\frac{\sigma_{\mathrm{exp}}(\varepsilon_\mathrm{i}) - \sigma_{\mathrm{sim}}(\varepsilon_\mathrm{i})}{\left(\sigma_{\mathrm{exp}}\right)_{\mathrm{max}}} \times 100\right)^2 \tag{4.47}$$

where $N$ is the total number of data points used for comparison, $w(\varepsilon_\mathrm{i})$ is the weighting that has been assigned to the data, $\sigma_{\mathrm{exp}}$ is the experimental stress, and $\sigma_{\mathrm{sim}}$ is the simulation stress

(DeMarco et al., 2010). It uses the sum of the squares method, includes a weighting for emphasis of importance, and it normalizes the stress so that values of different magnitudes may be compared. This last benefit is important in the evaluation of the error between the model response and experiments because a wide range of stress magnitudes are seen when the strain rate and temperature dependencies are considered. Accurate optimization of creep parameters, for example, will not be achieved quickly if the error is evaluated identically to that of the hardening parameters without normalization.

The weighting can be assigned in multiple ways. One way is to assign weighting based upon how important the data is. With this method certain aspects of the data can be accurately parameterized while leaving others more roughly calibrated. Another way to assign the weighting is by how sensitive the model is to a certain parameter. With this technique the weighting can be increased for those parameters which only cause small changes in the model with large changes in their value, such as $\dot{\gamma}_0$. This would cause the optimization to work harder on the less sensitive parameters. The weighting can also be used to single out a parameter for optimization if its interdependencies can be neglected. This can be done by setting the weight to all other error evaluations, except the one most sensitive to a single parameter, to zero.

# Chapter 5. Experimental Protocols for Efficient Calibration

The design of experiments is important not only in the calibration of the CVP model, but also in reducing the time and effort of calibration. Typical testing regimens can consume upwards of six months since separate experiments are run for each set of control conditions, such as temperature, strain rate, and initial microstructure. Additionally the hysteresis response of low cycle fatigue test data of Ni-base superalloys often does not contain the significant cyclic plastic strain needed to calibrate the CVP model. Therefore it is necessary to set forth a list of requirements which when placed on the collection techniques of experimental data result in a dataset adequately detailed for the efficient calibration of the CVP model for use in thermomechanical fatigue predictions. In this chapter a list of the minimum requirements is defined and the experiments that were selected to fulfill these requirements and used in this study are provided. These do not in general fulfill the requirements for calibration of the model for use in thermal processing or high rate deformation.

## 5.1 Minimum Data Requirements

There exists a minimum amount of data that is required to accurately calibrate the crystal viscoplasticity model to a specific material which depends on the specific material traits desired for calibration. Table 5.1 shows a summary of the requirements for an accurate, complete, temperature-dependent parameterization of the CVP model. The following is a discussion of what motivates each requirement.

Table 5.1: Requirements for calibration data

| **Requirement** | **Reason** |
|---|---|
| Elastic modulus in at least two directions | Calibration of the stiffness constants, $C_{11}$, $C_{12}$, $C_{44}$ |
| Thermal strain vs. temperature data | Calibration of the CTE |
| Multiple material directions | Calibration of octahedral and cubic slip parameters |
| Cyclic response | Bauchinger effect, asymmetry of the yield surface |
| Minimum of three strain rates | Calibration of the strain rate dependent parameters |
| Large plastic strain range: ~0.4% | Proper calibration of internal state variable evolution |
| Stabilized hysteresis | Evolution of internal state variables |
| Minimum of six temperatures | Temperature-dependent polynomial creation |

The first requirement is the most obvious. The elastic constants need to be determined from data. This is exceedingly important for thermomechanical loading since small errors in the elastic response can lead to large errors in the cyclic plastic strain prediction, particularly when the amount of applied plastic strain is small in comparison to elastic strains. Even a small deviation in the elastic modulus can cause a large error in the model response as seen in Figure 4.4. Therefore, for each isothermal testing temperature a separate test or a section of a test should be devoted to determining the elastic modulus and Poisson's ratio. It is noted here that the elastic modulus in the transverse direction can vary as much as 30% for DS alloys (Siemens, 2010). This variation is caused by the grain size in the transverse direction; if the extensometer is placed across a large grain the measurement of strain can be significantly biased.

The second requirement is that the coefficient of thermal expansion be determined accurately. The process for determining the value of the CTE is listed in section 4.5 and requires stabilized cyclic data of thermal strain versus temperature. Because the stabilized cycling of temperature is required for TMF experiments the data is most conveniently recorded from free expansion thermal cycling before the start of a TMF experiment, after steady state thermal cycling conditions have been achieved.  Note that, as mentioned in Chapter 4, the half temperature cycle created by raising an elevated temperature experiment from room temperature to its testing temperature is not sufficiently accurate for the calibration of the CTE and should not be used unless the temperature change rate is slow enough to ensure uniform temperature distribution throughout the gage section.

The third requirement is that the material be tested in several different material directions. Since the loading of a component is in general not aligned with the [0 0 1] direction it is important to determine the stress-strain response of the material in several directions and to calibrate the model to them. This allows the activity of different slip systems to be determined along with the directional dependence of the elastic constants. Suggested testing directions are shown in Table 5.2, Table 5.3, and Table 5.4 for different alloy crystal structures.

Table 5.2: Single Crystal required orientations

| **Single Crystal** | |
|---|---|
| **Direction** | **Reason** |
| [0 0 1] | 12 octahedral slip systems active |
| [0 1 1] | 4 octahedral slip systems active, 6 cubic slip systems mildly active |
| [1 1 1] | 6 octahedral and 3 cubic slip systems active |
| [1 2 3] | Single slip system active |

Table 5.3: Directionally-Solidified required orientations

| Directionally Solidified | |
|---|---|
| **Direction** | **Reason** |
| L | Only octahedral slip systems active |
| T | Both octahedral and cubic slip systems active |
| 45° | Both octahedral and cubic slip systems active |

Table 5.4: Polycrystalline required orientations

| Polycrystalline | |
|---|---|
| **Direction** | **Reason** |
| any | Response is averaged in all directions |

The next requirement is that the data include the cyclic response. This is important for selection of the hardening parameters (Huber and Tsakmakis, 2001): the Bauschinger effect as well as the evolution of back stress and threshold stress are contained in this data. Additionally the stabilized cyclic response is needed for selection of material parameters which are relevant to fatigue life predictions. Included in the cyclic response should be a significant amount of plasticity so that the inelastic parameters can be clearly identified.

Since as mentioned previously a materials deformation response is time dependent, multiple strain rates or dwells must be included in the data acquisition. Looking at the flow rule, there are three regions of interest: slow strain rates, medium strain rates, and fast strain rates. Since the material response is strain rate insensitive at very high strain rates only one strain rate is required to determine the material response in this region. However, at least two strain rates are needed to determine the slope of the flow rule at slower strain rates. Thus three strain rates is the minimum number required to determine the strain rate dependence of a Ni-base superalloy. As can be seen in Figure 3.1 a large change in strain rate is needed to affect a relatively small change in shear stress. Thus each of the chosen strain rates should be at least an order of magnitude different from each other.

As mentioned above a significant amount of plasticity is required to calibrate the plasticity parameters $\chi$, $D_0$, $\dot{\gamma}_0$, $Q_0$, and $B_0$. Typically low cycle fatigue tests for fatigue life prediction contain inelastic strain ranges less than 0.2%, however this data does not contain significant amounts of information about the evolution of the state variables. Therefore a minimum plastic strain range of 0.4% is suggested for the efficient and accurate calibration of the state variables. This suggestion is based upon the strain hardening of DS-CM247LC. If no strain hardening is observed in a material, then the inelastic strain range can and should be reduced. The important aspect of this requirement is to include enough plasticity so that the internal state variables reach a saturation value. However, care must be taken to not include too much plasticity since this will cause premature failure in the experiment. This is discussed in the next requirement. Additionally, the yield surface must be crossed at a minimum of six points so that there is a sufficient number of data points for the creation of the temperature dependent polynomials fitted through $h_\chi(\mathrm{T})$, $R_\chi(\mathrm{T})$, $\kappa_0(\mathrm{T})$. If the temperature range of interest is small (O(200 °C)) fewer data points can be used since the order of the polynomials can be reduced.

Finally, a stabilized hysteresis is needed for each strain rate at each temperature. This is important since the steady state material response is needed to determine the evolution of the state variables. Thus a stabilized hysteresis loop is needed in order for the model to reasonably be expected to accurately describe the material response. Depending on the intended application of the model, the transient response may or may not be of interest. If the focus is developing modeling tools for life prediction, modeling the stabilized response is often sufficient. The variables dealing mostly with the transient behavior can then be turned off which simplifies the model. If it is desirable to determine the transient response, which might be needed for thermomechanical processing simulations where the initial deformation response is important, then several cycles prior to stabilization are needed. This could add significant amounts of time to the parameterization process since the simulations must be several times longer than for the stabilized response and the number of parameters considered increases. Because the suggested amount of plasticity causes the life of the specimen to be low, typically less than 50 cycles, care must be taken in designing the test plan such that a sufficient number of cycles is included to capture the material behavior. While a stabilized hysteresis loop is required it may be impossible to obtain at each strain rate if the life of the specimen is exceeded by the number of cycles needed to obtain the steady state response. If this is the case there are several options. The first is to split strain rates into different tests. This should reduce the required number of cycles per test to be under the expected life. The second option is to reduce the inelastic strain range which would cause the life of the specimen to increase. This is an option only if the steady state response of the state variables can be inferred from the data. For instance, a stabilized hysteresis is never reached in Figure 5.1 for the medium or fast strain rates yet because the stress-strain relationship is strain rate insensitive at low temperatures the steady state response can be inferred from the slow strain rate.

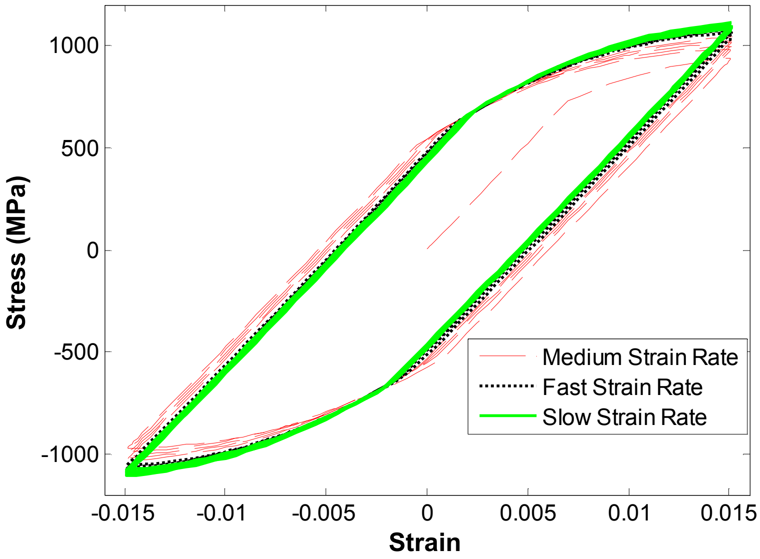

Figure 5.1: Example of stress-strain relationship at low temperature which does not reach cyclically stabilized hysteresis

## 5.2 Experiments

A set of experiments was designed to fulfill the above requirements. Experiments were separated by temperature and one isothermal experiment was conducted at each temperature. Figure 5.2 shows the strain history that was designed to fulfill the above requirements. Each isothermal experiment contains three strain rates for calibration of the flow rule in both the rate dependent and insensitive regions. Additionally a compressive creep hold is included in each experiment. The strain rates are organized such that the creep hold follows the fastest strain rate and is then followed by the slowest strain rate. This causes the amount of creep to be more significant than if placed anywhere else in the experiment. Five cycles are completed at both of the faster strain rates to allow the material to achieve cyclic hysteresis. The total time of each of the isothermal experiments is shorter than 4.5 hours.

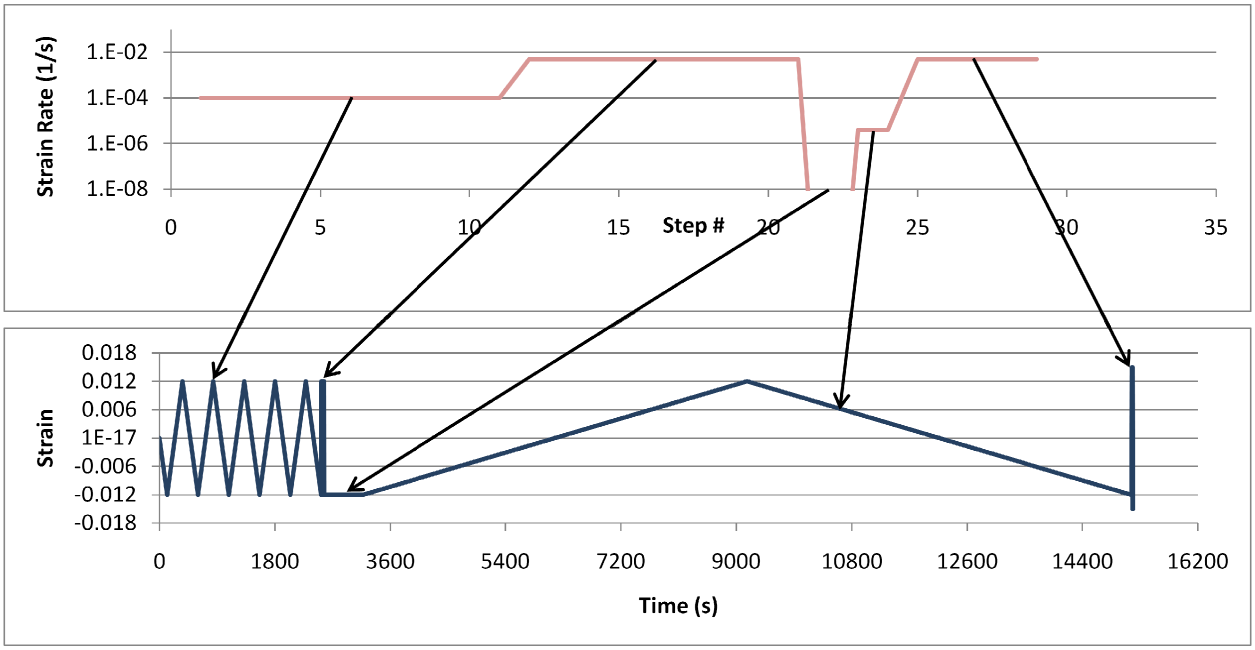

Figure 5.2: Strain history designed for calibration experiments

Table 5.5 shows the test plan for the longitudinal direction. The strain ranges were selected to produce the required inelastic strain range, and the temperatures were selected to produce adequate points for polynomial creation.

Table 5.5: Isothermal longitudinal test plan

| Test # | Control | Wave | Orientation | Hold Time (s) | Min Strain Rate (1/s) | Max Strain Rate (1/s) | Strain Range % | R | Temp (°C) |
|---|---|---|---|---|---|---|---|---|---|
| 1 | Strain | Ramp | L | none | 4.0E-06 | 5.0E-03 | 2 | -1 | 23 |
| 2 | Strain | Ramp | L | none | 4.0E-06 | 5.0E-03 | 2.4 | -1 | 650 |
| 3 | Strain | Ramp | L | none | 4.0E-06 | 5.0E-03 | 2 | -1 | 750 |
| 4 | Strain | Ramp | L | none | 4.0E-06 | 5.0E-03 | 2 | -1 | 850 |
| 5 | Strain | Ramp | L | none | 4.0E-06 | 5.0E-03 | 2 | -1 | 950 |
| 6 | Strain | Ramp | L | none | 4.0E-06 | 5.0E-03 | 2 | -1 | 1050 |

Table 5.6 and Table 5.7 show the test plan for non-Longitudinal isothermal testing and TMF testing respectively. The strain ranges for the transverse and off-axis test were adjusted with the knowledge that the modulus will be different from the longitudinal direction. Only three tests were performed in each of these directions since the parameters that become active in these directions are assumed to be non temperature-dependent. Additionally cube slip is active at higher temperatures (Bettge and Osterle, 1999), so the experiments used for calibration were the ones at 950 °C. The strain ranges for the TMF tests were determined from previous experiments (Kupkovits, 2009).

Table 5.6: Off-axis testing matrix

| Test # | Control | Wave | Orientation | Hold Time (s) | Min Strain Rate (1/s) | Max Strain Rate (1/s) | Strain Range % | R | Temp (°C) |
|---|---|---|---|---|---|---|---|---|---|
| 1 | Strain | Ramp | T | none | 1.0E-04 | 1.0E-03 | 1.4 | -1 | 400 |
| 2 | Strain | Ramp | T | 2000 | 1.0E-04 | 1.0E-03 | 1.6 | -1 | 750 |
| 3 | Strain | Ramp | T | 2000 | 1.0E-04 | 1.0E-03 | 1.4 | -1 | 950 |
| 4 | Strain | Ramp | 45° | none | 1.0E-04 | 1.0E-03 | 1.4 | -1 | 400 |
| 5 | Strain | Ramp | 45° | 2000 | 1.0E-04 | 1.0E-03 | 1.6 | -1 | 750 |
| 6 | Strain | Ramp | 45° | 2000 | 1.0E-04 | 1.0E-03 | 1.4 | -1 | 950 |

Table 5.7: TMF test matrix

| Test # | Control | Wave | Orientation | Hold times (s) | Min Strain Rate (%/s) | Max Strain Rate (%/s) | Mechanical Strain Range (%) | R | Min Temp (°C) | Max Temp (°C) |
|---|---|---|---|---|---|---|---|---|---|---|
| 1 | Strain | Ramp | L | none | 1.8E-03 | | 1.4 | -1 | 100 | 950 |
| 3 | Strain | Ramp | L | 600 | 1.0E-03 | 5.0E-03 | 1.4 | -1 | 100 | 950 |

# Chapter 6. Experimental Methods

The experiments listed in the previous chapter were performed on DS-CM247LC and used to calibrate the CVP model shown in Table 3.1. The following presents the experimental setup used and the data that was acquired.

## 6.1 Experimental Setup

The experiments listed in Table 5.5, Table 5.6, and Table 5.7 were conducted on DS-CM247LC. The total time required to run each of the experiments was 22 days spread over five months with each isothermal experiment lasting approximately four hours and TMF experiments lasting between one and five days. Strain rates of $5.0 \times 10^{-3}$/s, $1.0 \times 10^{-4}$/s, and $4.0 \times 10^{-6}$/s were used for the fast, medium, and slow strain rates, respectively. These strain rates were chosen based upon data from DS-GTD-111 (Shenoy, 2006) and from data on DS-CM247LC (Kupkovits, 2009).

A dog bone specimen with the dimensions shown in Figure 6.1 was used for all experiments, where the units are in inches. The experimental set up for all experiments was as follows; a 44.5 *kN* (10 kip) axial servo-hydraulic MTS® testing machine with water cooled grips (MTS® model 646) was used along with TestStar controller software (Testware SX® 4.0D). The load cell resolution of the machine was ±0.22 *kN*. Temperature feedback was provided by two 26-gage K-type thermocouples having 0.404 mm (0.159 in) diameter leads which were spot welded just above and below the specimen gage section as is shown in Figure 6.2. The specimen was heated by an Ameritherm® single phase 2 *kW* radio frequency induction heater with a control resolution of ±1 °C which was controlled by a PID controller (Watlow® model 945A-2FK5-A000) with closed-loop feedback control. A high temperature extensometer (MTS® model 632.52E-14) with 5.0 *mm* diameter alumina extension rods and a 1.0" gage length was used to obtain strain measurements. For the thermomechanical experiments the controller PID values were determined for each test such that the error between the desired temperature and actual temperature was within the ASTM specification E8/E 8M-08 (ASTM, 2008). Data acquisition rates were determined such that there was a minimum of two hundred data points per half cycle.

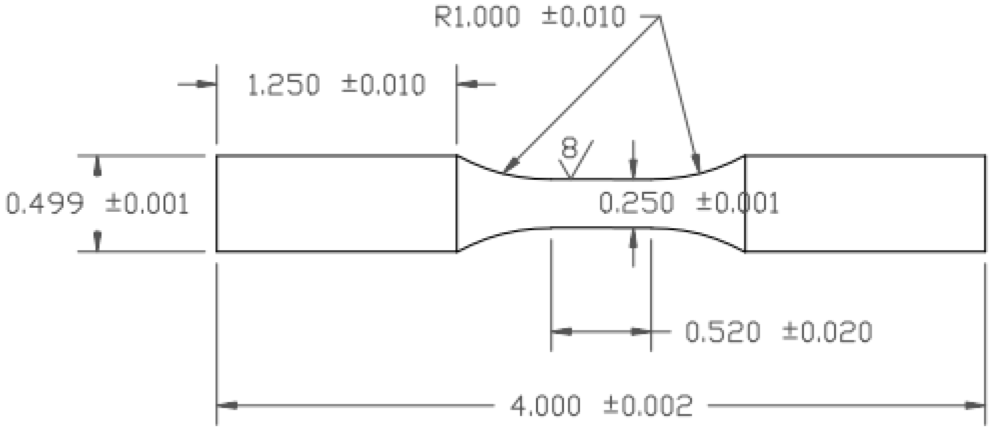

Figure 6.1: Specimen drawing and dimension specification

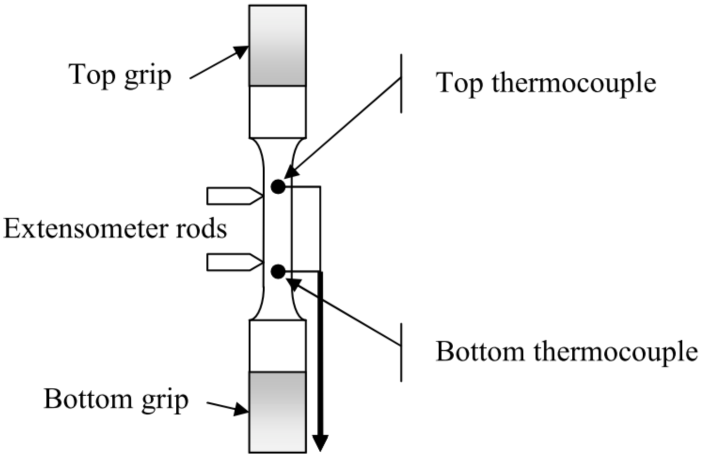

Figure 6.2: Diagram of inserted specimen

## 6.2 Experimental Data

Figure 6.3 - Figure 6.12 show the experimental data obtained from the longitudinal and transverse calibration experiments listed in Table 5.5 and Table 5.6, respectively. The plots show the data separated by temperature so that the strain rate dependence is emphasized. Each cycle is shown in the figures so that the cyclic hysteresis is evident. This data was used in model calibration. By comparing Figure 6.3 to Figure 6.4 it can be seen that the stabilized cyclic response does not differ significantly between these two temperatures with the exception that the elastic modulus is different. This was used to simplify the temperature-dependent parameters by keeping them constant between these two temperatures. The experiment at 750 °C is the first to experience quantifiable strain rate sensitivity as can be seen in Figure 6.5. The higher temperature experiments reach a stabilized cyclic hysteresis at each strain rate much faster than the lower temperature experiments. Experiments which do not complete the slowest cycle, seen in Figure 6.3and Figure 6.7 were stopped due to adverse changes in the experimental

environment. However, these experiments were not re-run since the data contained in them was sufficient for calibration purposes.

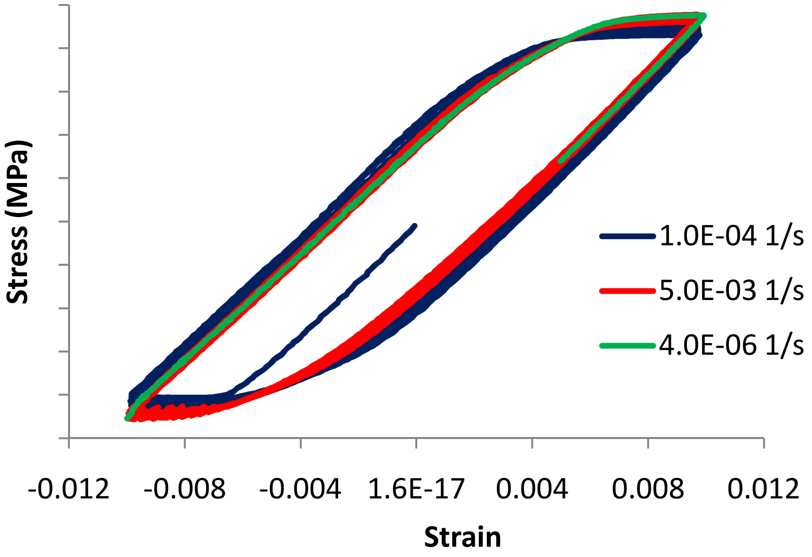

Figure 6.3: Calibration experiment response in the longitudinal direction at room temperature

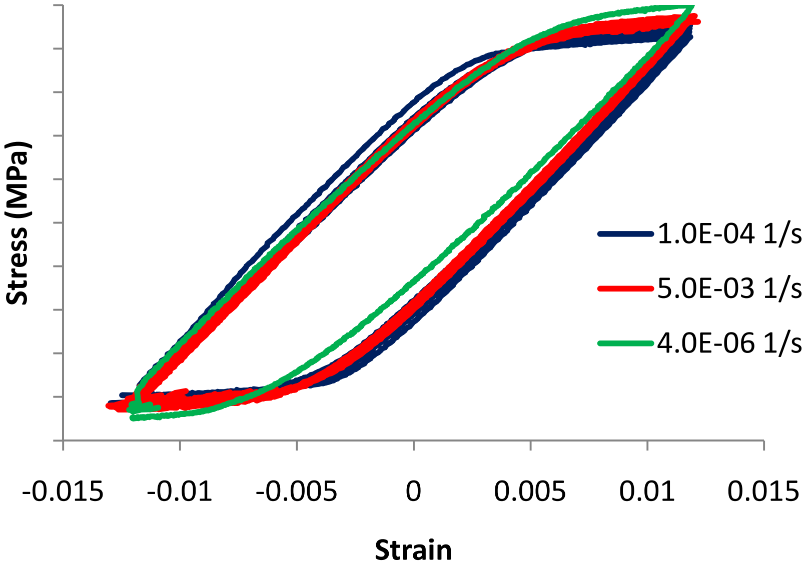

Figure 6.4: Calibration experiment response in the longitudinal direction at 650 °C

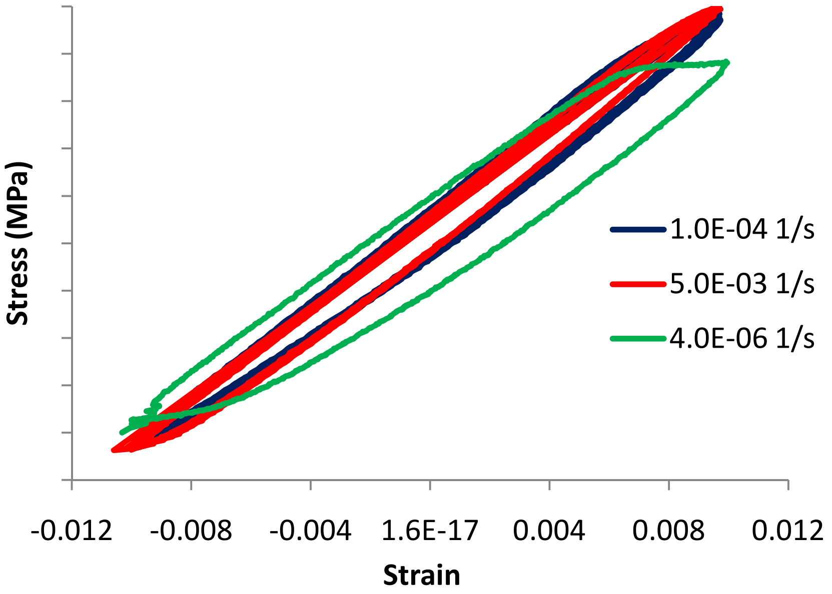

Figure 6.5: Calibration experiment response in the longitudinal direction at 750 °C

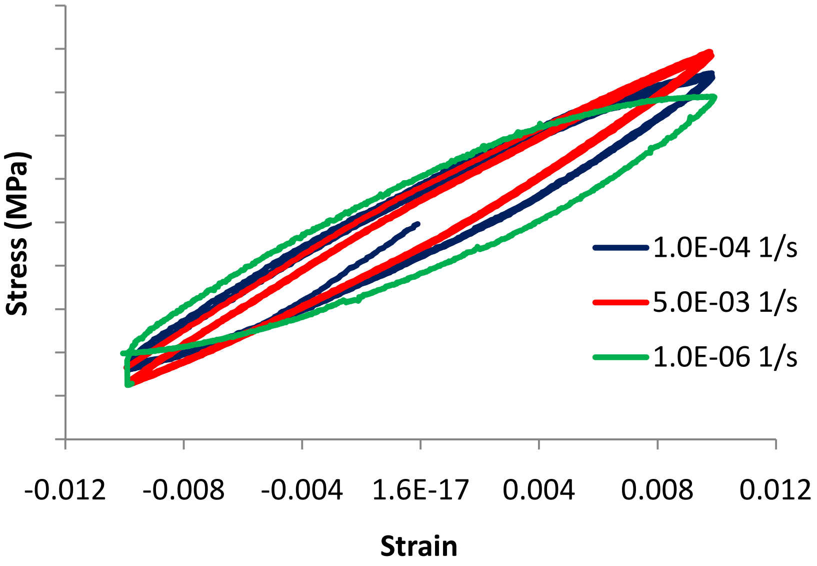

Figure 6.6: Calibration experiment response in the longitudinal direction at 850 °C

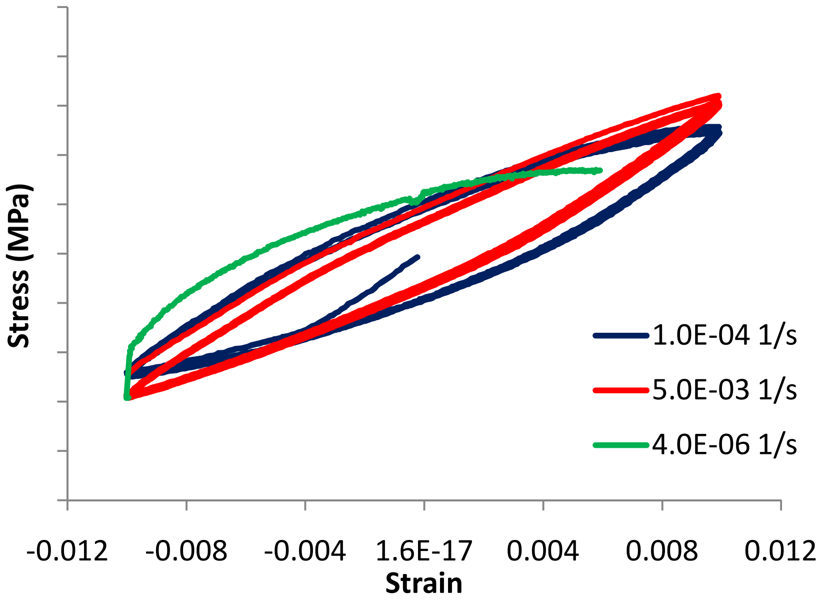

Figure 6.7: Calibration experiment response in the longitudinal direction at 950 °C

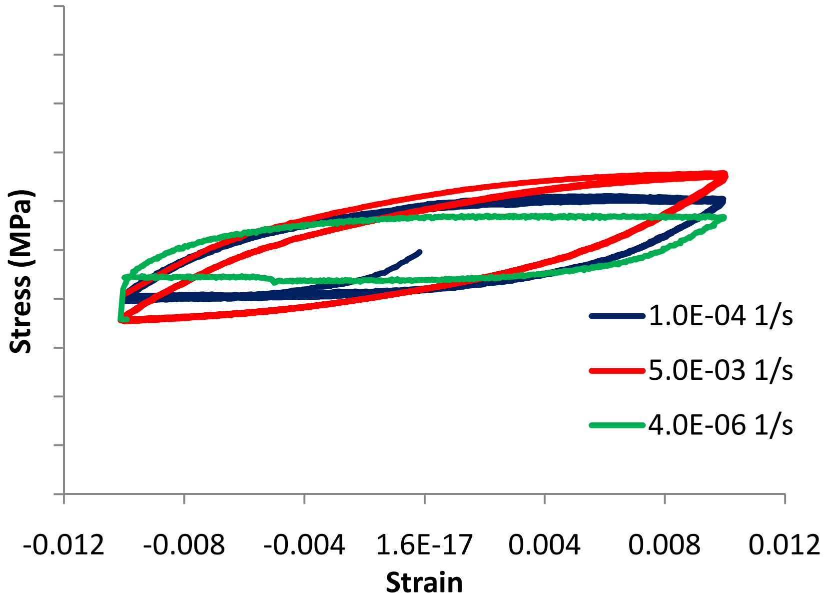

Figure 6.8: Calibration experiment response in the longitudinal direction at 1050 °C

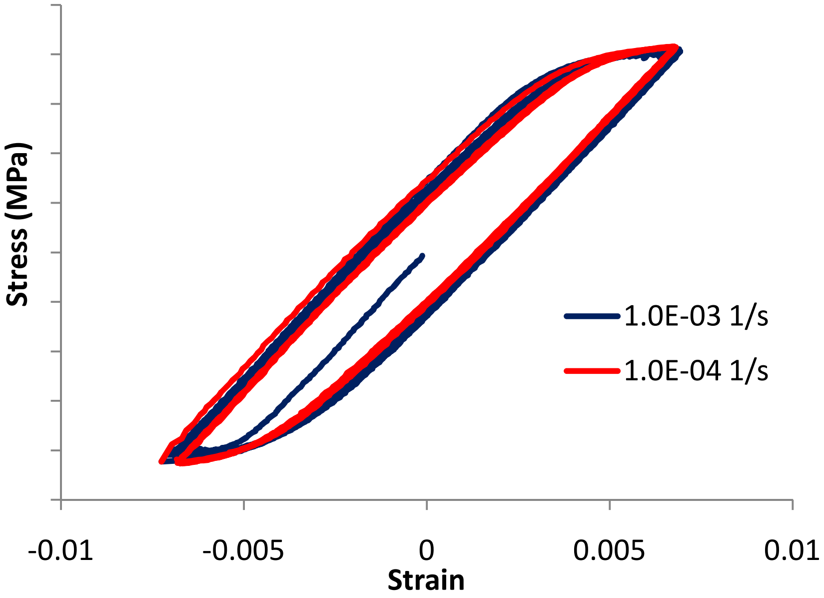

Figure 6.9: Calibration experiment response in the transverse direction at 400 °C

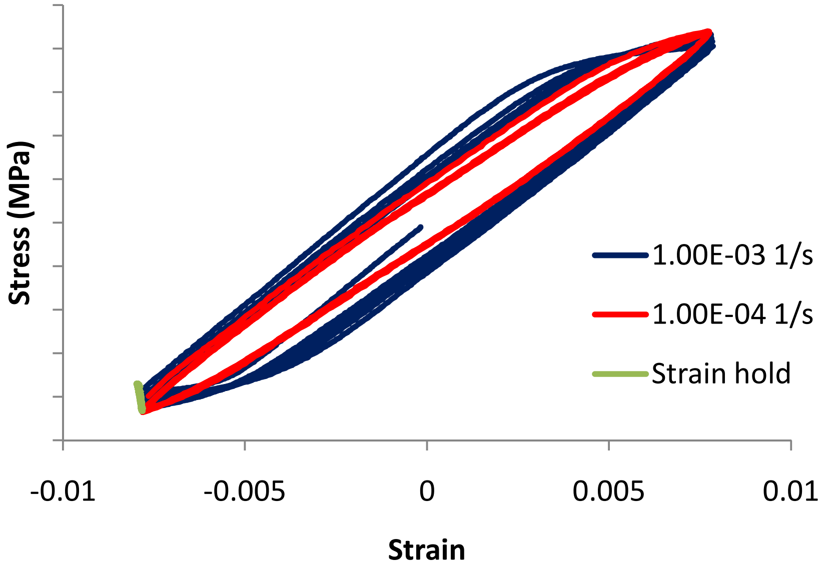

Figure 6.10: Calibration experiment response in the transverse direction at 750 °C

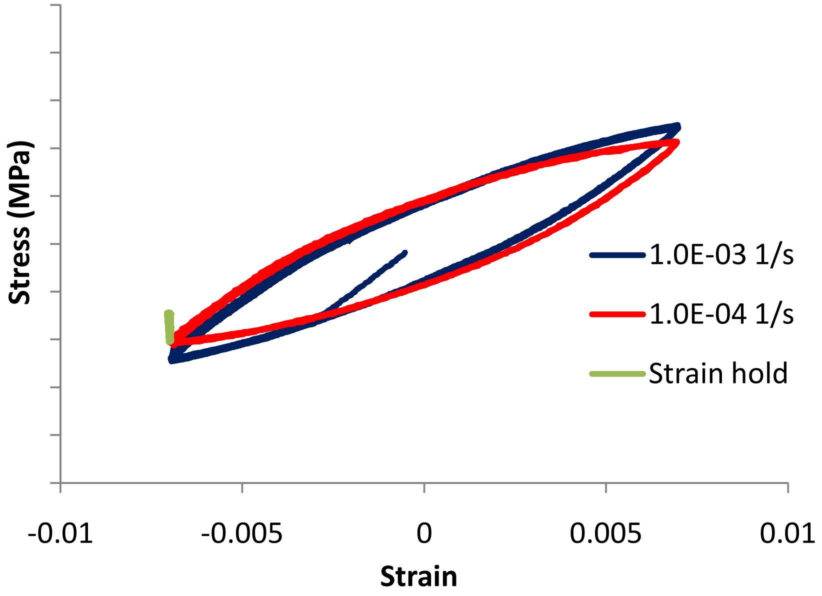

Figure 6.11: Calibration experiment response in the transverse direction at 950 °C

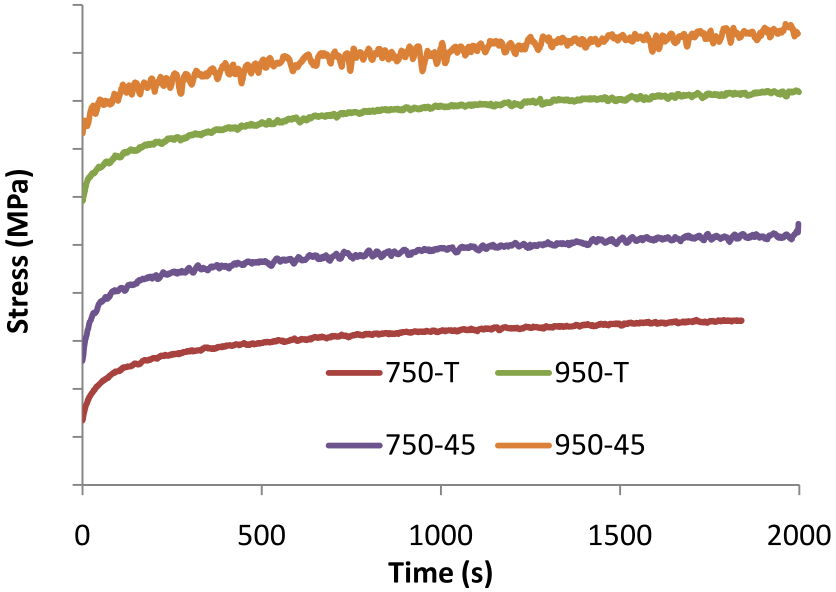

Figure 6.12: Experimental stress relaxation data in the transverse and 45° off-axis directions for compressive strain holds

Figure 6.13 - Figure 6.15 show the 45° off-axis experimental data which was obtained from the experiments listed in Table 5.6. This data was not used in the calibration process and was therefore available for model validation. The experiment at 400 °C experienced serrated yielding which decreased in severity as the experiment progressed, and was greater in compression than in tension.

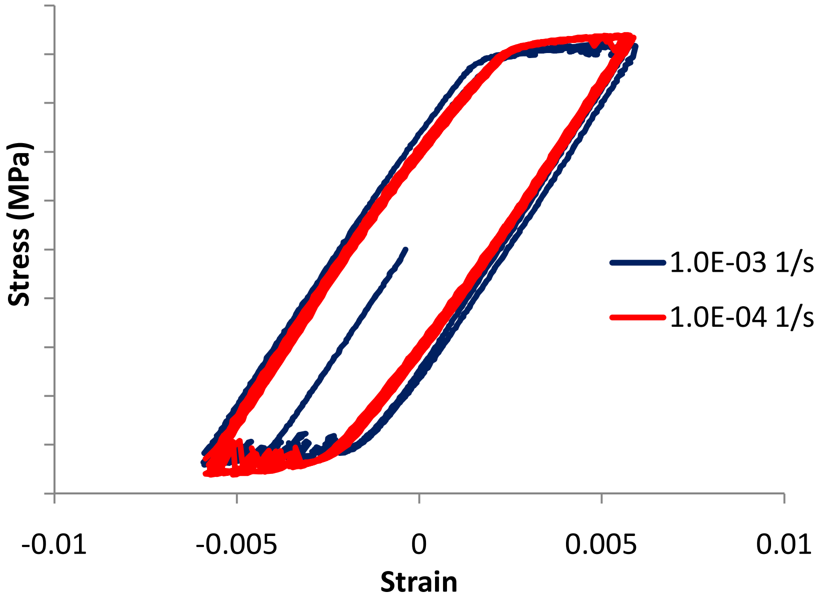

Figure 6.13: Validation experiment in the 45° off-axis direction at 400 °C

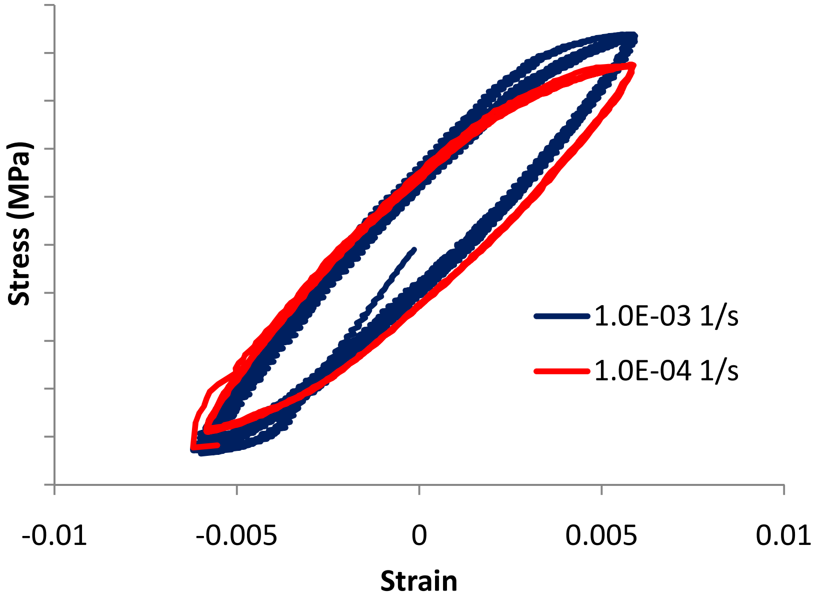

Figure 6.14: Validation experiment in the 45° off-axis direction at 750 °C

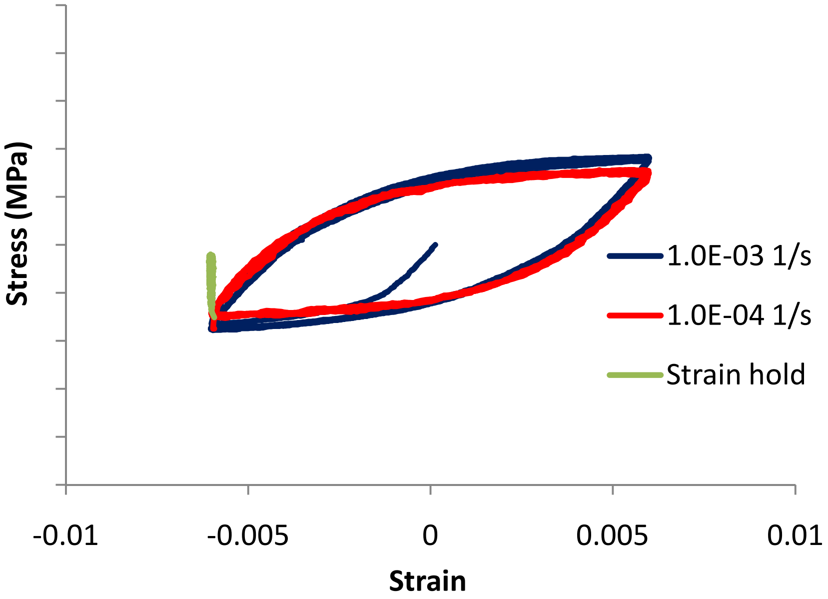

Figure 6.15: Validation experiment in the 45° off-axis direction at 950 °C

Figure 6.16 and Figure 6.17 show the data from the TMF experiments listed in Table 5.7. Each one has a temperature range of 100 – 950 °C. The first one has a cycle time of 1700s, and the second one has a cycle time of 6600s due to repeated strain holds. The strain and temperature profile for the second experiment is shown in Figure 6.18. In both cases the experiments were run to failure, where it is defined as fracture. Due to the large cyclic plastic strain, the cyclic peak stresses, shown in FIGYY, never stabilized so the load drop criterion could not be used.

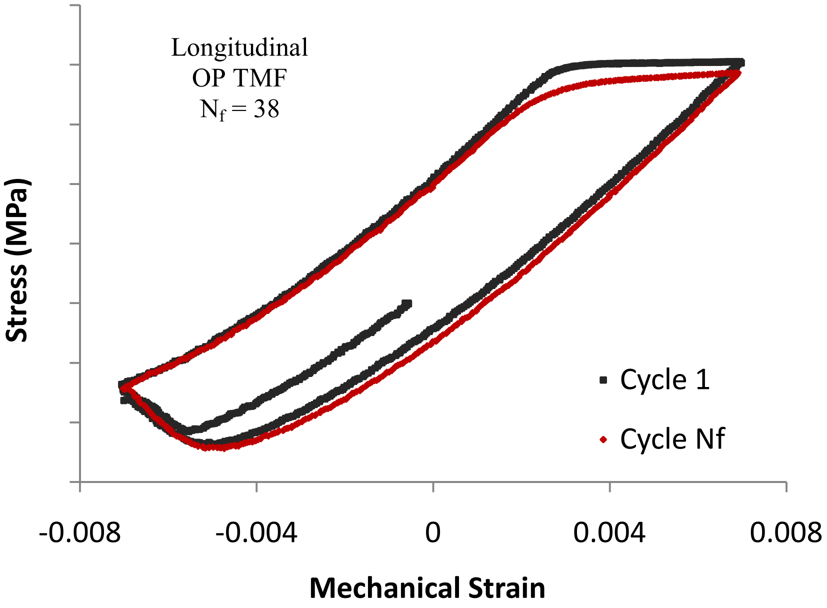

Figure 6.16: OP TMF experiment with temperature range 100-950 °C, 1750s cycle time, no holds

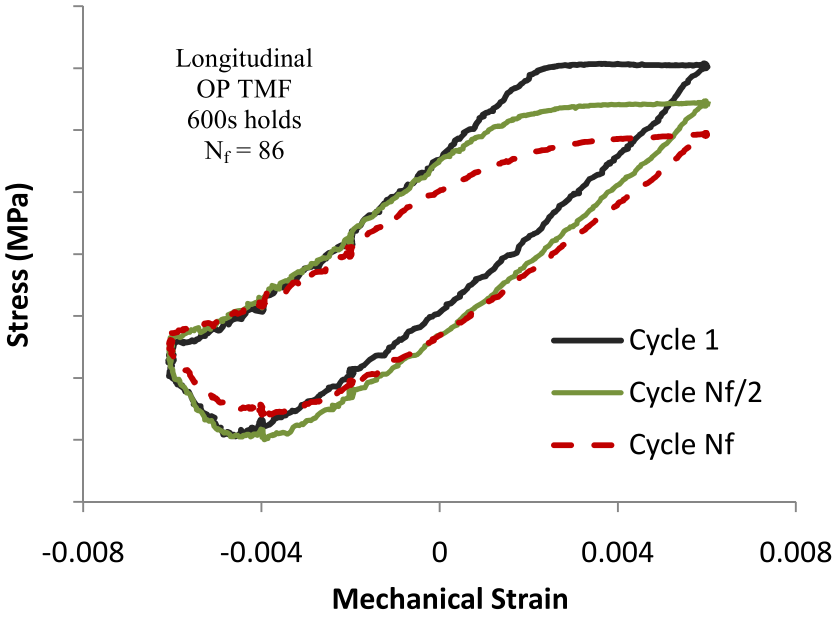

Figure 6.17: OP TMF experiment with temperature rage 100-950 °C, 110 minute cycle time, with six 800s holds per cycle

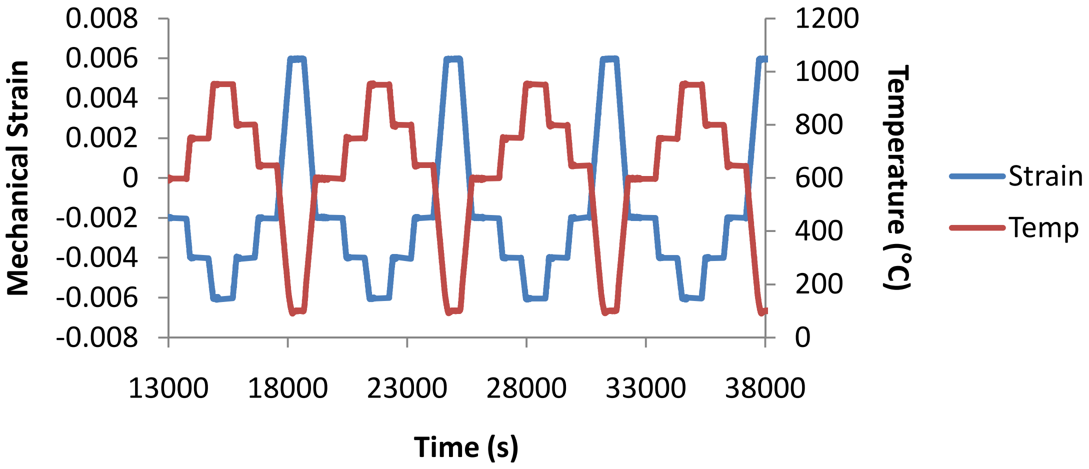

Figure 6.18: Strain and temperature history for second OP TMF experiment

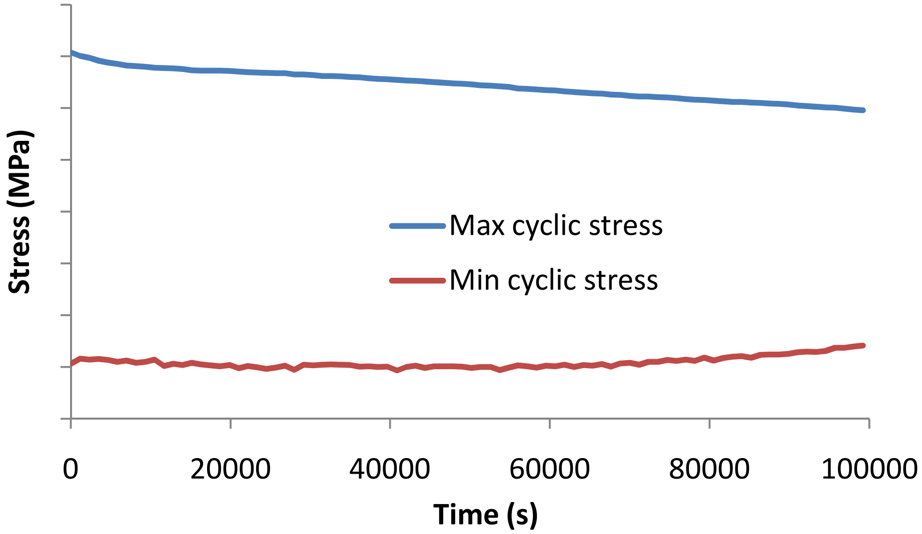

Figure 6.19: Peak cyclic stress for second OP TMF experiment

# Chapter 7. Parameterization Results

After performing the calibration procedures outlined in Chapter 4, the model was calibrated to the test data obtained for DS-CM247LC shown in Chapter 6. The parameterization process resulted in a model which accurately predicted the test data at multiple temperatures, strain rates, and orientations. The calibrated model was then used to predict material behavior in an additional loading direction as well as thermomechanical loading and both were compared to experimental data. These results are described in this chapter.

## 7.1 Isothermal Calibration Results

The model was first calibrated to isothermal experiments in the longitudinal direction. Figure 7.1 shows these calibrations, which have been separated by temperature. Note that the model does a good job of simulating all three strain rates used at each temperature. The best isothermal result is at 950 °C and the worst is at 750 °C.

The model was then calibrated to transverse data. Figure 7.2 shows the results of this calibration. The parameters determined during this stage were the cubic back stress parameters, $h_\chi^{\mathrm{cub}}$, $R_\chi^{\mathrm{cub}}$, $h_{\chi\mathrm{s}}^{\mathrm{cub}}$, and $r_{\chi\mathrm{s}}^{\mathrm{cub}}$, cubic drag stress, $D_0^{\mathrm{cub}}$, and the cubic $B_0^{\mathrm{cub}}$ along with the non-Schmid factors $h_{\mathrm{pe}}$, $h_{\mathrm{se}}$, and $h_{\mathrm{cb}}$. Additional temperature dependence in the cubic parameters was not required for accurate representation of the data and so was omitted to reduce complexity. The Euler angles for this calibration procedure are $\varphi_1 = 90°$, $\Phi = 0°$ to $81°$, and $\varphi_2 = 0°$ which are shown in Table 7.1. The loading directions resulting from these angles are shown in Figure 7.3, where “x”, “y”, and “z”, denote the global coordinate system and the dashed lines are the ten loading directions. The direction of solidification for these Euler angles is in the material y-direction as shown in the figure. The initial parameterizations were performed using ten grains which according to Shenoy (2006) is sufficient for DS alloys. Initial analyses of model performance were conducted with thirty grains, but the simulation times were found to be two and a half times longer than those with only ten grains. Additionally the difference in model response with ten and thirty grains was negligibly small, so ten grains was used for the remaining analyses. The results of the calibration agree well with the experimental data at all temperatures.

Table 7.1: Euler angles used for calibration to transverse experiments

| $\varphi_1$ | $\Phi$ | $\varphi_2$ |
|---|---|---|
| 90 | 0 | 0 |
| 90 | 9 | 0 |
| 90 | 18 | 0 |
| 90 | 27 | 0 |
| 90 | 36 | 0 |
| 90 | 45 | 0 |
| 90 | 54 | 0 |
| 90 | 63 | 0 |
| 90 | 72 | 0 |
| 90 | 81 | 0 |

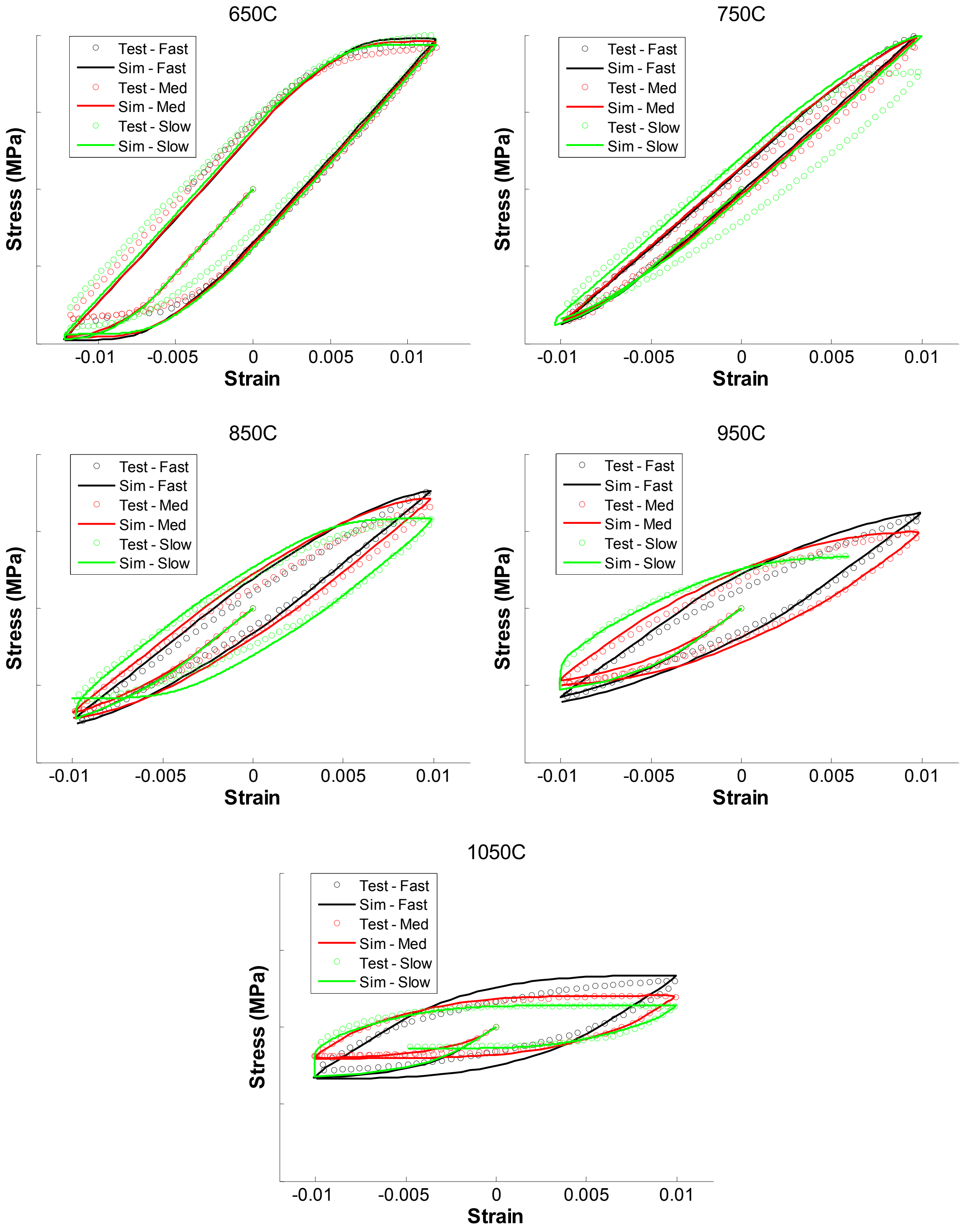

Figure 7.1: Correlation of model and calibration experiments in the longitudinal orientation

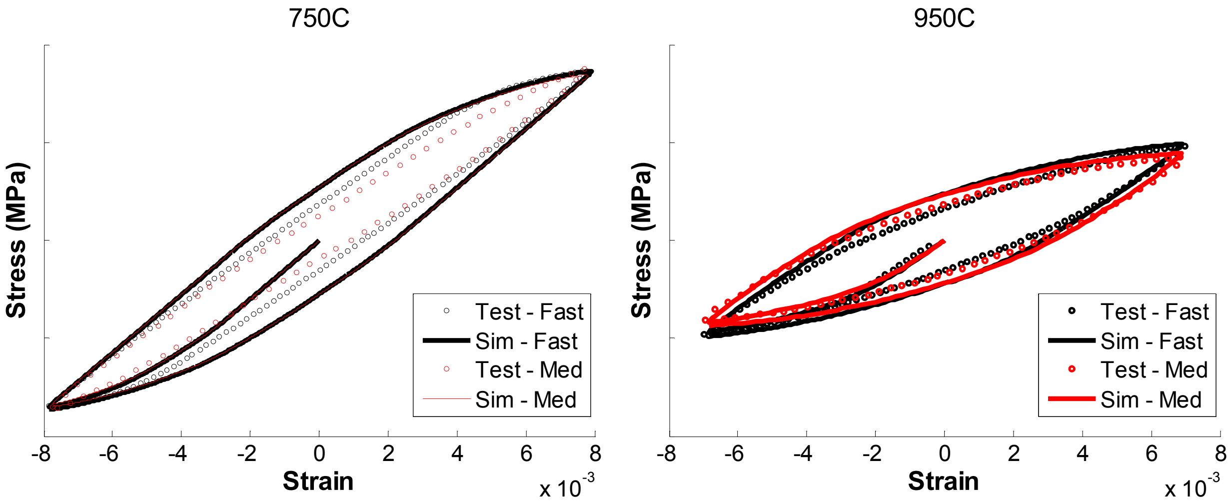

Figure 7.2: Correlation of model and calibration experiments in the transverse orientation

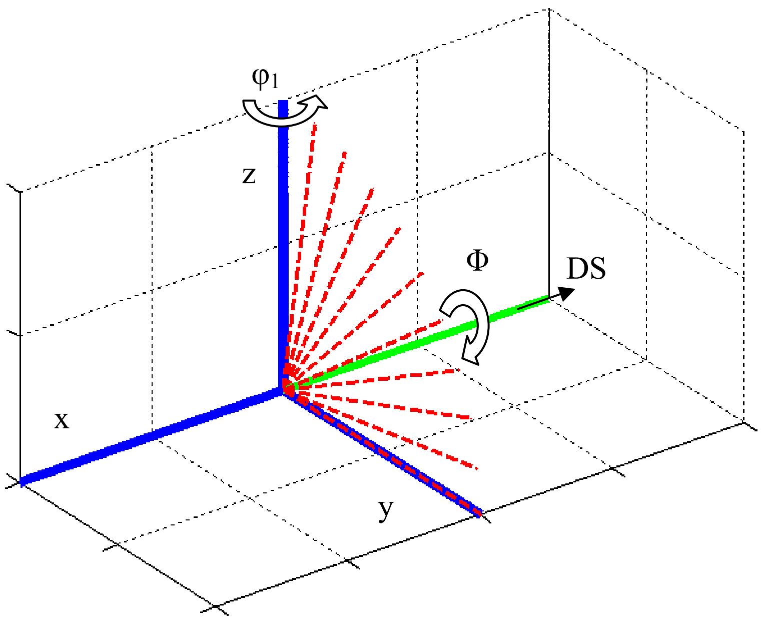

Figure 7.3: Illustration of Euler angles used to determine transverse response

The calibration was then compared to experimental response for 45° off-axis loading. The Euler angles used in these simulations are graphically shown in Figure 7.4. Note that each loading direction is 45° from the direction of solidification which is achieved through setting the first Euler angle to 45°, and randomly varying the second Euler angle. The maximum allowed time step is a critical value during these simulations because the modulus of elasticity is larger in the non-longitudinal directions than in the longitudinal direction which results in larger increments of stress in the elastic prediction. The results are shown in Figure 7.5. Note that in Figure 7.5 (b) there is excessive hardening and the yield stress is too high. It is postulated the specimen used at 950 °C may have contained a limited number of grains which biased the experiment. This could be verified with additional testing, but has not been done.

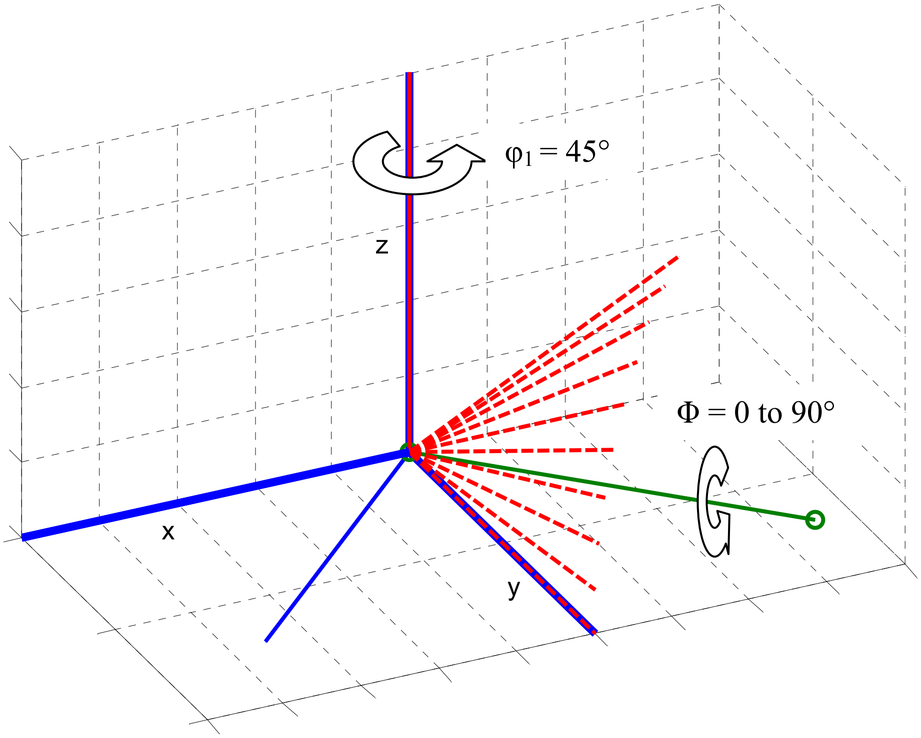

Figure 7.4: Illustration of Euler angles used to determine 45° off-axis response

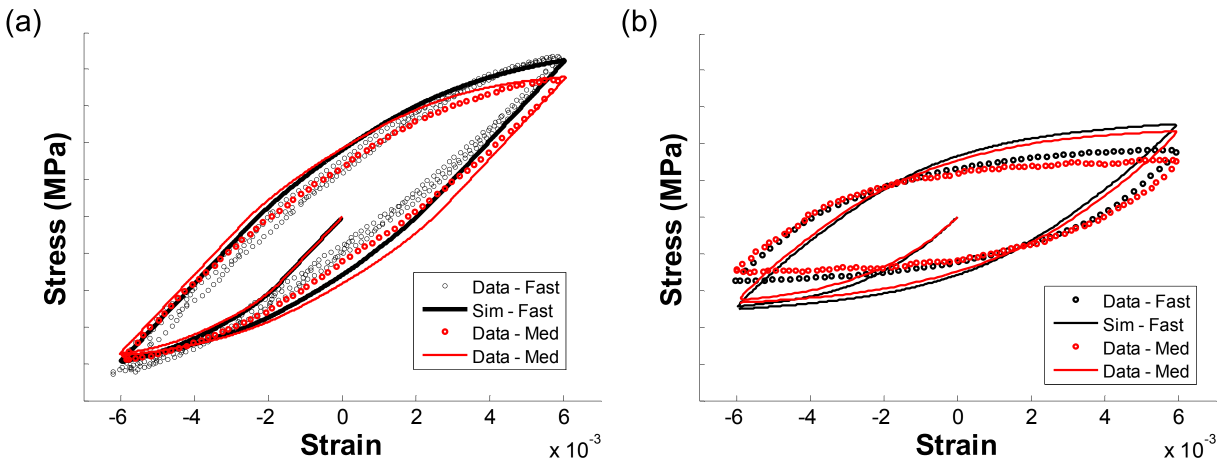

Figure 7.5: Comparison between 45° off-axis test data and predicted response at (a) 750° C and (b) 950° C

The calibration of the CTE, $\beta$, was achieved using the thermal cycling of a TMF experiment and Eq. (4.42) & (4.43). The thermal cycling data is shown in Figure 7.6 with the prediction resulting from this calibration. The model prediction matches the experimental data well.

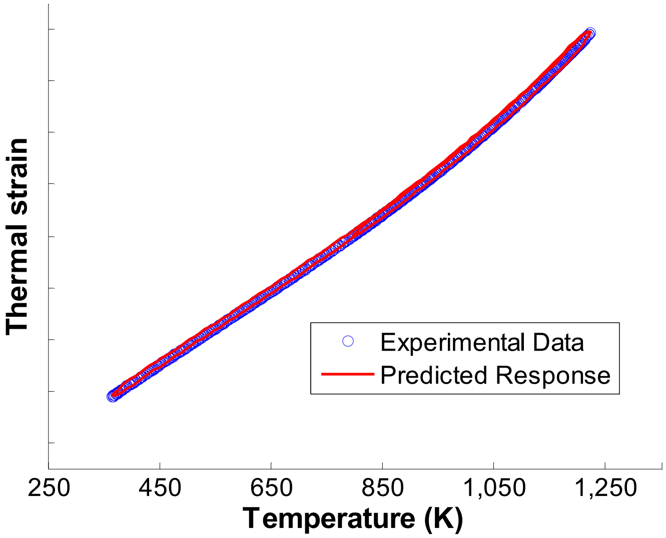

Figure 7.6: Comparison between thermal cycling and predicted response between 100 – 950 °C

## 7.2 Thermomechanical Simulations

Finally the calibrated model was compared to the thermomechanical cyclic response as shown in Figure 7.7. It was found that the model accurately predicted the maximum and minimum stresses of the experiment, but did not accurately predict the entire deformation history. Of particular importance is the behavior going from compression to tension, or high temperature to low temperature. Here the experimental data shows a more sharp transition from elastic behavior to plastic behavior, while the model predicts a gradual transition, beginning at a much lower stress. The cause of this errant prediction is thought to come from dynamic strain aging (Christ and Bauer, 2011) which causes dislocation arrangements to differ from high temperature deformation to low temperature deformation. The theory here is that the deformation at higher temperatures causes dislocation patterns which restrict deformation at lower temperatures and cause isothermal calibrations to wrongly predict yielding in TMF loadings. Presently the CVP model does not capture this mechanism.

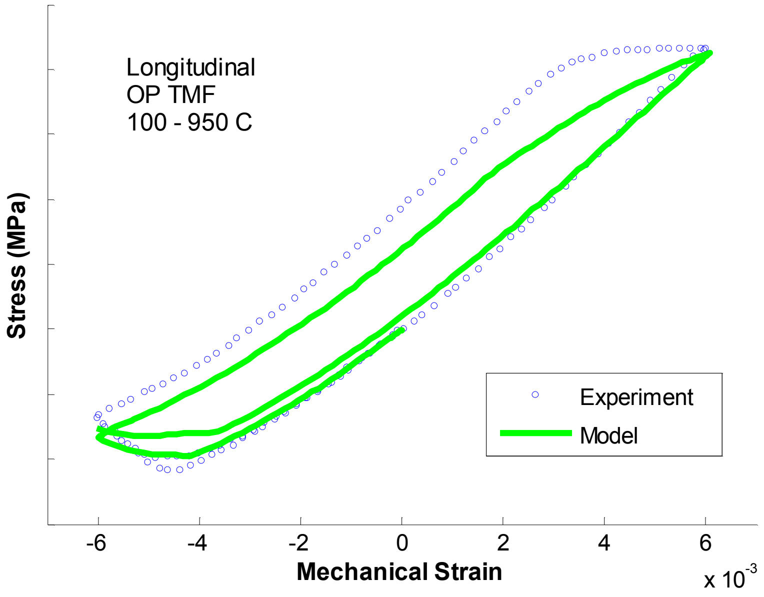

Figure 7.7: Comparison between experimental and predicted response for OP TMF between 100 and 950 °C

# Chapter 8. Parametric Study

The CVP model is capable of simulating much more complex loadings than just the fully-reversed constant amplitude LCF and TMF tests used to calibrate and validate the model. To demonstrate the predictive power of the CVP model it was run with a series of control points which lie outside of normal constraints, but for which there exists considerable experimental precedents. Isothermal LCF is first considered, followed by TMF calculations. The following is a description of this study and a discussion of the results.

## 8.1 LCF Predictions

Two LCF predictions are run with 600s strain holds included; one at 750 °C and one at 950 °C. To further emphasize the difference between them each contains a cycle without a strain hold as is shown in Figure 8.1. As can be seen in Figure 8.2, at 750 °C there is a much smaller range of cyclic plasticity than at 950 °C for both the cycle with and without the strain hold. Additionally, at 750 °C a smaller change in cyclic plasticity between the cycle with the hold and the one without is observed than at 950 °C. This result is expected since the amount of stress relaxation is greatly increased in the 200 °C between these two temperatures.

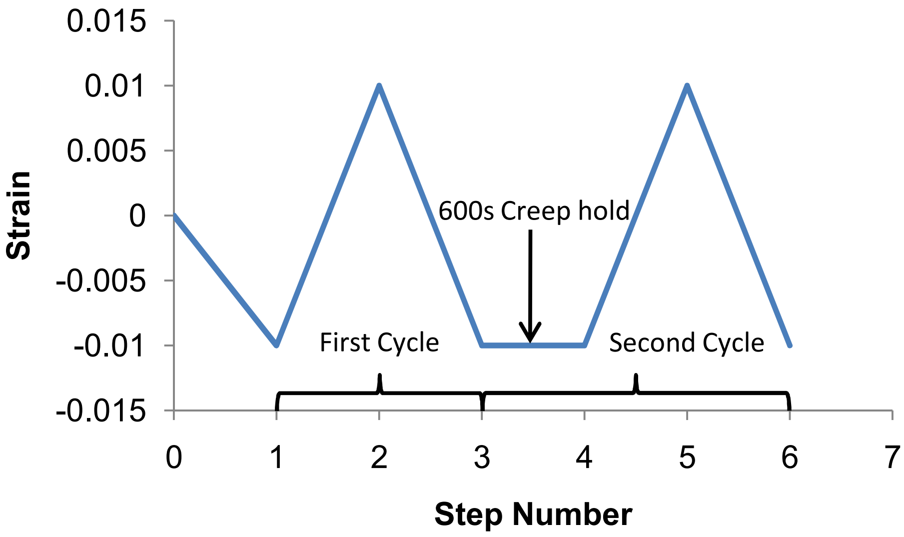

Figure 8.1: Strain history for isothermal model predictions with strain holds

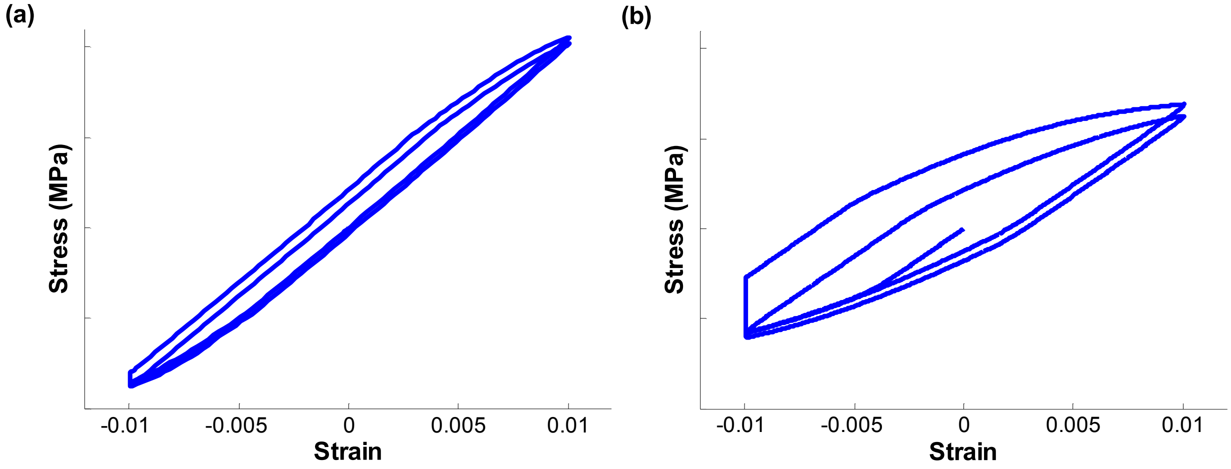

Figure 8.2: Comparison of predictions at a strain rate of 5.0x10$^{-3}$ s$^{-1}$ with strain holds at (a) 750 °C and (b) 950 °C

All of the experiments conducted and shown in the calibration of the CVP model above have a strain ratio, $R_\varepsilon$, of -1. However, since actual turbine components undergo deformation at different strain rations, the difference between $R_\varepsilon=-\infty$ and $R_\varepsilon=-1$ with strain holds is explored.

The temperature and strain rate used were 850 °C and 5.0x$10^{-3}$ $s^{-1}$, respectively. The results are shown below in Figure 8.3. When fully reversed the cyclic response is stable after the first cycle, while when $R_\varepsilon$=-∞, with half the strain amplitude, the response exhibits ratcheting due primarily to the accumulated creep deformation.

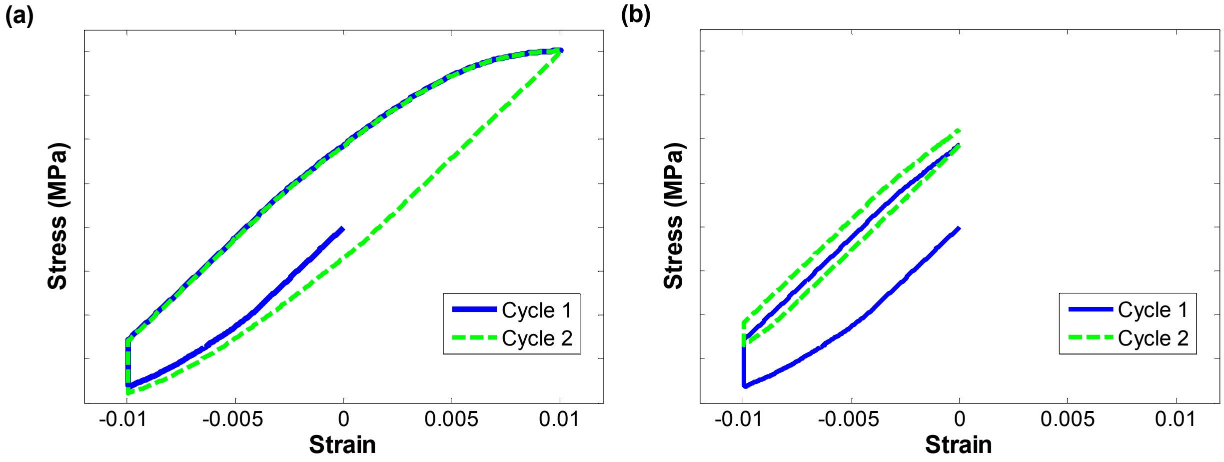

Figure 8.3: Comparison of LCF at 850 °C and a strain rate of 5.0x$10^{-3}$ $s^{-1}$ with $R_\varepsilon$ of (a) -1, and (b) -∞

## 8.2 TMF Predictions

TMF experiments on NI-base superalloys are typically run with a minimum cyclic temperature, $T_{min}$, that is sufficiently low to be in the range where the yield stress is relatively constant down to room temperature. The typical value for $T_{min}$ is 550 °C since the yield stress remains relatively constant between room temperature and this point, but increases with increasing temperature, and then decreasing rapidly after about 750 °C (Reed, 2006), while. With this $T_{min}$ the maximum temperature, $T_{max}$, is then varied, typically between 750 – 1050 °C (Shenoy, 2005; Gordon, 2006; Shenoy et al., 2006; Shenoy, 2006; Kupkovits, 2009). There are, however, a select few who have performed TMF experiments outside of this range (Esmaeili et al., 1995; Okazaki and Sakaguchi, 2008; Kupkovits, 2009). $T_{min}$ is set at this relatively high temperature for experimental expediency: dropping $T_{min}$ causes cycle times to lengthen since the cooling rate of the specimen is directly proportional to the difference between the specimen temperature and ambient temperature. Forced convection can be used to lower the $T_{min}$ without increasing the cycle time, but it is difficult to control such that uniform temperature distributions in the gage section are maintained. The justification for using a $T_{min}$ of 550 °C when the minimum operating temperature of gas turbine engines is around room temperature is that the yield stress does not change between these temperatures. It has been shown, however, that the effect of reducing $T_{min}$ is to include a significant amount of additional cyclic plasticity (Kupkovits et al., 2010). Since fatigue life decreases with increasing cyclic plasticity and since actual components experience $T_{min}$ at around room temperature, it is important to include the actual $T_{min}$ in life prediction of turbine blades. This is demonstrated in Figure 8.4 where the $T_{min}$ of the cycle has been decreased from 550 °C to 100 °C with a $T_{max}$ held constant at 950 °C. For comparison purposes the mechanical strain rate is held constant at $1x10^{-6}$/s between the two cases. Each case is initially started at its mean temperature: 525 °C for $T_{min}$ = 100 °C and 750 °C for $T_{min}$ = 550 °C. The temperature change rate was dictated by the mechanical strain rate and was 1 °C/s for $T_{min}$ = 100 °C and 0.5 °C/s for $T_{min}$ = 550 °C.

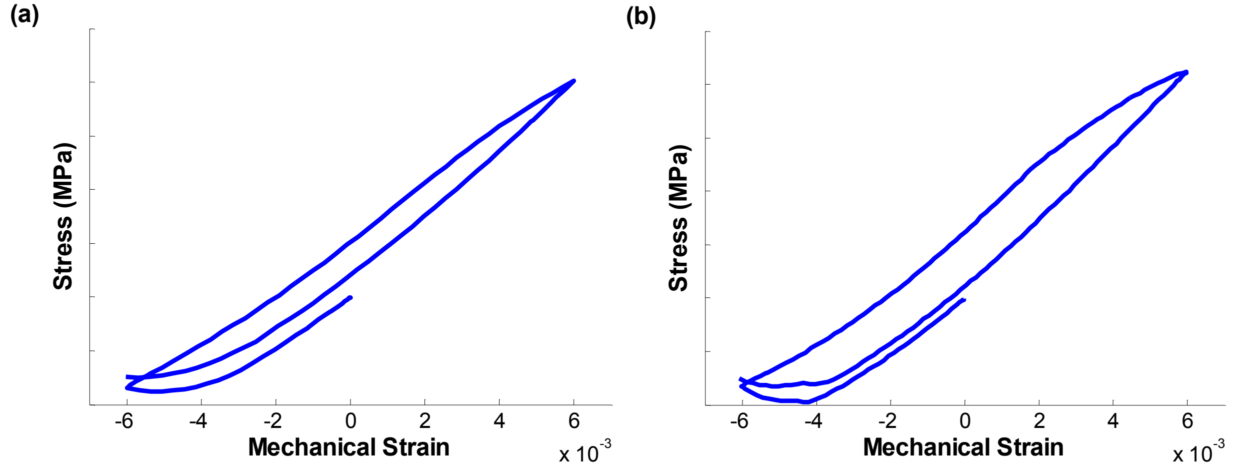

Figure 8.4: Comparison of TMF with $T_{max}$ of 950 °C, R = -1, and (a) $T_{min}$= 550 °C and (b) $T_{min}$= 100 °C

The model response for different TMF cycle types was also predicted. These include linear in phase (IP), linear out of phase (OP), and counter clockwise diamond cycles. For reference the temperature-strain-time histories for each of these cycles are shown in Figure 8.5. Figure 8.6 shows the model response for each cycle type with the mechanical strain range held constant. Of the three cycle types the one with the least plasticity is the diamond cycle. This happens because the mean temperature, where both the maximum and minimum strains occur, is in a region where the yield stress is high. Between the OP and IP cycle types, OP has slightly more initial plasticity, but as can be seen in the figure its cyclic plasticity is approximately the same as the IP prediction. The IP prediction however ratchets toward negative stresses and has a lower stabilized mean stress while the OP prediction ratchets toward positive stresses and has a higher stabilized mean stress.

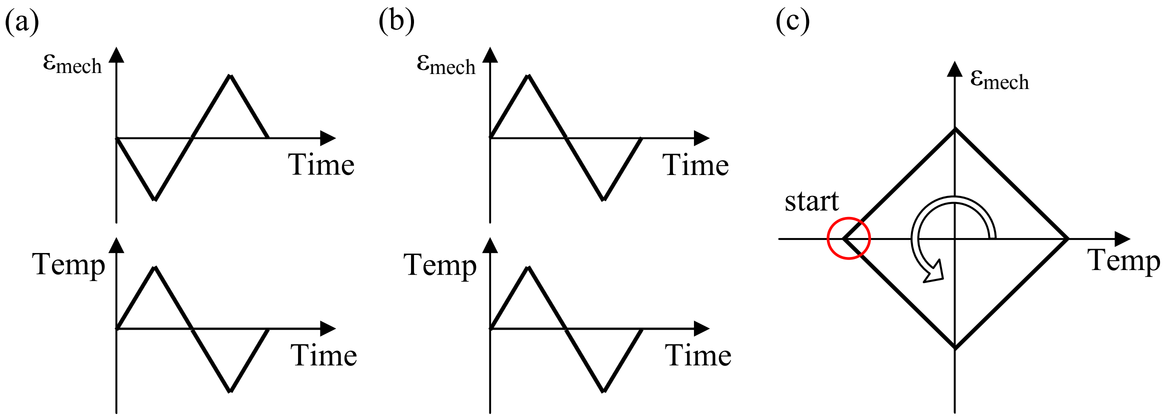

Figure 8.5: Temperature and strain history for (a) OP, (b) IP, and (c) counter clockwise diamond cycle types

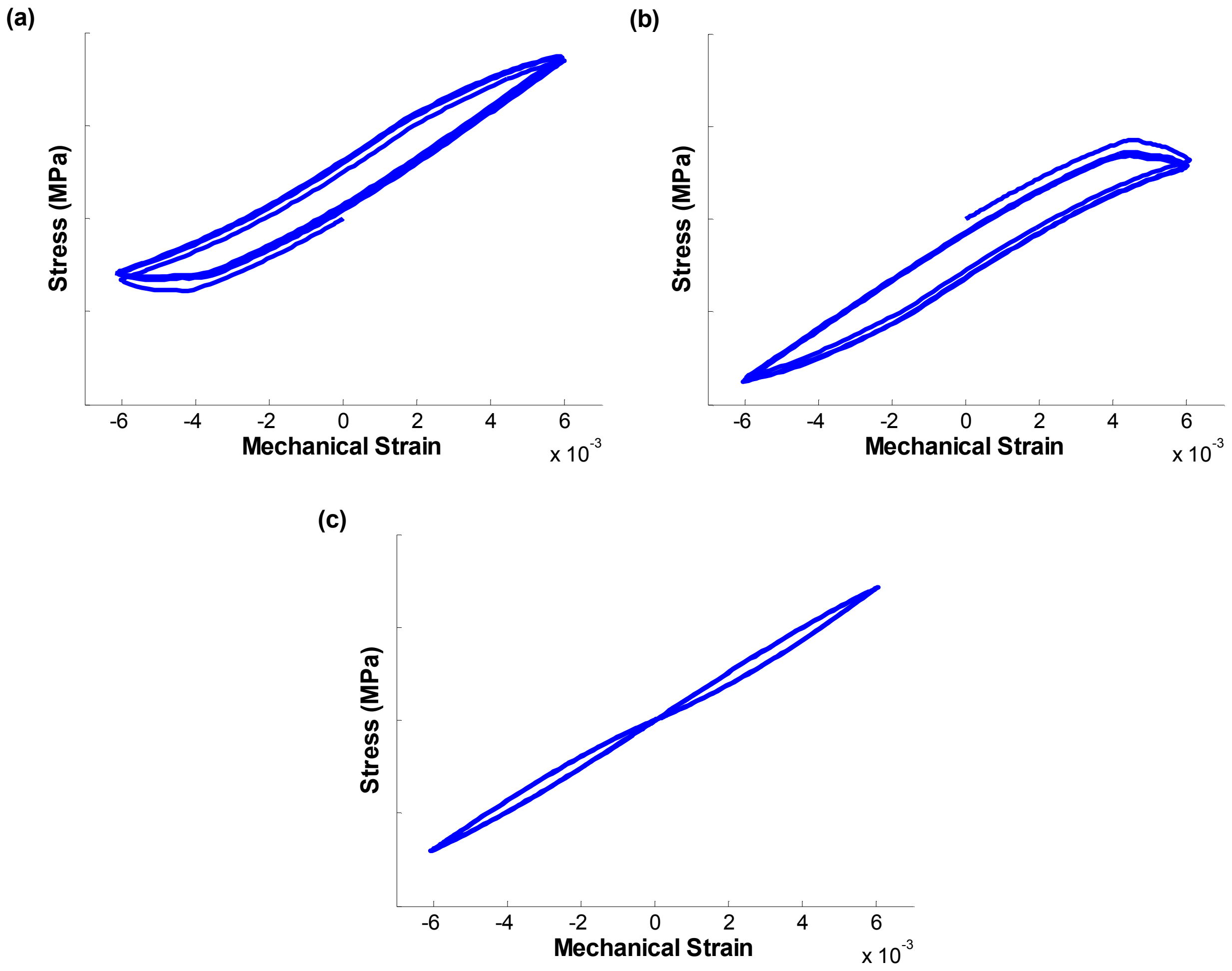

Figure 8.6: Comparison of TMF model predictions with different cycle types: (a) IP, (b) OP and (c) diamond. All analyses are 100-950 °C, with half cycle times of 850s.

Again, because an $R_\varepsilon$ ratio of -1 is not representative of most actual loadings in turbine blades several predictions have been made with $R_\varepsilon$ ratios of 0 and $-\infty$, and then compared to an $R_\varepsilon$ of -1. These are shown in Figure 8.7. The temperature change rate and starting temperature of each was 1 °C/s and 525 °C, respectively. All have approximately the same cyclic plasticity and stabilized stress range, although there is significantly more accumulated plasticity for both the $R_\varepsilon$ of $-\infty$ and 0 in the early cycles.

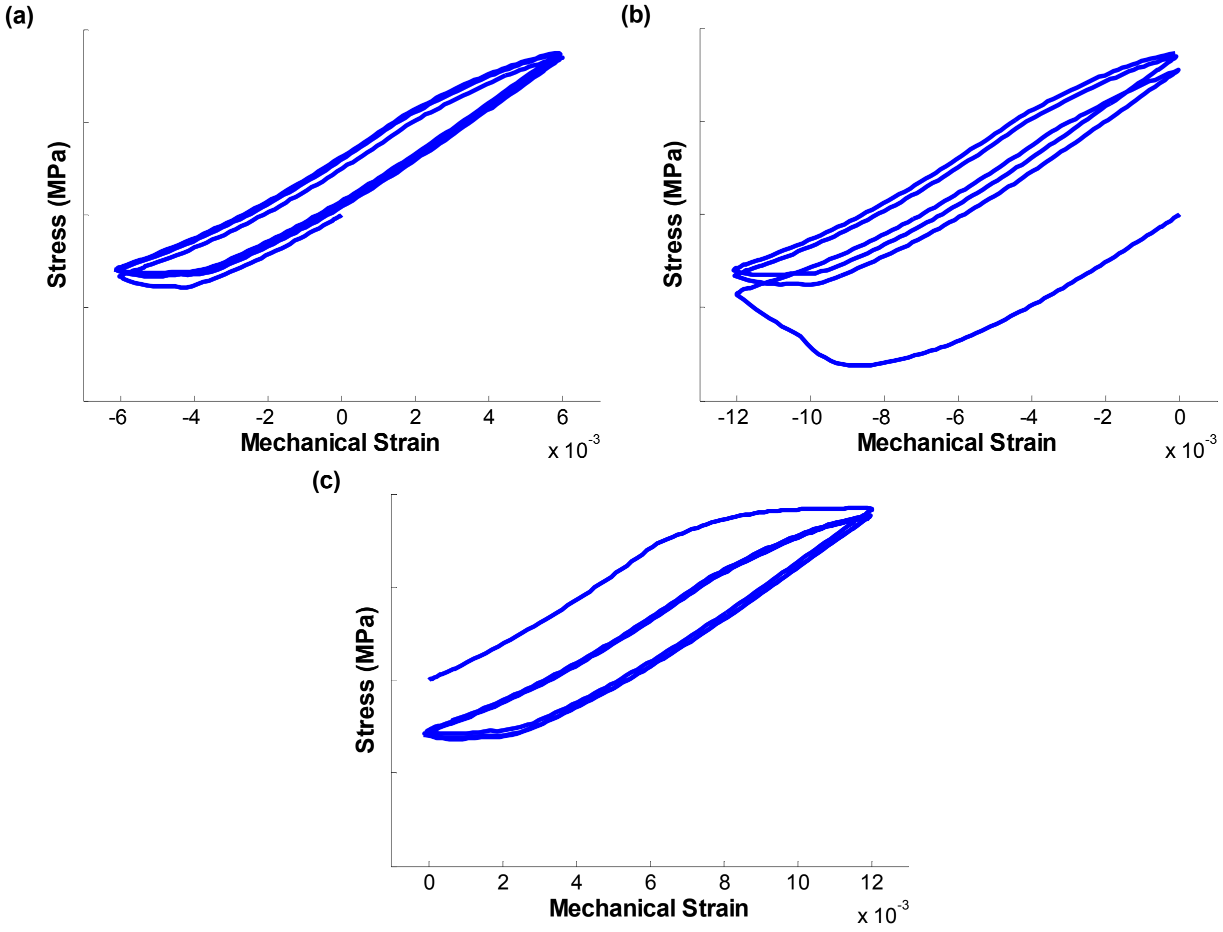

Figure 8.7: Comparison of 100-950 °C TMF cycles with a mechanical strain range of $1.2\text{x}10^{-2}$ and $R_\varepsilon$ of (a) -1, (b)-∞, and (c) 0

# Chapter 9. Conclusions and Recommendations

## 9.1 Conclusion

In this work a method for rapidly determining parameters for the crystal viscoplasticity model over a wide temperature range was developed. These protocols and procedures reduce the time needed to determine material parameters, allowing for the models use in industry, where previous calibration times restricted its application. Components of this method are listed below and include: parameter grouping, a hierarchy of parameters and groups, a roadmap for isothermal parameter determination, and a method for transitioning from isothermal parameters to temperature dependent ones.

- A roadmap for rapidly determining temperature-dependent parameters for the CVP model was created. Parameters of the CVP model are grouped by function and dependence resulting in the categories of elastic constants and CTE, yield stress, hardening, flow rule, and creep. This grouping allows for the separation of parameters whose function is related to a certain data type which reduces the interdependencies which exist between parameters. A hierarchical pathway through the groups was constructed to reduce the dependence of each group on others. Additionally the parameters within each group are ranked according to sensitivity and interdependence so that an order of parameterization is created where there is limited iteration between parameters. Finally a type of data is defined for use in the calibration of each parameter. This allows each parameter to be calibrated to data towards which it is most sensitive, and restricts multiple parameters from being determined from identical data.

- A series of calibration protocols were established which result in the accurate calibration of the model to experimental data. Parameter values are first determined at points in temperature from isothermal experiments. Polynomials are then created to describe the behavior of each parameter with respect to temperature. Finally, parameters which are not temperature-dependent are determined through calibration across the entire testing temperature range. The result is an efficient method for determining temperature-dependent parameters across a range of temperatures that has not previously been attempted.
- Calibration experiments for use with the above protocols were created and performed. A total of eight experiments, six longitudinal and two transverse, are performed for the calibration of the model. Four additional experiments, two at 45° off-axis from the direction of solidification and two TMF, are conducted for validation of the calibrated model. Each calibration experiment contains a minimum of three strain rates at least a decade apart from each other. Additionally a significant amount of plasticity is included in each experiment so that the calibration of the plasticity parameters and internal state variables is efficiently and accurately achieved.
- The CVP model was calibrated to the directionally solidified Ni-base superalloy DS-CM247LC between room temperature and 1050 °C. This temperature range is larger than any other CVP calibration temperature range previously attempted and allows the simulation of loadings with temperature ranges similar to those experienced in the hot section of gas turbine engines. To achieve the temperature dependence necessary to describe this temperature range the protocols and procedures above were utilized. All of the calibration experiments are accurately simulated with the calibrated model. The 45°

off-axis experiments are well predicted at 750 °C, but are over predicted at 950 °C. The TMF experiments are well predicted by the calibrated model.

## 9.1 Recommendations

Since the scope and depth of this research was limited by time constraints it is necessary to list further research which could be completed to improve the function of the model and its predictive capability. These suggestions are given below.

- Since, as mentioned above, the model does not correctly represent the evolution of the back stress under TMF conditions, it is suggested that this be addressed in further model modifications. It is postulated that the proper model modifications will not be difficult to implement since the back stress rate equation is separate from the rest of the model. However, determining how the modification should be implemented and what form they should take are not trivial matters.
- The model does not currently explicitly include microstructure attributes as material parameters. This necessitates the calibration of the model to multiple material microstructures for a single material composition. In particular it is desirable for the volume fraction and morphology and distribution of sizes of $\gamma$' to be explicit parameters. Presently these effects are implicitly lumped in the more sensitive parameters of the model. Including these material attributes as parameters would allow a single calibration to describe a range of microstructures and thus allow simulation of actual components. One step in this direction is the modification of the model to account for changes in the microstructure due to rafting.
- The UMAT currently uses the Newton-Raphson method to converge to a solution. Although this method is in general faster when compared to other methods it is not

bounded and relies on the slope of the error. These characteristics cause the model to not guarantee a solution and to converge proportionally to the slope of the error. For instance, when the temperature is low enough for the material behavior to be quasi rate independent the Newton-Raphson method does not converge quickly because the slope of the error function is exponentially steep. It may therefore be more efficient to use a bounded method at these low temperatures which would ensure convergence and which would allow the specification of a finite search space. One such method would be bisection, which is both relatively fast and robust. Bounded methods are not projected to work well at higher temperatures however where the range of possible solutions could span several decades. Therefore it is proposed that a combination of the Newton-Raphson and a bounded search method be used such that rate insensitive behavior is solved by the bounded method and rate dependent behavior is solved by the Newton-Raphson method.

- The main goal of this research was to accelerate the calibration of the CVP model. One thought is to use optimization methods to make iteration of parameter determination quicker. This was attempted, but due to time constraints and difficulty in implementation it was not feasible to construct optimization protocols which would further enhance the calibration process. However, the codes listed in Appendix D for adjustment of the threshold stress, Code 2 and Code 3, and back stress, Code 4 and Code 5, parameters based upon changes in other parameters could be utilized in an optimization scheme to correct previously calibrated parameters for new parameter trial values. This would allow the hierarchy and parameter determination protocols used in this work to also be applicable to optimizations. Therefore it is suggested that future work focus on establishing optimization codes which would reduce the extent of human intervention in the process of model calibration. A simple model for these optimizations is given in Chapter 4.

- All of the experiments performed in this work are uniaxial in nature. However it is possible to use tension-torsion experiments to separate the back stress from its strain rate dependence. This could be used to get a more accurate look at the back stress evolution and separate it from its interdependencies with other parameters. It is therefore recommended that further research include this type of testing so that the back stress parameters achieved through the parameterization procedures described in this work may be validated.

# Appendix A. UMAT modifications

At the beginning of this work the author was supplied with a UMAT written by McGinty (2001) and modified by Shenoy (2006). This UMAT will from this point forward be referred to as UMAT$^{06}$. In the course of designing parameter determination protocols and determining material parameters for DS-CM247LC it was found necessary to modify this UMAT$^{06}$. The UMAT which resulted from these modifications will from this point on be termed UMAT$^{11}$. This appendix lists a detailed description of the major modifications made to UMAT$^{06}$.

- The UMAT$^{06}$ was modified to allow the input of temperature dependent polynomials directly from the input file. The UMAT$^{06}$ required that the polynomials be hard-coded into the temperature dependent subroutine. Because this does not allow for the easy modification of the parameters for use in optimizations and because this implementation of the temperature dependence would require a unique user material subroutine for different materials or microstructures, it was modified such that the temperature dependent polynomials are controlled from the input file. While this makes reading parameters from the input file difficult it gives full control of the CVP model's temperature dependence to the user without modification of the UMAT$^{11}$. This modification has no effect on the result of the model.
- The internal variable storage of the UMAT$^{06}$ was adjusted to allow for the analysis of multiple grains. Initially the internal variable array, which saves internal state variable values for each slip system, was hard-coded to contain the strains, stress, and temperature after the internal state variables of the first grain. However a second grain would first

errantly use these values as initializations and then save over them. Thus these values were moved to the beginning of the array where they would not be errantly used or erased.

- Correct implementation of the threshold stress was achieved through another modification. The UMAT$^{06}$ implemented the temperature dependence of the threshold stress by multiplication of the shear modulus as shown in the following equation.

$$\tau_v^\alpha = |\tau^\alpha - \chi| - \kappa^\alpha \frac{\mu \cdot \kappa_0^\alpha(T)}{\mu_0} \tag{A.1}$$

  This is valid only if $\kappa^\alpha$ is equal to unity and the rest of the threshold stress components are turned off. In other words, this is not valid if any non-Schmid factor, $h_{pe}$, $h_{se}$, and $h_{cb}$, is non-zero, as well as if any of the threshold stress evolution parameters, $h_0$, $h_{\kappa s}$, and $h_s$, are non-zero. Therefore the UMAT$^{06}$ was modified to match the model shown in Table 3.1 where the temperature dependence of the threshold stress is added to $\kappa_c^\alpha$.

- The calculation of the thermal strain was corrected. In the UMAT$^{06}$ the thermal strain is calculated at the beginning of each elastic prediction by Eq. (4.38) where $\mathbf{F}^\theta$ is found by Eq. (3.10). However at the end of each iteration the thermal strain was calculated from the total and mechanical strain by,

$$\varepsilon_{th} = \varepsilon_T - \varepsilon_{mech} \tag{A.2}$$

  where $\varepsilon_T$ is the total strain and is an input, and $\varepsilon_{mech}$ is the mechanical strain which is calculated during the iteration. Since the thermal strain can be calculated directly from inputs of temperature and CTE, this evaluation of the thermal strain caused numerical errors which were easily visible; the thermal strain would be non-zero for isothermal loadings. Thus the evaluation of thermal strain was modified from Eq. (A.2) to match that of Eq. (4.38). There still exists a minor inaccuracy in mechanical strain, but this is due to the inexact solution of the inelastic shear strain rate. To reduce the error in the mechanical strain one only needs to reduce the tolerance on the solution of the inelastic shear strain rate.

- The UMAT$^{06}$ was modified to eliminate input parameters for parameter derivatives. In UMAT$^{06}$ the derivatives in the back stress temperature rate term were inserted as input parameters. While this is valid so long as the polynomials which are input are derivatives of the parameters, this is redundant as it requires the input of additional polynomial coefficients. Additionally the polynomials which were in use in UMAT$^{06}$ were not derivatives of the back stress polynomials. Therefore the derivatives were implemented through the quotient rule and the extra polynomial coefficients were eliminated.

# Appendix B. Euler Angle Determination

The determination of Euler angles for input into the CVP model is not trivial. Therefore a MATLAB code for Euler angle determination has been created and is shown in Figure B.1. Additionally a script which runs the Euler angle function and plots the result is shown in Figure B.2. Note that the codes will only return two angles. This is because the transformation of a vector in three dimensional space to any other orientation requires only two perpendicular angles. Three angles are required only if the rotation of the vector is important. Since the model uses cubic symmetry the use of this angle is unnecessary in most cases. For this reason the determination of this angle is not included, although it is noted that it is possible to use this angle when it is convenient to do so.

Since multiple grains with random orientations in the transverse direction are needed in a DS alloy to model loading in non-longitudinal directions multiple sets of Euler angles are needed for simulation of these loadings. Take for instance the loading of a DS specimen at 45° from the direction of solidification. The random orientation of grains in the transverse direction makes the determination of a single angle for loading impossible. The approach therefore is to use the first Euler angle to rotate the coordinate system to a point where the loading (in the global y-axis) is 45° from the direction of solidification (a rotation of 45°). The second Euler angle can then be assigned an array of random values which represent individual grains in an experimental specimen. The result is shown in Figure 7.4 where the dashed lines are the resulting directions of loading. Note that each load is 45° from the direction of solidification (in the case the material y-axis). This description is not unique since the rotation is over-constrained by three angles.

```
function [Alpha, Beta, Gamma] = FindEulerAngles(Vector)
% This function computes the Euler angles for use in the Crystal
% Viscoplasticity UMAT.

normVec = Vector/(sum(Vector.^2))^.5;
x = [1 0 0];
y = [0 1 0];
z = [0 0 1];

Alpha_rad = acos(dot(normVec,y));
Alpha = -Alpha_rad/pi*180;

Rz = [cos(Alpha_rad) -sin(Alpha_rad) 0; sin(Alpha_rad) cos(Alpha_rad) 0; 0
0 1];
X = Rz*x';
Z = Rz*z';
normW = Rz*normVec';

Wx = dot(normW,X);
Wz = dot(normW,Z);

Wxz = [Wx 0 Wz];
if sum(Wxz) ~= 0
    WXZ = Rz*Wxz';
    normWXZ = WXZ/(sum(WXZ.^2))^.5;
    normX = X/(sum(X.^2))^.5;
    normWXZx = dot(normWXZ,normX);
    theta = acos(normWXZx)/pi*180;
else
    theta = 180;
end
Beta = theta-180;

Gamma = 0; % this is an arbitrary angle.
% Because only two angles are needed to define a transformation of a vector
% to another arbitrary direction the value of gamma is always zero.
```

Figure B.1: MATLAB function for Euler angle determination

```
% Initialize loading direction Ex: [1 0 0]
a = [1 2 3];

d = (a(1)^2+a(2)^2+a(3)^2)^.5;
A = a/d;

[Alpha Beta Gamma] = FindEulerAngles(A); % Find Euler angles

O1 = Alpha*pi/180; % Convert to radians
O2 = Beta*pi/180;  % Convert to radians
O3 = Gamma*pi/180; % Convert to radians

c1 =cos(O1); c2 =cos(O2); c3 =cos(O3);
s1 =sin(O1); s2 =sin(O2); s3 =sin(O3);

R = [ c1*c2*c3 - s1*s3, - c3*s1 - c1*c2*s3, c1*s2;...
    c1*s3 + c2*c3*s1, c1*c3 - c2*s1*s3, s1*s2; -c3*s2, s2*s3, c2];

% original (global) coordinates
x = [1 0 0]; y = [0 1 0]; z = [0 0 1];

% Rotate coordinate system to new orientation
X = R*x'; Y = R*y'; Z = R*z'; W = R*A';

c = [0;0;0];
v1 = [c X]; v2 = [c Y]; v3 = [c Z]; v4 = [c W];

% Plot original (global) coordinates
plot3([0 1 0 0 0 0 0 0], [0 0 0 1 0 0 0 0], [0 0 0 0 0 1 0 0],...
    'LineWidth',3)
hold on
% plot resulting coordinate system after rotation
plot3(v1(1,:),v1(2,:),v1(3,:),v2(1,:),v2(2,:),v2(3,:),...
    v3(1,:),v3(2,:),v3(3,:),v4(1,:),v4(2,:),v4(3,:))

grid on; xlabel('x'); ylabel('y'); zlabel('z'); axis equal
hold off
```

Figure B.2: Script for finding and plotting Euler angles for specified loading direction

As mentioned previously the grain orientations for loading of multiple grains are supplied to the UMAT[11] through an external text file which contains the grain orientations in units of degrees. This is accomplished on line 326 of the UMAT[11] through an "open" command. Therefore the location of the text file must be correctly specified within the UMAT[11]. Figure B.3

shows a proper file specification, and Figure B.4 shows the corresponding file for loading ten grains at 45° from the direction of solidification.

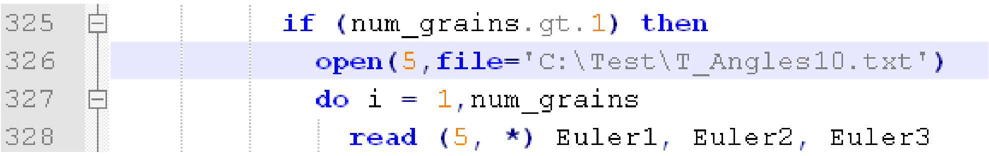

```
if (num_grains.gt.1) then
  open(5,file='C:\Test\T_Angles10.txt')
  do i = 1,num_grains
    read (5, *) Euler1, Euler2, Euler3
```

Figure B.3: File specification in UMAT[11] for multiple grain orientations

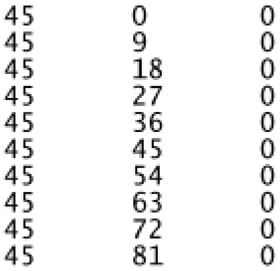

```
45      0       0
45      9       0
45      18      0
45      27      0
45      36      0
45      45      0
45      54      0
45      63      0
45      72      0
45      81      0
```

Figure B.4: Angle specification from external file for multiple grains

# Appendix C. ABAQUS input file

The input parameters have been organized in the ABAQUS input script for easy location and insertion. Figure C.1 shows the parameter input section of a sample input file with the important aspects highlighted. The box under *DEPVAR is the number of positions in the *statev*, which stands for “state-variable”, array. This value should be determined by Eq. (C.1) where *N* is the number of grains in the simulation.

$$DEPVAR = 24 + N * 48 \tag{C.1}$$

Setting this value to a little more than the result of Eq. (C.1) is not detrimental, however setting it to less will cause the simulation to crash. The large box in Figure C.1 contains all of the input parameters necessary to simulate a loading history. Each line of parameter values is preceded by a comment line specifying what each parameter is. The order of parameters must not be changed unless the UMAT is modified accordingly. The dashed box at the bottom of the figure contains the starting temperature for the history. This value should be set to the initial temperature at which the thermal strain is zero.

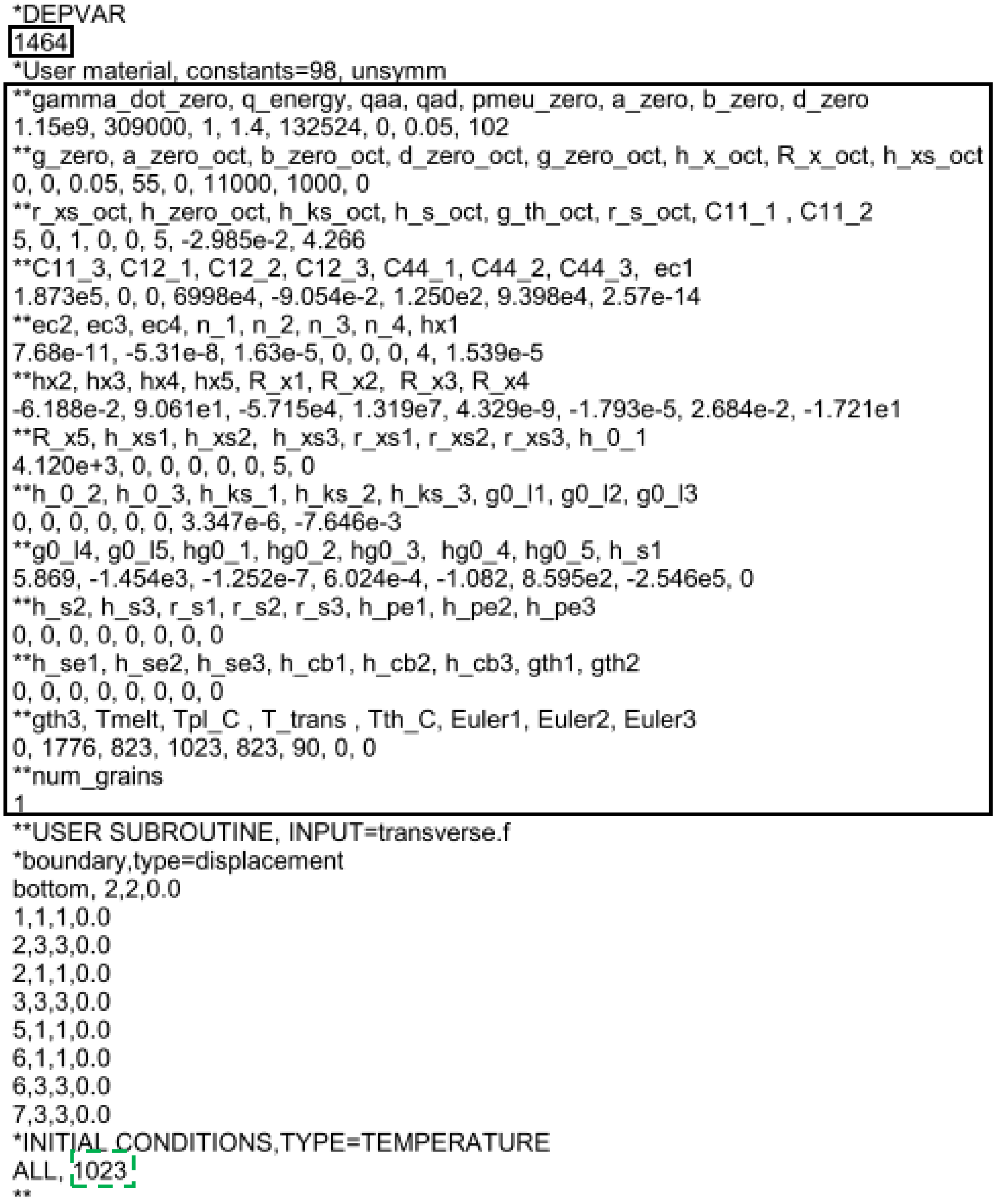

```
*DEPVAR
1464
*User material, constants=98, unsymm
**gamma_dot_zero, q_energy, qaa, qad, pmeu_zero, a_zero, b_zero, d_zero
1.15e9, 309000, 1, 1.4, 132524, 0, 0.05, 102
**g_zero, a_zero_oct, b_zero_oct, d_zero_oct, g_zero_oct, h_x_oct, R_x_oct, h_xs_oct
0, 0, 0.05, 55, 0, 11000, 1000, 0
**r_xs_oct, h_zero_oct, h_ks_oct, h_s_oct, g_th_oct, r_s_oct, C11_1 , C11_2
5, 0, 1, 0, 0, 5, -2.985e-2, 4.266
**C11_3, C12_1, C12_2, C12_3, C44_1, C44_2, C44_3,  ec1
1.873e5, 0, 0, 6998e4, -9.054e-2, 1.250e2, 9.398e4, 2.57e-14
**ec2, ec3, ec4, n_1, n_2, n_3, n_4, hx1
7.68e-11, -5.31e-8, 1.63e-5, 0, 0, 0, 4, 1.539e-5
**hx2, hx3, hx4, hx5, R_x1, R_x2,  R_x3, R_x4
-6.188e-2, 9.061e1, -5.715e4, 1.319e7, 4.329e-9, -1.793e-5, 2.684e-2, -1.721e1
**R_x5, h_xs1, h_xs2,  h_xs3, r_xs1, r_xs2, r_xs3, h_0_1
4.120e+3, 0, 0, 0, 0, 0, 5, 0
**h_0_2, h_0_3, h_ks_1, h_ks_2, h_ks_3, g0_l1, g0_l2, g0_l3
0, 0, 0, 0, 0, 0, 3.347e-6, -7.646e-3
**g0_l4, g0_l5, hg0_1, hg0_2, hg0_3,  hg0_4, hg0_5, h_s1
5.869, -1.454e3, -1.252e-7, 6.024e-4, -1.082, 8.595e2, -2.546e5, 0
**h_s2, h_s3, r_s1, r_s2, r_s3, h_pe1, h_pe2, h_pe3
0, 0, 0, 0, 0, 0, 0, 0
**h_se1, h_se2, h_se3, h_cb1, h_cb2, h_cb3, gth1, gth2
0, 0, 0, 0, 0, 0, 0, 0
**gth3, Tmelt, Tpl_C , T_trans , Tth_C, Euler1, Euler2, Euler3
0, 1776, 823, 1023, 823, 90, 0, 0
**num_grains
1
**USER SUBROUTINE, INPUT=transverse.f
*boundary,type=displacement
bottom, 2,2,0.0
1,1,1,0.0
2,3,3,0.0
2,1,1,0.0
3,3,3,0.0
5,1,1,0.0
6,1,1,0.0
6,3,3,0.0
7,3,3,0.0
*INITIAL CONDITIONS,TYPE=TEMPERATURE
ALL, 1023
**
```

Figure C.1: Parameter input section of a sample input file

Figure C.2 shows a sample step specification portion of an input file with the important aspects highlighted. The box directly under “*STATIC” contains time values which dictate how the step is to be performed. The first value is the initial time increment for the step. This should be set to a small number for the first step and set to less than the maximum time increment of the previous step otherwise. ABAQUS only allows a 1.5x increase is time increment so if the initial time increment of a step is larger than the previous maximum time increment by more than 1.5x the analysis will crash. The next value is the total time that the step should consume and can be used to control the strain rate. The third value in this line is the minimum time increment allowed in the step. This value should be small enough to ensure convergence of the simulation. The final value is the maximum allowed time increment. This value is critical to ensuring convergence of the model and in keeping the analysis from crashing. Because most steps will start as an elastic increment the UMAT is allowed to increase the time step until it reaches the maximum value. Once the threshold stress is exceeded the UMAT still uses the elastic solution as its initial prediction and then corrects for plasticity. This initial elastic stress however can cause the predicted inelastic shear strain rate to overshoot with errors being larger than the overflow value. Thus the first action taken if an error code of 144 or 693 is generated should be the reduction of the maximum time increment. The box underneath “*TEMPERATURE” contains the temperature at the end of the step. The next box down contains the ending value of the total strain. It is emphasized here that the loading history is controlled through total strain unlike thermomechanical testing which is controlled through mechanical strain. Thus for thermomechanical predictions the thermal strain must be included in the input strain. The dashed box which comes next contains the data output interval in seconds. This value is only important for those who wish to use the CAD file which is generated during the analysis. Because this file is difficult to access it is not used in this calibration of the model. Rather the “.dat” text file is used. This file contains the result of each increment performed during the analysis and is not affected by the output time interval. Because the output of data to the CAD file is time consuming and can slow an analysis down significantly the output interval is set to a large number so that a minimal amount of time is spent generating the ".odb" file. Finally the box at the bottom of the figure contains the data which is output to the ".dat" text file. The letters "SDV_" specify the *statev* array in the UMAT, and the number represents the position in the array. There are a number of options here: anything that can be accessed in the CAD file can be output as text from here. In the figure the first value is the stress in the loading direction, $\sigma_{22}$, and subsequent values are the total strain, mechanical strain, elastic strain, plastic strain, thermal strain, and temperature, respectively.

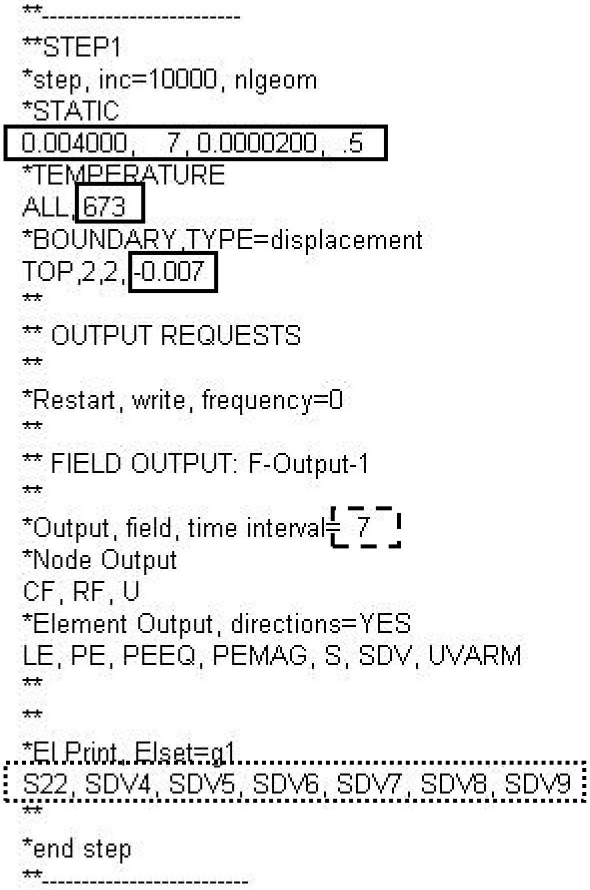

```
**------------------------
**STEP1
*step, inc=10000, nlgeom
*STATIC
0.004000,    7, 0.0000200,  .5
*TEMPERATURE
ALL,673
*BOUNDARY,TYPE=displacement
TOP,2,2,-0.007
**
** OUTPUT REQUESTS
**
*Restart, write, frequency=0
**
** FIELD OUTPUT: F-Output-1
**
*Output, field, time interval= 7
*Node Output
CF, RF, U
*Element Output, directions=YES
LE, PE, PEEQ, PEMAG, S, SDV, UVARM
**
**
*El Print, Elset=g1
S22, SDV4, SDV5, SDV6, SDV7, SDV8, SDV9
**
*end step
**-------------------------
```

Figure C.2: Step specification section of a sample input file

As noted the parameter values in Figure C.1 have a comment line above them specifying what each parameter is. However, these are the code names and do not necessarily have an obvious connection to the model parameter symbols. Therefore Table C.1 is included below to assist in converting between code names and model symbols. Additionally for reference the parameter values for PWA-1484 are included.

Table C.1: Parameter code names and symbols

| **Code name** | **Model Symbol** | **Units** | **GTD-111 Parameter Value** | **T-dependence implementation** |
|---|---|---|---|---|
| gamma_dot_zero | $\dot{\gamma}_0$ | 1/s | $1.15*10^9$ | NA |
| q_energy | $Q_0$ | KJ/mol | 309000 KJ/mol | |
| qaa | $q^{\alpha\beta}$ | - | 1 | |
| qad | | | 1.4 | |
| pmeu_zero | $\mu_0$ | MPa | 166000 MPa | |
| a_zero | $\chi_0$ | | 0 | |
| b_zero | $B_0$ | | 0.05 | |
| d_zero | $D_0$ | | 102 MPa | |
| g_zero | $\kappa_0$ | | 0 | |
| a_zero_oct | $\chi_{0\ oct}$ | | 0 | |
| b_zero_oct | $B_{0\ oct}$ | | 0.05 | |
| d_zero_oct | $D_{0\ oct}$ | | 55 | |
| g_zero_oct | $\kappa_{0\ oct}$ | | 0 | |
| h_x_oct | $h_{\chi\ oct}$ | | 11000 MPa | |
| R_x_oct | $R_{\chi\ oct}$ | | 1000 MPa | |
| h_xs_oct | $h_{\chi s\ oct}$ | odd units | 0 | |
| r_xs_oct | $r_{\chi s\ oct}$ | - | 0 | |
| h_zero_oct | $h_{0\ oct}$ | MPa | 0 | |
| h_ks_oct | $h_{\chi s\ oct}$ | - | 0 | |
| h_s_oct | $h_{s\ oct}$ | odd units | 0 | |
| g_th_oct | $\kappa_{th\ oct}$ | MPa | 0 | |
| r_s_oct | $r_{s\ oct}$ | - | 0 | |

Table C.1 (continued)

| Code name | Model Symbol | Units | GTD-111 Parameter Value | T-dependence implementation |
|---|---|---|---|---|
| C11_1 | $C_{11}$ | MPa | -2.985E-02 | Polynomial |
| C11_2 | | | 4.266E+00 | |
| C11_3 | | | 1.873E+05 | |
| C12_1 | $C_{12}$ | | 0 | |
| C12_2 | | | 0 | |
| C12_3 | | | 6.998E+04 | |
| C44_1 | $C_{44}$ | | -9.054E-02 | |
| C44_2 | | | 1.250E+02 | |
| C44_3 | | | 9.398E+04 | |
| ec1 | CTE | 1/K | -2.57E-14 | |
| ec2 | | | 7.86E-11 | |
| ec3 | | | -5.31E-8 | |
| ec4 | | | 1.63E-5 | |
| n_1 | $n$ | NA | NA | |
| n_2 | | | NA | |
| n_3 | | | NA | |
| n_4 | | | 4 to 5 | |
| hx1 | $h_\chi$ | MPa | 1.539E-05 | |
| hx2 | | | -6.188E-02 | |
| hx3 | | | 9.061E+01 | |
| hx4 | | | -5.715E+04 | |
| hx5 | | | 1.319E+07 | |
| R_x1 | $R_\chi$ | | 4.329E-09 | |
| R_x2 | | | -1.793E-05 | |
| R_x3 | | | 2.684E-02 | |
| R_x4 | | | -1.721E+01 | |
| R_x5 | | | 4.120E+03 | |
| h_xs1 | $h_{\chi s}$ | odd units | 0 | Exponential |
| h_xs2 | | | 0 | |
| h_xs3 | | | 0 | |

Table C.1 (continued)

| **Code name** | **Model Symbol** | **Units** | **GTD-111 Parameter Value** | **T-dependence implementation** |
|---|---|---|---|---|
| r_xs1 | $r_{\chi s}$ | NA | 0 | Polynomial |
| r_xs2 | | | 0 | |
| r_xs3 | | | 5 | |
| h_0_1 | $h_0$ | MPa | 0 | |
| h_0_2 | | | 0 | |
| h_0_3 | | | 0 | |
| h_ks_1 | $h_{\kappa s}$ | - | 0 | |
| h_ks_2 | | | 0 | |
| h_ks_3 | | | 0 | |
| g0_l1 | $\kappa_0$(T) low temp | MPa | 0 | |
| g0_l2 | | | 3.347E-06 | |
| g0_l3 | | | -7.646E-03 | |
| g0_l4 | | | 5.869E+00 | |
| g0_l5 | | | -1.454E+03 | |
| hg0_1 | $\kappa_0$(T) high temp | | -1.252E-07 | |
| hg0_2 | | | 6.024E-04 | |
| hg0_3 | | | -1.082E+00 | |
| hg0_4 | | | 8.595E+02 | |
| hg0_5 | | | -2.546E+05 | |
| h_s1 | $h_s$ | odd units | 0 | |
| h_s2 | | | 0 | |
| h_s3 | | | 0 | |
| r_s1 | $r_s$ | - | 0 | |
| r_s2 | | | 0 | |
| r_s3 | | | 0 | |
| h_pe1 | $h_{pe}$ | | 0 | |
| h_pe2 | | | 0 | |
| h_pe3 | | | 0 | |
| h_se1 | $h_{se}$ | | 0 | |
| h_se2 | | | 0 | |
| h_se3 | | | 0 | |
| h_cb1 | $h_{cb}$ | | 0 | |
| h_cb2 | | | 0 | |
| h_cb3 | | | 0 | |

Table C.1 (continued)

| **Code name** | **Model Symbol** | **Units** | **GTD-111 Parameter Value** | **T-dependence implementation** |
|---|---|---|---|---|
| gth1 | $\kappa_{th}$ | MPa | 0 | Polynomial |
| gth2 | | | 0 | |
| gth3 | | | 0 | |
| Tmelt | $T_m$ | K | 1776 | NA |
| Tpl_C | - | | 823 | |
| T_trans | - | | 1023 | |
| Tth_C | - | | 823 | |
| Euler1 | $\varphi_1$ | degrees | 90 | |
| Euler2 | $\Phi$ | | 0 | |
| Euler3 | $\varphi_2$ | | 0 | |
| num_grains | - | - | 1 | |

# Appendix D. MATLAB codes

Codes have been developed to assist in determining parameter values for the CVP model used in this work. This appendix shows these.

Figure D.1 shows a MATLAB function for calculating the shear stress needed to cause a specific inelastic strain rate. It can be used for estimating both $\kappa_0$(T) and $R_\chi$. Inputs are the inelastic shear strain rate for a slip system, which can be found from the strain rate for saturated hardening by,

$$\dot{\gamma} = 0.306221 * \dot{\varepsilon} \tag{D.1}$$

where $\dot{\varepsilon}$ is the strain rate for an experiment, and the flow rule parameters, $n$, $B_0$, $D_0 \frac{\mu}{\mu_0}$, and $\Theta$(T).

Code 1

```
function tauv = find_tauv_given_g_dot(g_dot,guess,n,B0,Da,C)
%% function to find a value for tauv that results in the desired Epl_dot.
%  Note that RECURSION is used here!!!
%
% INPUTS:
%   g_dot - gamma_dot for steady state test
%   guess - 1x3 vector of shear stress guesses
%      guess(1) - lower bound of shear stress (=0)
%      guess(2) - start point
%      guess(3) - upper bound of shear stress (=400)
%   n - flow exponent
%   B0 - rate independent modification to the drag stress
%   Da - drag stress (=D0*pmeu(T)/pmeu0)
%   C - first term in flow rule (=gamma_dot_0*exp(-Q/R/T) for T>Tm/2)
%
% OUTPUT: tauv - shear stress required to cause the inelastic rate of
%                  deformation

Tolerance = 1e-12;

psr_try(2) = C*((guess(2)/Da)^n)*exp(B0*(guess(2)/Da)^(n+1))*sign(g_dot);
Error(2) = g_dot - psr_try(2);
if abs(Error(2))<Tolerance %done!!
    tauv = guess(2);
else
    psr_try(1)=C*((guess(1)/Da)^n)*exp(B0*(guess(1)/Da)^(n+1))*sign(g_dot);
    psr_try(3)=C*((guess(3)/Da)^n)*exp(B0*(guess(3)/Da)^(n+1))*sign(g_dot);
    Error = [(g_dot-psr_try(1)),Error(2), (g_dot-psr_try(3))];

    E1 = Error(1)*Error(2);
    E2 = Error(2)*Error(3);
    if E1<0 % the initial guess was too high
        guess = [guess(1), (guess(1)+guess(2))/2, guess(2)];
    elseif E2<0 % the initial guess was too low
        guess = [guess(2), (guess(2)+guess(3))/2, guess(3)];
    else % High bound was too low - increase bound slowly
        guess = [guess(3) guess(3)+9 guess(3)+10];
    end
    tauv = find_tauv_given_g_dot(g_dot,guess,n,B0,Da,C); % Recursion
end
```

Figure D.1: MATLAB function to find shear stress needed to cause a given inelastic shear strain rate

Figure D.2 and Figure D.3 combined create a tool for determining the threshold stress given changes in other parameters. They work by adjusting the threshold stress until the saturation inelastic shear strain rate from the first set of parameter values matches the saturation inelastic shear strain rate from the new parameter values.

### Code 2

```
% Initialize parameters
g_dot_0_o = 1.15e9; % Old value of g_dot_0
Q0_o = 309000;      % Old value of Q0
D0_o = 90;          % Old value of D0
n_o =  5;           % Old value of n
B0_o = .05;         % Old value of B0
k_o =  100;         % Old value of threshold stress

g_dot_0 = 1.15e9;   % New value of g_dot_0 (same as above if no change)
Q0 = 400000;        % New value of Q0      (same as above if no change)
Da = 95;            % New value of D0      (same as above if no change)
n =  4;             % New value of n       (same as above if no change)
B0 = .05;           % New value of B0      (same as above if no change)

tau_ys = 250; % yield shear stress: converted stress at first yield
Temp = 823; % temperature in degrees K
Tm = 1700; % Melting temp in degrees K

R = 8.314;
if Temp>Tm/2
    Flow_o = g_dot_0_o*exp(-Q0_o/R/Temp);
    Flow = g_dot_0 * exp(-Q0/R/Temp);
else
    Flow_o = g_dot_0_o*exp(-2*Q0_o/R/Tm*log((Tm/2/Temp)+1));
    Flow = g_dot_0 * exp(-2*Q0/R/Tm*log((Tm/2/Temp)+1));
end

% calculate old value of the inelastic shear strain rate
g_dot_old = Flow_o*(((tau_ys-k_o)/D0_o)^n_o)*exp(B0_o*((tau_ys-
k_o)/D0_o)^(n+1));

guess = [0, k_o, k_o+100];
K0_new = find_K0_given_Edot(g_dot_old,guess,tau_ys,n,B0,Da,Flow);
```

Figure D.2: Script for finding new values of $\kappa_0$ if other parameters change: Note that it requires the function *find_K0_given_Edot()*

Code 3

```
function K0_new = find_K0_given_Edot(g_dot,k,t_ys,n,B0,Da,C)

Tolerance = 1e-12;

psr_try(2) = C*(((t_ys-k(2))/Da)^n)*exp(B0*((t_ys-
k(2))/Da)^(n+1))*sign(g_dot);
Error(2) = g_dot - psr_try(2);
if abs(Error(2))<Tolerance %done!!
    K0_new = k(2);
else
    k_try(1) = C*(((t_ys-k(1))/Da)^n)*exp(B0*((t_ys-
k(1))/Da)^(n+1))*sign(g_dot);
    k_try(3) = C*(((t_ys-k(3))/Da)^n)*exp(B0*((t_ys-
k(3))/Da)^(n+1))*sign(g_dot);
    Error = [(g_dot-k_try(1)),Error(2), (g_dot-k_try(3))];

    E1 = Error(1)*Error(2);
    E2 = Error(2)*Error(3);
    if E1<0 % the initial guess was too high
        k = [k(1), (k(1)+k(2))/2, k(2)];
    elseif E2<0 % the initial guess was too low
        k = [k(2), (k(2)+k(3))/2, k(3)];
    else % High bound was too low - increase bound slowly
        k = [k(3) k(3)+9 k(3)+10];
    end
    K0_new = find_K0_given_Edot(g_dot,k,t_ys,n,B0,Da,C); % Recursion
end
```

Figure D.3: Function *find_K0_given_Edot()*: for use with script in Figure D.2

Figure D.4 and Figure D.5 combined create a tool for determining the saturation back stress given changes in other parameters. They work by adjusting the saturation back stress until the saturation inelastic shear strain rate from the first set of parameter values matches the saturation inelastic shear strain rate from the new parameter values.

# Code 4

```
% Initialize parameters
g_dot_0_o = 1.15e9; % Old value of g_dot_0
Q0_o = 309000;      % Old value of Q0
D0_o = 100;          % Old value of D0
n_o =  5;           % Old value of n
B0_o = .001;         % Old value of B0
K0_o = 100;         % Old value of K0
Rx_o =  100;         % Old value of threshold stress

g_dot_0 = 1.15e9;   % New value of g_dot_0 (same as above if no change)
Q0 = 400000;        % New value of Q0      (same as above if no change)
Da = 95;            % New value of D0      (same as above if no change)
n =  4;             % New value of n       (same as above if no change)
B0 = .05;           % New value of B0      (same as above if no change)
K0 = 100;           % New value of K0      (same as above if no change)
tau_sat = 250; % yield shear stress: converted stress at first yield
Temp = 823; % temperature in degrees K
Tm = 1700; % Melting temp in degrees K

R = 8.314;
if Temp>Tm/2
    Flow_o = g_dot_0_o*exp(-Q0_o/R/Temp);
    Flow = g_dot_0 * exp(-Q0/R/Temp);
else
    Flow_o = g_dot_0_o*exp(-2*Q0_o/R/Tm*log((Tm/2/Temp)+1));
    Flow = g_dot_0 * exp(-2*Q0/R/Tm*log((Tm/2/Temp)+1));
end
% calculate old value of the inelastic shear strain rate
g_dot_old = Flow_o*(((abs(tau_sat-Rx_o)-K0_o)/D0_o)^n_o)*...
    exp(B0_o*((abs(tau_sat-Rx_o)-K0_o)/D0_o)^(n+1));
% look through the range to see if there is more than one solution
Rx = 0:2:Rx_o+200; Error = zeros(1,length(Rx));
for i = 1:length(Rx)
    Error(i) = g_dot_old - Flow*(((abs(tau_sat-Rx(i))-K0)/Da)^n)*...
        exp(B0_o*((abs(tau_sat-Rx(i))-K0)/Da)^(n+1));
end
% Find correct solution location
found = 0;
for i = 1:length(Error)-1
    if Error(i)>0 && Error(i+1)<0
        found = found +1;
        Cross(found) = i;
    elseif Error(i)<=0 && Error(i+1)>=0
        found = found +1;
        Cross(found) = i;
    end
end
guess = [Rx(Cross(1)-2), Rx(Cross(1)), Rx(Cross(1)+2)];
Rx_new = find_Rx_given_Edot(g_dot_old,guess,K0,tau_sat,n,B0,Da,Flow);
```

Figure D.4: Script for finding new values of $R_\chi$ if other parameters change: Note that it requires the function *find_Rx_given_Edot()*

## Code 5

```
function Rx_new = find_Rx_given_Edot(g_dot,Rx,k,t_sat,n,B0,Da,C)

Tolerance = 1e-25;

Rx_try(2) = C*(((abs(t_sat-Rx(2))-k)/Da)^n)*...
    exp(B0*((abs(t_sat-Rx(2))-k)/Da)^(n+1))*sign(g_dot);
Error(2) = g_dot - Rx_try(2);
if abs(Error(2))<Tolerance %done!!
    Rx_new = Rx(2);
else
    Rx_try(1) = C*(((abs(t_sat-Rx(1))-k)/Da)^n)*...
        exp(B0*((abs(t_sat-Rx(1))-k)/Da)^(n+1))*sign(g_dot);
    Rx_try(3) = C*(((abs(t_sat-Rx(3))-k)/Da)^n)*...
        exp(B0*((abs(t_sat-Rx(3))-k)/Da)^(n+1))*sign(g_dot);
    Error = [(g_dot-Rx_try(1)),Error(2), (g_dot-Rx_try(3))];

    E1 = Error(1)*Error(2);
    E2 = Error(2)*Error(3);
    if E1<0 % the initial guess was too high
        Rx = [Rx(1), (Rx(1)+Rx(2))/2, Rx(2)];
    elseif E2<0 % the initial guess was too low
        Rx = [Rx(2), (Rx(2)+Rx(3))/2, Rx(3)];
    else % High bound was too low - increase bound slowly
        Rx = [Rx(3) Rx(3)+9 Rx(3)+10];
    end
    Rx_new = find_Rx_given_Edot(g_dot,Rx,k,t_sat,n,B0,Da,C); % Recursion
end
```

Figure D.5: Function *find_Rx_given_Edot()*: for use with script in Figure D.4

# References

Alers, G. A., Neighbours, J. R., Sato, H. (1960). " Temperature Dependent Magnetic Contributions to the High Field Elastic Constants of Ni and Fe-Ni Alloys." Journal of Physics Chemistry and Solids **13**: 40-55.

Almroth, P., Hasselqvist, M., Simonsson, K., Sjostrom, S. (2004). "Viscoplastic-plastic modeling of IN792." Computational Materials Science **29**: 437-445.

Almroth, P., Hasselqvist, M., Sjostrom, S., Simonsson, K. (2002). "Modeling of the high temperature behaviour of IN792 in gas turbine hot parts." Computational Materials Science **25**: 305-315.

Arsenlis, A., Parks, D. M. (1999). "Crystallographic aspects of geometrically necessary and statictically-stored dislocation density." Acta Mater **47**(5): 1597-1611.

Arsenlis, A., Parks, D. M. (2002). "Modeling the evolution of crystallographic dislocation density in crystal plasticity." Journal of Mechanics, Physics and Solids **50**(9): 1979-2009.

Arsenlis, A., Parks, D. M., Becker, R., Bulatov, V. V. (2004). "On the evolution of crystallographic dislocation density in non-homogeneously deforming crystals." Journal of Mechanics, Physics and Solids **52**(6): 1213-1246.

Asaro, R. J. (1983). "Crystal Plasticity." Journal of Applied Mechanics **50**: 921-934.

ASTM (2008). Standard Test Methods for Tension Testing of Metallic Materials. ASTM, American Associan State. **E 8/E 8M - 08:** 25.

Balasubramanian, S., Anand, L. (2002). "Elasto-viscoplastic constitutive equations for polycrystalline fcc materials at low homologous temperatures." Journal of the Mechanics and Physics of Solids **50**: 101-126.

Becker, R., Butler, J. F., Hu, H., Lalli, L. A. (1991). "Analysis of an aluminum single crystal with unstable initial orientation (001)[111] in channel die compression." Metallurgical transactions A **22**: 45-58.

Bettge, D., Osterle, W. (1999). "Cube slip in near-[111] oriented speciments of a single-crystal nickel-base superalloy." Scripta Materialia **40**(4): 389-395.

Bhattachar, V. S., Stouffer, D. C. (1993). "Constitutive equations forthe thermomechanical response of rene 80: Part I - developement from isothermal data." Journal of Engineering Materials and Technology **115**: 351-357.

Carroll, D. L. (1996). "Chemcial Laser Modeling with Genetic Algorithms." AIAA J. **34**(2): 338-346.

Chaboche, J. L. (1989). "Constitutive Equations For Cyclic Plasticity And Cyclic Viscoplasticity " Intternational Journal of Plasticity **5**: 247-302.

Chaboche, J. L., Rousselier, G. (1983). "On the plastic and viscoplastic constitutive equations-part I: Rules developed with internal variable concept." International Journal of Pressure Vessle Technology **105**: 153-158.

Chan, K. S., Bodner, S. R., Walker, K. P., Lindholm, U. S. (1985). A survey of Unified Constitutive Theories.

Christ, H.-J., Bauer, V. (2011). "Effect of Creep and Oxidation on the Isothermal and Thermomechanical Fatigue Behavior of an Austenitic Stainless Steel."

Courant, R. (1943). "Variational methods for the solution of problems of equilibrium and vibrations." Bull Am Math Soc **49**: 1-23.

DeMarco, J. P., Hogan, E. A., Stewart, C. M., Gordon, A. P. (2010). "An Efficient Method for the Optimizaiton of Viscoplastic Constitutive Model Constants." Proceedings of Proceedings of ASME Turbo Expo 2010: Power for Land, Sea and Air: 1-14.

Esmaeili, S., Engler-Pinto, C. C. J., Rezai-Aria, F. (1995). "Interaction Between Oxidation and Thermomechanical Fatigue in IN738LC Superalloy - I." Scripta Metallurgica it Materialia **32**(11): 1777-1781.

Evers, L. P., Brekelmans, W. A. M., Geers, M. G. D. (2004). "Non-local crystal plasticity model with intrinsic SSD and GND effects." Journal of Mechanics, Physics and Solids **52**(10): 2379-2401.

Evers, L. P., Parks, D. M., Brekelmans, W. A. M., Geers, M. G. D. (2002). "Crystal Plasticity Model with Enhanced hardening by geometrically necessary dislocation accumulation." Journal of Mechanics, Physics and Solids **50**(11): 2403-2424.

Fahrmann, M., Hermann, W., Fahrmann, E., Boegli, A., et al. (1999). "Determination of matrix and precipitate elastic constants." Materials Science and Engineering A **260**: 212-221.

Frost, H. J., Ashby, M. F. (1982). Deformation-Mechanism Maps - The Plasticity and Creep of Metals and Ceramics. Oxford, UK, Pergamon Press.

Goldberg, D. E. (1989). Genetic Algorithms in Search, Optimization and Machine Learning. Reading, MA, Addison-Wesley.

Gordon, A. P. (2006). Crack Initiation Modeling of a Directionally-Solidified Nickel-Base Superalloy. George W. Woodruff School of Mechanical Engineering Atlanta, Georgia Institute of Technology. **Doctor of Philosophy:** 481.

Huber, N., Tsakmakis, C. (2001). "A Neural Network Tool for Identifying the Material Parameters of a Finite Deformation Vciscoplasticity Model with Static Recovery." Computational Methods in Applied Mechanics and Engineering **191**: 353-384.

Ichitsubo, T., Ogi, H., Hirao, M., Tanaka, K., et al. (2002). "Elastic constant measurement of Ni-base superalloy with the RUS and EMAR methodsmethods." Ultrasonics **40**: 211-215.

Kocks, U. F. (1970). "The Relation Between Polycrystal Deformation and Single-Crystal Deformation." MetallURGICAL AND MATERIALS TRANSACTIONS B **1**(5): 1121-1143.

Kuhn, H.-A., Sockel, H.-G. (1989). " Elastic Properties of Textured and Directionally Solidified Nickel-based Superalloys Between 25 and 1200C." Materials Science and Engineering A **A112**: 117-126.

Kupkovits, R. A. (2009). Thermomechanical Fatigue Behavior of the Directionally-Solidified Nickel-Base Superalloy CM247LC. George W. Woodruff School of Mechanical Engineering. Atlanta, Georgia Institute of Technology **Master of Science:** 280.

Kupkovits, R. A., Smith, D. J., Neu, R. W. (2010). "Influence of minimum temperature on the thermomechanical fatigue of a directionally-solidified Ni-base superalloy." Procedia Engineering **2**(1): 687-696.

Ledbetter, H. M., Reed, R. P. (1973). "Elastic Properties of Metals and Alloys, I. Iron, Nickel, and Iron-Nickel Alloys." Journal of Physics Chemistry and Solids **2**(3): 531-617.

Ma, A., Roters, F., Raabe, D. (2006a). "A dislocation density based constitutive model for crystal plasticity FEM including geometrically necessary dislocations." Acta Mater **54**(2169-79).

Ma, A., Roters, F., Raabe, D. (2006b). "On the consideration of interactions between dislocations and grain boundaries in crystal plasticity finite element modeling - theory, experiments, and simulations." Acta Mater **54**: 2181-2194.

Ma, X., Gu, J., Shi, H. (2008). Investigation of Low Cycle Fatigue (LCF) Behavior for Anisotropic Materials, Tsinghua University

McDowell, D. L. (1992). "A nonlinear Kinematic Hardening Theory for Cyclic Thermoplasticity and Thermoviscoplasticity." International Journal of Plasticity **8**: 695-728.

McGinty, R. D. (2001). Multiscale Representation of Polycrystalline Inelasticity. George W. Woodruff School of Mechanical Engineering. Atlanta, GA, Georgia Institute of Technology. **Doctor of Philosophy in Mechanical Engineering**.

McGinty, R. D., McDowell, D. L. (1999). "Multiscale Polycrystal Plasticity." Journal of Engineering Materials and Technology **121**(2): 203-209.

Miller, A. (1976). "An Inelastic Constitutive Model for Monotonic Cyclic and Creep Deformation." Journal of Engineering Materials and Technology **98**(2): 97-105, 106-113.

Moosbrugger, J. C., Mcdowell, D. L. (1990). "A Rate-dependent Bounding Surface Model with a Generalized Image Point for Cyclic Nonproportional Viscoplasticity." Journal of the Mechanics and Physics of Solids **38**(5): 627-656.

Mucke, R., Bernhardi, O.-E. (2003). "A constitutive model for anisotropic materials based on Neuber's rule." Computer Methods in Applied Mechanics and Engineering **192**: 4237-4255.

Nathal, M. V., Ebert, L. J. (1985). "Elevated Temperature Creep-Rupture Behavior of the Single Crystal Nickel-Base Superalloy NASAIR 100." Metallurgical Transactions **16A**: 427-439.

Nouailhas, D. (1989). "Unified Modelling of Cyclic Viscoplasticity: Application to Austenitic Stainless Steels " International Journal of Plasticity **5**: 501-520.

Okazaki, M., Sakaguchi, M. (2008). "Thermo-mechanical fatigue failure of a single crystal Ni-based superalloy." International Journal of Fatigue **30**(2): 318-323.

Peirce, D., Asaro, R. J., Needleman, A. (1982). "An analysis of nonuniform and localized deformaion in ductile single crystals." Acta Metall **30**: 1087-1119.

Qin, Q., Bassani, J. L. (1992a). "Non-associated Plastic Flow in Single Crystals." Journal of the Mechanics and Physics of Solids **40**(4): 835-862.

Qin, Q., Bassani, J. L. (1992b). "Non-Schmid Yield Behavior In Single Crystals." Journal of the Mechanics and Physics of Solids **40**(4): 813-833.

Ramaswamy, V. G., Stouffer, D. C., Laflen, J. H. (1990). "A unified constitutive model for the uniaxial response of rene 80 at temperatures between 583 and 982 C." Journal of Engineering Materials and Technology **112**: 280-286.

Reed, R. C. (2006). The Superalloys: Fundamentals and Applications, Cambridge University Press, Cambridge.

Roters, F., Eisenlohr, P., Hantcherli, L., Tjahjanto, D. D., et al. (2010). "Overview of constitutive laws, kinematics, homogenization and multiscale methods in crystal plasticity finite-element modeling: Theory, experiments, applications." Acta Materialia **58**(4): 1152-1211.

Rowley, M. A., Thornton, E. A. (1996). "Constitutive modeling of the visco-plastic response of hastelloy-X and aluminum alloy 8009." Journal of Engineering Materials and Technology **118**: 19-27.

Schmid, E., Boas, W. (1950). Plasticity of crystals with a special reference to metals. London, F. A. Hughes.

Sheh, M. Y., Stouffer, D. C. (1990). "A Crystallographic Model for the Tensile and Fatigue Response for Rene N4 at 982°C." Journal of Applied Mechanics **57**: 25-31.

Shenoy, M. (2005). "Modeling effects of nonmetallic inclusions on LCF in DS nickel-base superalloys." International Journal of Fatigue **27**(2): 113-127.

Shenoy, M., Kang, M. S., Neu, R. W., McDowell, D. L. (2002). Cyclic deformation of a DS Ni-base superalloy at 871C. Proceedings CAMP2002: High-Temperature Fatigue. G. Biallas, H. J. Maier, O. Hahn, K. Herrmann and F. Vollertsen. Germany: Bad Lippspringe. **3:** 14-28.

Shenoy, M., McDowell, D., Neu, R. (2006). "Transversely isotropic viscoplasticity model for a directionally solidified Ni-base superalloy." International Journal of Plasticity **22**(12): 2301-2326.

Shenoy, M., Tjiptowidjojo, Y., McDowell, D. (2008). "Microstructure-sensitive modeling of polycrystalline IN 100." International Journal of Plasticity **24**(10): 1694-1730.

Shenoy, M. M. (2006). Constitutive Modeling and Life Prediction in Ni-Base Superalloys. George W. Woodruff School of Mechanical Engineering Atlanta, Georgia Institute of Technology **Doctor of Philosophy** 318.

Shenoy, M. M., Gordon, A. P., McDowell, D. L., Neu, R. W. (2005). "Thermomechanical Fatigue Behavior of a Directionally Solidified Ni-Base Superalloy." Journal of Engineering Materials and Technology **127**(3): 325 - 336.

Siemens (2010). Personal communication. Atlanta.

Song, J. (2010). Hierarchical Multiscale Modeling of Ni-base superalloys. George W. Woodruff School of Mechanical Engineering. Atlanta, Georgia Institute of Technology. **Master of Science:** 122.

Srikanth, A., Zabaras, N. (1999). "A Computational Model For the Finite Element Analysis of Thermoplasticity Coupled with Ductile Damage at Finite Strains." International Journal for Numerical Methods in Engineering **45**: 1569-1605.

Stouffer, D. C., Ramaswamy, V. G., Laflen, J. H., Van Stone, R. H., et al. (1990). "A constitutive model for the inelastic multiaxial response of rene 80 at 871 and 982 C." Journal of Engineering Materials and Technology **112**: 241-246.

Sumpter, B. G., Noid, D. W. (1996). "On the Design, Analysis, and Characterization of Materials using Computational Neural Networks." Annual Review of Materials Science **26**: 223-277.

Taylor, G. I. (1938). "Plastic strain in metals." J. Inst. Metals **62**: 307.

Tong, J. (2004). "Modelling of cyclic plasticity and viscoplasticity of a nickel-based alloy using Chaboche constitutive equations." International Journal of Fatigue **26**(8): 829-837.

Venkataramani, G., Deka, D., Ghosh, S. (2006). "Crystal Plasticity Based Fe Model for Understanding Microstructural Effects on Creep and Dwell Fatigue in Ti-6242." Journal of Engineering Materials and Technology **128**(3): 356.

Walker, K. P., Jordan, E. H. (1985). "Constitutive Modeling of Superalloy Single Crystals and Directionally Solidified Materials."

Wang, A.-J., Kumar, R. S., Shenoy, M. M., McDowell, D. L. (2006). "Microstructure-Based Multiscale Constitutive Modeling of $\gamma - \gamma'$ Nickel-Base Superalloys." International Journal for Multiscale Computational Engineering **4**: 663 - 692.

Xie, C. L., Ghosh, S., Groeber, M. (2004). "Modeling Cyclic Deformation of HSLA Steels Using Crystal Plasticity." Journal of Engineering Materials and Technology **126**(4): 339.

Yagawa, G., Okuda, H. (1996). "Neural Networks in Computational Mechanics." Archives of Computational Methods in Engineering **3**(4): 435-512.

Yaguchi, M., Yamamoto, M., Ogata, T. (2002a). "A viscoplastic Constitutive Model for Nickel-base Superalloys, Part 1: Kinematic Hardening Rule of Anisotropic Dynamic Recovery." International Journal of Plasticity **18**: 1083-1109.

Yaguchi, M., Yamamoto, M., Ogata, T. (2002b). "A viscoplastic Constitutive Model for Nickel-base Superalloys, Part 2: Modeling Under Anisothermal Conditions." International Journal of Plasticity **18**: 1111-1131.

Yue, Z. F., Lu, Z. Z., Zheng, C. Q. (1997). "Fracture behavior of a nickel-base single crystal superalloy as predicted by the strain energy density criterion." Theoretical and Applied Fracture Mechanics **26**: 89-104.